

MEMOIRS
OF THE
FACULTY OF ENGINEERING
OSAKA CITY UNIVERSITY

VOL. 56

DECEMBER 2015

PUBLISHED BY THE
GRADUATE SCHOOL OF ENGINEERING
OSAKA CITY UNIVERSITY

This Memoirs is annually issued. Selected original works of the members of the Faculty of Engineering are compiled herein. Abstracts of paper presented elsewhere during the current year are also compiled in the latter part of the volume.

All communications with respect to Memoirs should be addressed to:

Dean of the Graduate School of Engineering
Osaka City University
3-3-138, Sugimoto, Sumiyoshi-ku
Osaka 558-8585, Japan

Editors

Yusuke YAMADA

Takeshi TAKIYAMA

Tomohito TAKUBO

Masafumi MURAJI

Noritsugu KOMETANI

Tetsu TOKUONO

Koichi KANA

MEMOIRS OF THE FACULTY OF ENGINEERING
OSAKA CITY UNIVERSITY

VOL. 56

DECEMBER 2015

CONTENTS

Regular Articles 1

Urban Engineering

Urban Design and Engineering

Vertical Impulsive Forces to a Structure on Multi-layered Grounds at Near Field Earthquake

Keiichiro SONODA and Hiroaki KITOH 1

Applicability of Strain Softening Analysis for Tunnel Excavation

Kenichi NAKAOKA and Hiroaki KITOH 15

Study on Evaluation of Fine Fraction Content of Soil Using Soil-Metal Friction Sound for Liquefaction Assessment by Swedish Ram Sounding

Suguru YAMADA and Akihiko OSHIMA 29

Analysis of Resident Interest and Intentions for Community Bus Network Reorganization

Yumie SAWADA and Takashi UCHIDA 37

Major Issues of Bicycle Use in Urban Area from View Point of Community Development

Yurie ISHINUMA, Yasuo HINO and Yuuka WATANABE 51

Abstracts of Papers Published in Other Journals	57
<i>Mechanical and Physical Engineering</i>	
<i>Mechanical Engineering</i>	59
<i>Physical Electronics and Informatics</i>	
<i>Applied Physics and Electronics</i>	67
<i>Electric and Information Engineering</i>	77
<i>Applied Chemistry and Bioengineering</i>	
<i>Applied Chemistry and Bioengineering</i>	81
<i>Urban Engineering</i>	
<i>Architecture and Building Engineering</i>	100
<i>Urban Design and Engineering</i>	102

MEMOIRS
OF THE
FACULTY OF ENGINEERING
OSAKA CITY UNIVERSITY

VOL. 56

DECEMBER 2015

PUBLISHED BY THE
GRADUATE SCHOOL OF ENGINEERING
OSAKA CITY UNIVERSITY

Vertical Impulsive Forces to a Structure on Multi-layered Grounds at Near Field Earthquake

Keiichiro SONODA* and Hiroaki KITOH**

(Received October 2, 2015)

Synopsis

At Hyogo-ken Nanbu Earthquake 1995, a lot of instances of structural failure or damage due to vertical impulsive ground motion were observed. Objective of the paper is to investigate vertical impulsive force mechanism inducing failure of reinforced concrete bridge piers supported by multi-layered grounds.

KEYWORDS: seismic force, multi-layered grounds, impulsive force, reinforced concrete viaduct pier

1. Preliminary

Figure 1.1 shows typical failure modes of reinforced concrete (RC) viaduct pier observed in a highway within Kobe port area at Hyogo-ken Nanbu Earthquake 1995. The failure zone is located on only the upper portion of column and is developed on the whole cross sectional area in spite of their rectangular cross section. It will be a natural view that such failure modes were caused by strong vertical ground motion rather than strong horizontal ground motion.



Fig.1.1 Viaduct pier failure modes observed in Harbor Highway in Kobe City (Photo by author)

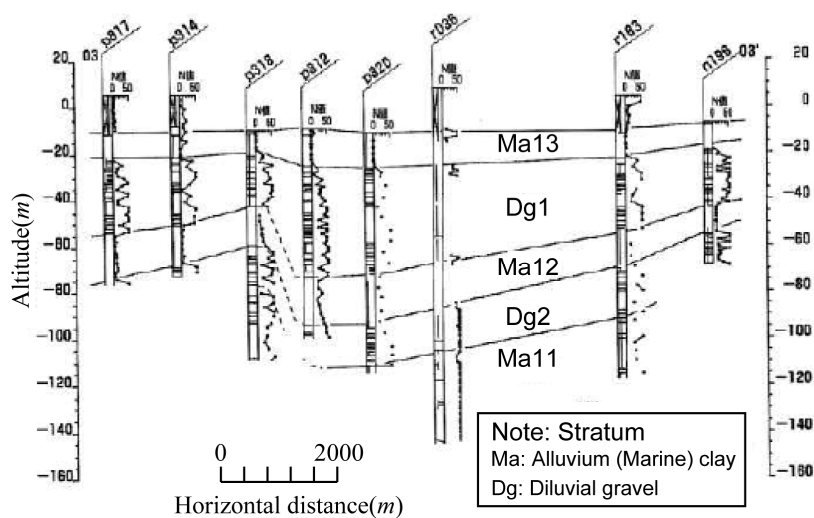


Fig.1.2 Geological map in the vicinity of Harbor Highway¹⁾

* Professor Emeritus
 ** Professor, Urban Engineering

Figure 1.2 shows a geological map in the vicinity of Harbor Highway in Kobe City, which was presented by the 3rd Port Construction Bureau of the Ministry of Transportation in Japan, in 1998¹⁾. The surface zone of ground is covered by soft clay of alluvium stratum, and below that diluvium stratum is developed. The deep zone than several ten meters below is occupied by stiff sand or grain stratum.

This paper is focused on characteristics of vertical stress wave propagation from the deep base ground to the multi-layered surface grounds, and is devoted to find the impulsive force mechanism against reinforced concrete viaduct pier on multi-layered grounds due to a near field earthquake such as Hyogo-ken Naibu earthquake.

2. Plane elastic stress wave characteristics through multi-layered grounds

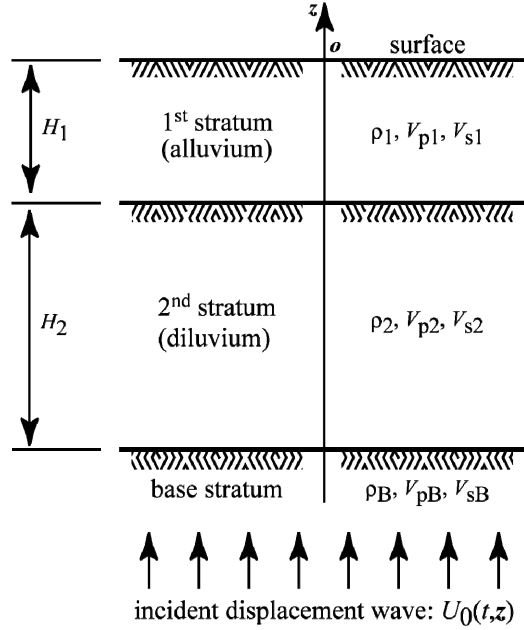


Fig.2.1 Multiple reflection of vertical displacement wave through multi-layered grounds²⁾

Kanai, K.(1957)²⁾ has found theoretical solutions of one dimensional wave equation for multi-layered elastic grounds shown in Fig.2.1. In those solutions, the vertical incident wave to semi-infinite base stratum is assumed as a harmonic wave,

$$U_0(t, z) = u_0 \cos(pt - f_3 z) \quad (2.1)$$

where $p = 2\pi/T_0$, T_0 : period, $f_3 = 2\pi/L_3$, L_3 : incident wave length within the base stratum.

From the free condition at the surface ($z = 0$), the continuous conditions at the interface between 1st and 2nd strata and the interface between 2nd and the semi-infinite base strata, the vertical displacement waves developed within 1st and 2nd strata, respectively are given as follows²⁾ :

$$U_1(t, z) = u_1(z) \cdot \cos(pt - \tan^{-1} \frac{Q}{P}), \quad u_1(z) = \frac{2u_0}{\phi} \cos q_1 \frac{z}{H_1} \quad (2.2)$$

$$U_2(t, z) = u_2(z) \cdot \cos(pt - \tan^{-1} \frac{Q}{P}),$$

$$u_2(z) = \frac{2u_0}{\phi} \left\{ \cos q_1 \cos q_2 \left(\frac{H_1}{H_2} + \frac{z}{H_2} \right) - \alpha_1 \cdot \sin q_1 \cdot \sin q_2 \left(\frac{H_1}{H_2} + \frac{z}{H_2} \right) \right\} \quad (2.3)$$

in which,

$$\phi = \sqrt{P^2 + Q^2}, \quad P = \cos q_1 \cos q_2 - \alpha_1 \sin q_1 \sin q_2, \quad Q = \alpha_2 (\cos q_1 \sin q_2 + \alpha_1 \sin q_1 \cos q_2),$$

H_m ($m=1,2$) is the thickness of each stratum, $q_m = \rho H_m / V_{pm}$ ($m=1,2$), V_{pm} is wave velocity ($m=1,2$), $f_m = 2\pi / L_m$, L_m : wave length ($m=1,2$), ρ_m : ground density ($m=1,2$), $\alpha_m = \rho_m V_{pm} / (\rho_{m+1} V_{pm+1})$, ($m=1,2$). If the above solutions are applied to longitudinal displacement wave, those equations can be transformed into vertical stress wave solutions, exchanging Eq.(2.1) with the incident velocity wave or incident stress wave as

$$V_0(t, z) = v_0 \sin(pt - f_3 z), S_0(t, z) = \sigma_0 \sin(pt - f_3 z) \quad (2.4)$$

where, $v_0 = -pu_0$, $\sigma_0 = -\rho_3 V_{p3} \cdot v_0$, V_{p3} means longitudinal wave velocity of the base stratum.

Then the velocity and stress waves developed within 1st and 2nd strata are given as

$$V_m(t, z) = \frac{\partial U_m(t, z)}{\partial t} = -pu_m(z) \cdot \sin(pt - \tan^{-1} \frac{Q}{P}), \quad m=1,2 \quad (2.5)$$

$$S_m(t, z) = E_m \frac{\partial U_m(t, z)}{\partial z} = E_m \frac{\partial u_m(z)}{\partial z} \cdot \cos(pt - \tan^{-1} \frac{Q}{P}), \quad m=1,2 \quad (2.6)$$

in which, $E_m = \rho_m V_{pm}^2$, $m=1,2$ means longitudinal elastic modulus of each stratum.

In the following discussions, three types of ground property shown in Table 2.1 are considered, in which the semi-infinite base stratum is fixed as $\rho_3 = 2.0t/m^3$ in density and $V_{p1} = 3000m/s$ in longitudinal wave velocity.

Table 2.1 Ground properties considered

	first stratum thickness: $H_1 = 10m$		second stratum thickness: $H_2 = 10, 20, 30, 50, 100m$	
	$\rho_1(t/m^3)$	$V_{p1}(m/s)$	$\rho_2(t/m^3)$	$V_{p2}(m/s)$
ground A	1.5	300	1.6	600
ground B	1.5	300	2.0	1000
ground C	1.6	600	2.0	1000

note: ρ_m and V_{pm} , $m=1,2$ mean density and longitudinal wave velocity, respectively

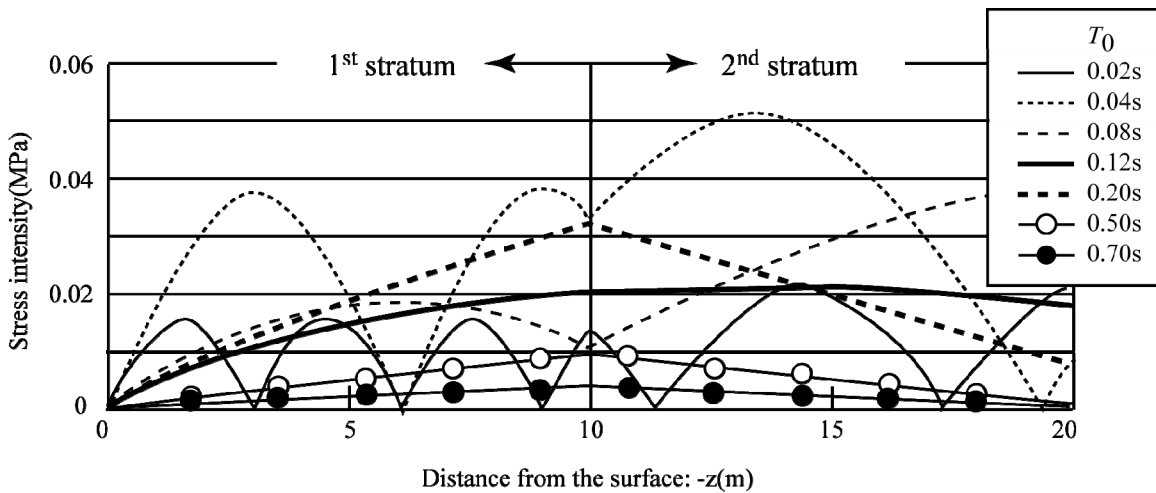


Fig.2.2 Vertical stress distributions within 1st and 2nd strata (ground A, $H_1=H_2=10m$, $v_0 = 1cm/s$)

The first numerical example was taken for the ground A with $H_1 = 10m$ and $H_2 = 10m$, in which the incident

velocity of $v_0 = 1\text{cm/s}$ ($\sigma_0 = -0.06\text{ MPa}$ in incident stress) and the periods of $0.02 \leq T_0 \leq 0.7\text{ sec}$ were applied. Figure 2.2 shows the vertical stress amplitude developed within 1st and 2nd strata. As seen in this figure, the vertical stress intensities are much influenced by the periods, T_0 , of incident velocity wave in the basic stratum, and the maximum stress intensity within 1st and 2nd strata attains to 0.038 MPa and 0.051 MPa , respectively at $T_0 = 0.04\text{ sec}$, but in the lower frequency area such as $T_0 > 0.2\text{ sec}$, the stress intensities much decreases.

Next, focusing on the interface of 1st and 2nd strata which may be ordinarily situated at the supporting face of a superstructure's foundation, the relations between the maximum intensities of vertical stress (denoted by $\sigma_{12,\text{max}}$) at the interface and the periods of incident velocity wave, T_0 , were investigated for the grounds A, B and C indicated in Table 2.1. Figure 2.3 shows the results for the ground A, in which $\sigma_{12,\text{max}}$ attains to 0.08 MPa at $T_0 = 0.12\text{ sec}$ in the case of $H_1 = 10\text{ m}$ and $H_2 = 30\text{ m}$.

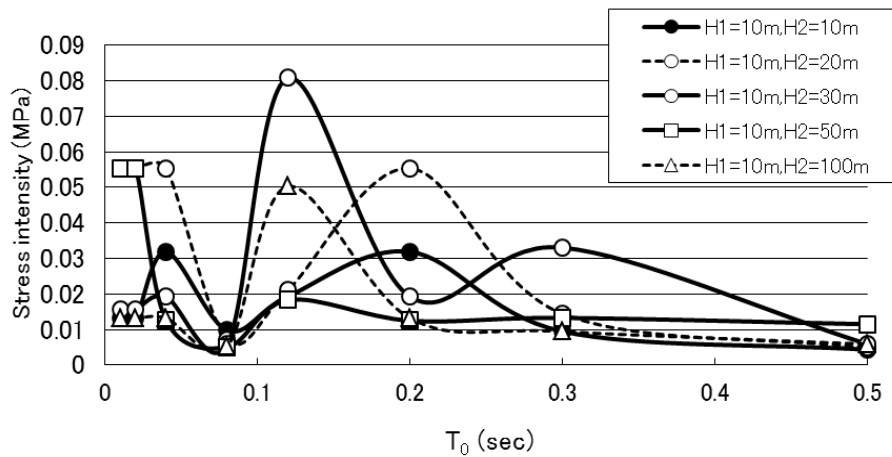


Fig.2.3 Maximum stress intensities at the interface of 1st and 2nd strata (ground A, $v_0 = 1\text{cm/s}$)

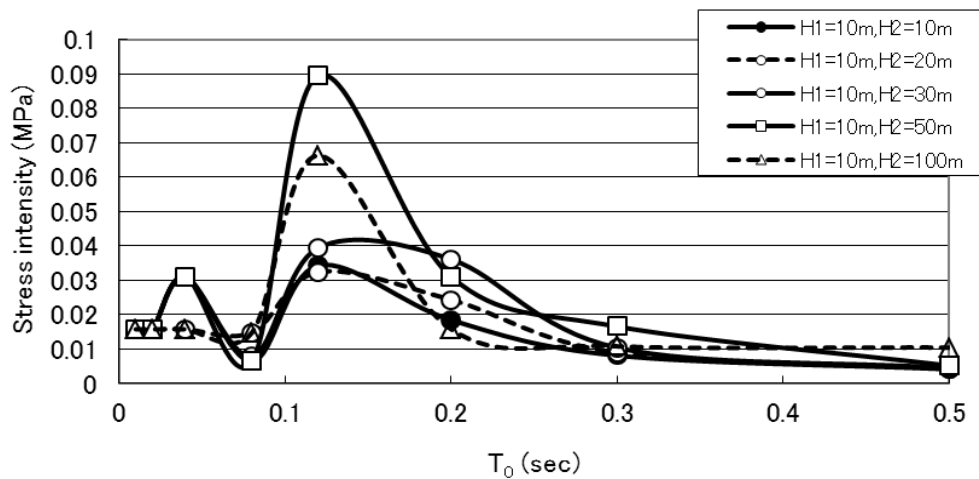


Fig.2.4 Maximum stress intensities at the interface of 1st and 2nd strata (ground B, $v_0 = 1\text{cm/s}$)

Figures 2.4 and 2.5 show the results for the grounds B and C, respectively. In the ground B, the peak values of $\sigma_{12,\text{max}}$ appear at $T_0 = 0.12\text{ sec}$, and the maximum stress intensity attains to 0.09 MPa which is corresponding to 1.5 times as large as $\sigma_0 = \rho_3 V_{p3} v_0 = 0.06\text{ MPa}$ in the incident stress within the base stratum. On the other hand, in the ground C, a large intensity of $\sigma_{12,\text{max}}$ appears at $T_0 = 0.08\text{ sec}$. Summarizing all the results of Figs.2.3, 2.4 and 2.5, we can mention that the predominant large intensities of $\sigma_{12,\text{max}}$ which is almost

same or more than the incident stress intensity, $\sigma_0 = 0.06 \text{ MPa}$, appear only in the relatively higher frequency zone such as $T_0 < 0.2 \text{ sec}$.

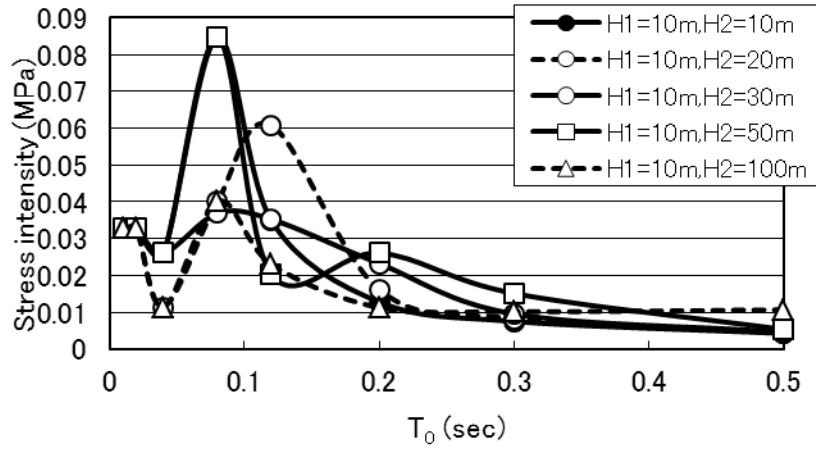


Fig.2.5 Maximum stress intensities at the interface of 1st and 2nd strata (ground C, $v_0 = 1 \text{ cm/s}$)

3. Applicability of numerical simulation procedure

In order to investigate stress wave interaction problems between a superstructure and multi-layered grounds, it is difficult to find theoretical solutions like Eqs. (2.5) and (2.6). Therefore, we have to rely on a numerical simulation method such as finite element method (called FEM).

As a preliminary study, applicability of one dimensional lumped mass-spring model shown in Fig. 3.1(a) was examined in comparison with the theoretical solutions obtained previously. In this model, 1st stratum with H_1 in thickness is divided by m_1 elements, 2nd stratum with H_2 in thickness by m_2 elements, and the base stratum with H_B in thickness by m_B elements. The elastic spring constant of each element is taken as $k_i = E_{Gi} / D_{zi}$, where E_{Gi} is longitudinal elastic modulus and D_{zi} is distance between adjacent nodes.

Incident displacement and velocity waves in the base stratum are taken as the same to Eqs.(2.1) and (2.4) namely

$$U_0(t, z) = u_0 \cos(pt - f_B z) \quad (2.1)$$

$$V_0(t, z) = -p u_0 \sin(pt - f_B z) \quad (2.4)$$

where,

$$p = 2\pi / T_0, \quad f_B = 2\pi / L_B, \quad L_B = V_{pB} T_0, \quad V_{pB} \text{ is longitudinal}$$

wave velocity of the base stratum.

Initial conditions are given as

$$U_0(0,0) = 0, \quad V_0(0,0) = \left. \frac{\partial U_0}{\partial t} \right|_{z=0, t=0} = 0 \quad (3.1)$$

The bottom face of base stratum ($z = 0$) is forced as

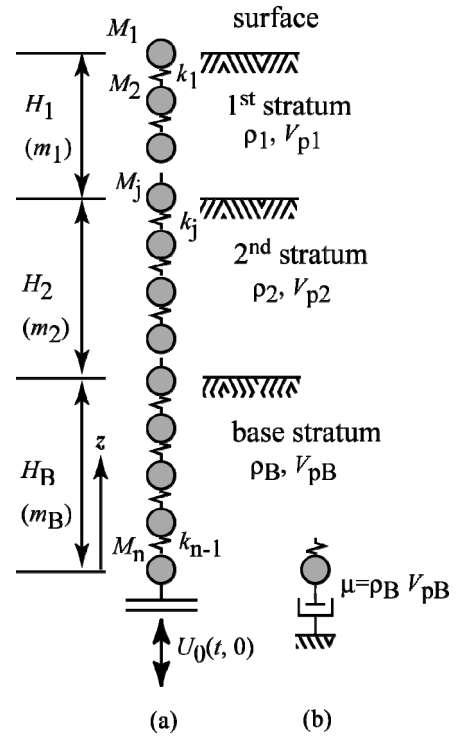


Fig.3.1 Lumped mass-spring model

$$U_0(t,0) = u_0(1 - \cos pt) \quad (3.2)$$

$$V_0(t,0) = v_0 \sin pt \quad (3.3)$$

where, $v_0 = pu_0 = (2\pi/T_0) \cdot u_0$. In this model, how to determine the thickness of basic stratum, H_B , is important, because the theoretical solutions presented in the previous section are derived for a semi-infinite base stratum.

Two methods are considered in the followings.

Method 1

The thickness of base stratum, H_B , takes so large as to exclude the influence of wave reaction at the bottom face of base stratum ($z=0$). If the relevant observation time is taken as $0 < t < T_{obs}$, $H_B \geq 3T_{obs}V_{pB}$ is sufficient condition to exclude a wave reflection influence from the bottom face of base stratum to 1st and 2nd strata.

Figure 3.2 shows comparison between the numerical results by a lumped mass-spring model and the theoretical ones on the maximum stress intensities (denoted by $\sigma_{12,max}$) at the interface of 1st and 2nd strata in the ground A with $H_1 = 10m$, $m_1 = 20$, $H_2 = 20m$, $m_2 = 20$ and $H_B = 1500m$, $m_B = 100$, which is taken as $T_{obs} = 1.5\text{sec}$. Good correlation between the numerical results and the theoretical ones is found except for very high frequency zone of $T_0 < 0.02\text{sec}$. It can be said, therefore, that a lumped mass spring model yields a reliable solution of one dimensional stress propagation problem, if a large thickness of base stratum, H_B , is applied such as $H_B \geq 3T_{obs}V_{pB}$.

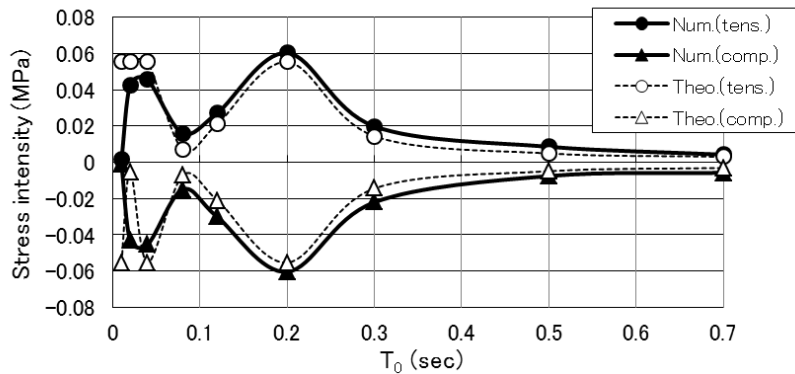


Fig.3.2 Comparison of the numerical results with the theoretical ones on $\sigma_{12,max}$ (ground A, $H_B=1500m$, $v_0 = 1cm/s$)

Method 2

Here, the case of limited thickness of base stratum such as $H_B < 3T_{obs}V_{pB}$ is considered. In this case, the

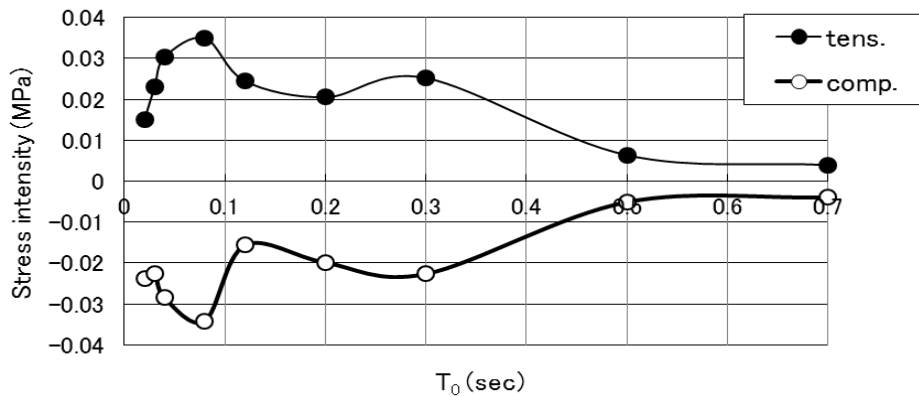


Fig.3.3 Numerical results on $\sigma_{12,max}$ by **Method 2** (ground A, $H_B = 40m$, $v_0 = 1cm/s$)

constraint conditions of Eqs.(3.2) and (3.3) are applied for only their first one period part, namely

$$U_0(t,0) = u_0(1 - \cos pt), \quad 0 \leq t \leq T_0 \quad (3.4)$$

$$V_0(t,0) = v_0 \sin pt, \quad 0 \leq t \leq T_0 \quad (3.5)$$

Furthermore, for the time domain, $t > T_0$, the bottom face of base stratum ($z = 0$) is treated as a viscous boundary shown in Fig.3.1(b) to exclude the wave reflection influence as possible.

Figure 3.3 shows the numerical results on $\sigma_{12,\max}$ which are obtained for the ground A of $H_1 = 10m$, $m_1 = 20$, $H_2 = 20m$, $m_2 = 20$ and $H_B = 40m$, $m_B = 20$. Comparing Fig.3.3 with 3.2, the incident constraints with only the first one period of Eqs.(3.4) and (3.5) yield lower stress intensities at the interface of 1st and 2nd strata in comparison with the continuous harmonic constraint by Eqs.(3.2) and (3.3). But the frequency zone yielding the peak stress intensities is similar from each other. Therefore, **Method 2** may be useful as an approximate method for more complicated two or three dimensional stress wave problems which will be later discussed.

4. Mechanism of vertical impulsive forces against a structure on multi-layered grounds

Characteristics of vertical forces to an overloaded structure on the multi-layered grounds shown in Fig.2.1 are discussed through three dimensional axisymmetric FEM analyses. Here, a structure is assumed as a simple rigid body, assuming that a reinforced concrete structure is much stiffer in comparison with the supporting ground materials.

Figure 4.1 shows the finite element division used. A three layered ground model similar to Fig.3.1 for numerical analyses is applied, in which the vertical element division is m_1 for the 1st stratum of H_1 in thickness, m_2 for the 2nd stratum of H_2 in thickness, and m_B for the base stratum of H_B in thickness, while the horizontal element division is n_1 for the structural basement of B_1 in radius, and $n_2 + n_3$ for the remaining ground region of $B_2 + B_3$, in radius, respectively. Joint elements with no tensile resistance are inserted between the structural basement and the ground surface.

The incident vertical displacement and velocity waves are given by the constraints of Eqs. (3.4) and (3.5) at the bottom face of base stratum in **Method 2**. Namely,

$$U_z(t,0) = u_0(1 - \cos pt), \quad 0 \leq t \leq T_0 \quad (4.1)$$

$$V_z(t,0) = v_0 \sin pt, \quad 0 \leq t \leq T_0 \quad (4.2)$$

$$U_x(t,0) = 0, \quad V_x(t,0) = 0 \quad (4.3)$$

While for $t > T_0$ the bottom face of base stratum is treated as a viscosity boundary, and in addition the horizontal edges of ground are also treated as a viscosity boundary to exclude the horizontal wave reflection effects as possible. The viscosity coefficients are applied as $\eta_{0z} = \rho_B V_{pB}$, and $\eta_{mx} = \rho_m V_{pm}$, $\eta_{mz} = \rho_m V_{sm}$, $m = 1, 2, B$.

Table 4.1 Ground properties considered for numerical analyses

	1 st stratum			2 nd stratum		
	$\rho_i(t/m^3)$	$V_{pi}(m/s)$	$V_{si}(m/s)$	$\rho_i(t/m^3)$	$V_{pi}(m/s)$	$V_{si}(m/s)$
ground A	1.5	300	100	1.6	600	200
ground B	1.5	300	100	2.0	1000	300
ground C	1.6	600	200	2.0	1000	300

The ground material properties in Table 4.1 are applied in which ρ_i means density, V_{pi} means longitudinal

wave velocity and V_{si} means transversal wave velocity of each stratum, in which the base stratum is fixed as $\rho_B = 2.0 \text{tm}^3$, $V_{pB} = 3000 \text{m/s}$, $V_{sB} = 800 \text{m/s}$.

Elastic constants of each stratum are determined by the so called PS inspection as follows: Longitudinal elastic modulus, G_{pi} , transversal elastic modulus, G_{si} , and Poisson's ratio, ν_{si} , are determined respectively as

$$\nu_{si} = \frac{(C_{pi}/C_{si})^2 - 2}{2[(C_{pi}/C_{si})^2 - 1]}, \quad G_{si} = \rho_{si} C_{si}^2, \quad E_{si} = 2(1 + \nu_{si}) \cdot G_{si} \quad (4.4)$$

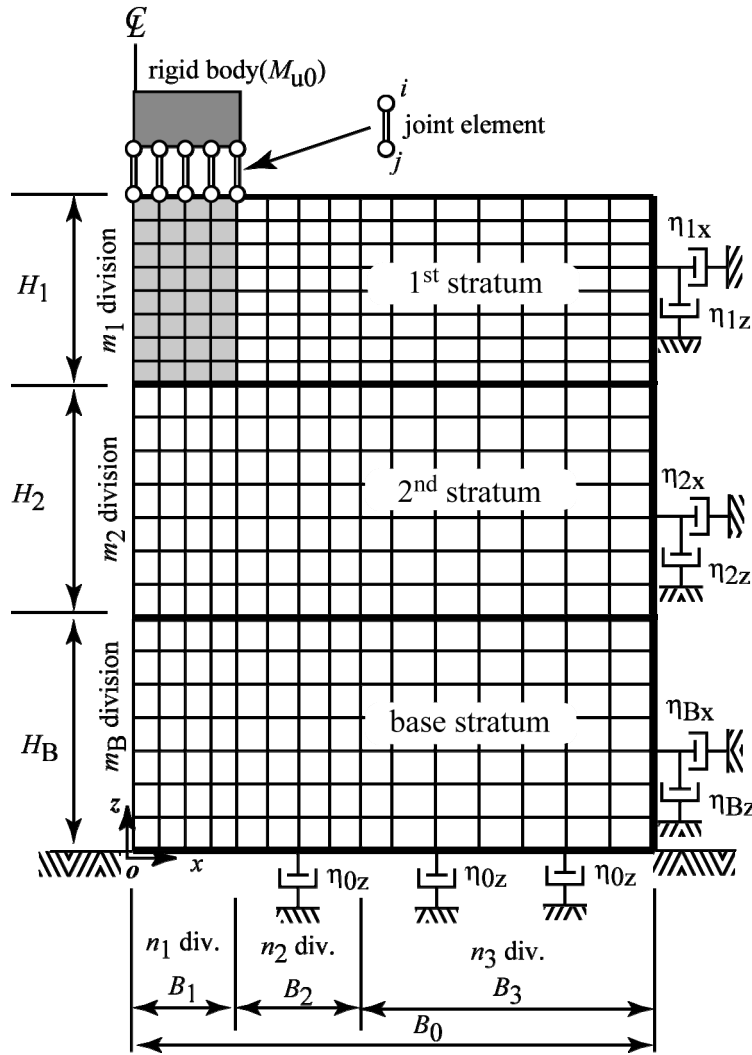


Fig.4.1 Three dimensional axisymmetric FEM element division

Linear elastic relations between stress vector: $\sigma_i = [\sigma_x \quad \sigma_z \quad \tau_{xz} \quad \sigma_\theta]^T$, and strain vector: $\varepsilon_i = [\varepsilon_x \quad \varepsilon_z \quad \gamma_{xz} \quad \varepsilon_\theta]^T$ are given as

$$\sigma_i = \tilde{\mathbf{E}}_i \varepsilon_i \quad (4.5)$$

where,

$$\tilde{\mathbf{E}}_i = \frac{E_{si}(1-\nu_{si})}{(1+\nu_{si})(1-2\nu_{si})} \begin{bmatrix} 1 & \nu_{si}/(1-\nu_{si}) & 0 & \nu_{si}/(1-\nu_{si}) \\ \nu_{si}/(1-\nu_{si}) & 1 & 0 & \nu_{si}/(1-\nu_{si}) \\ 0 & 0 & 0.5(1-2\nu_{si})/(1-\kappa_{si}) & 0 \\ \nu_{si}/(1-\nu_{si}) & \nu_{si}/(1-\nu_{si}) & 0 & 1 \end{bmatrix} \quad (4.6)$$

Numerical calculations are carried out for $H_1 = 10m$, $m_1 = 10$, $H_2 = 20m$, $m_2 = 20$, $H_B = 40m$, $m_B = 20$ and $B_1 = 5m$, $n_1 = 5$, $B_2 = 20m$, $n_2 = 10$, $B_3 = 100m$, $n_3 = 10$, in which the contact area of structural basement and ground surface is taken as $A_0 = \pi B_1^2 = 79m^2$.

First, the static solutions due to the structure's gravity force ($M_{u0} \times g$, where g is gravity acceleration) are found and then those are used as initial conditions for the following time-dependent response analyses. The kinematic equations are solved using an explicit time integration scheme.

$$\mathbf{M}\ddot{\mathbf{u}} + \mathbf{C}\dot{\mathbf{u}} + \mathbf{K}\mathbf{u} = \mathbf{P} \quad (4.7)$$

where \mathbf{u} : nodal displacement vector, \mathbf{M} : mass matrix, \mathbf{C} : damping matrix, \mathbf{K} : stiffness matrix, \mathbf{P} : nodal force vector by the structure's own weight, and dot means time differential.

Figures 4.2(a) and (b) show the ground reactive force responses of structural basement under $M_{u0} = 500ton$ in structure's mass, $v_0 = 0.01m/s$ in incident vertical velocity of the base stratum, and $T_0 = 0.02sec, 0.04sec, 0.05sec, 0.08sec, 0.12sec$ and $0.2sec$ in the incident displacement and velocity period. In those figures, the ground reactive forces of structure oscillate within compressive zone and their maximum compressive forces in cases of $T_0 = 0.04sec$ and $0.05sec$ attain to about two times as large as the structure's own weight being $M_{u0} \times g$ and in the relatively longer period domain of $T_0 \geq 0.12sec$, the peak reactive forces greatly decrease.

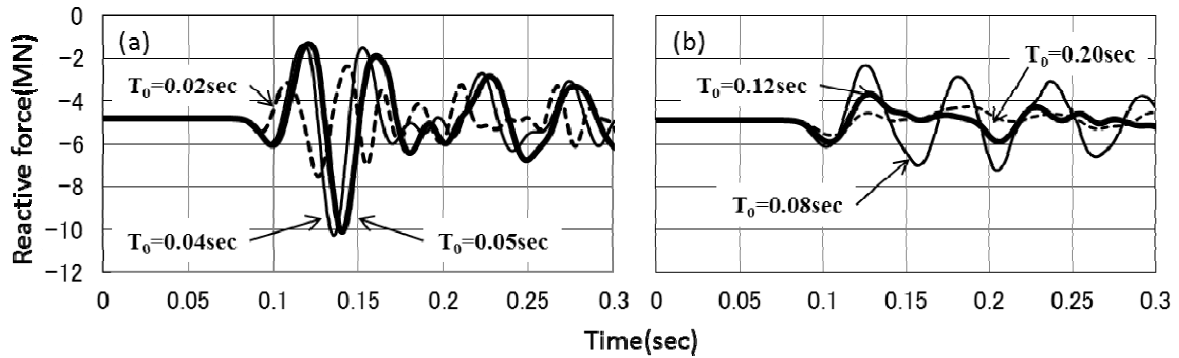


Fig.4.2 Ground reactive force responses of structure (ground A, $M_{u0} = 500ton$, $v_0 = 0.01m/s$)

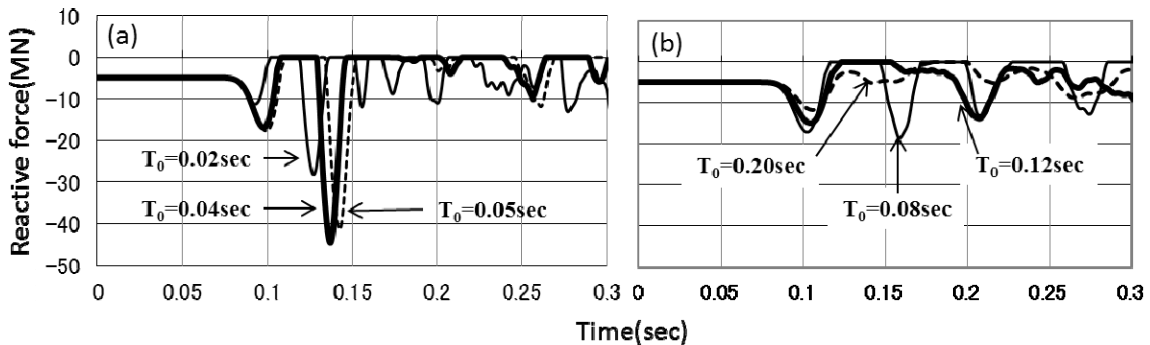


Fig.4.3 Ground reactive force responses of structure (ground A, $M_{u0} = 500ton$, $v_0 = 0.1m/s$)

Similar responses of ground reactive force of the structure when $v_0 = 0.1m/s$ are shown in Figs. 4.3(a), and (b). In this case, the time domains when the reactive ground forces become zero appear and pulse-like compressive reactive ground forces are yielded. It is also noted that the maximum ground reactive forces appear in the second peak rather than that in the first peak in the period domain of $T_0 < 0.08sec$. Since the maximum ground reactive forces attain to about 9 times as large as the static ground reactive force and the duration of compressive forces is very short as $T_0/2$, such a pulse-like ground reactive force may be regarded as a kind of impulsive vertical force against structure.

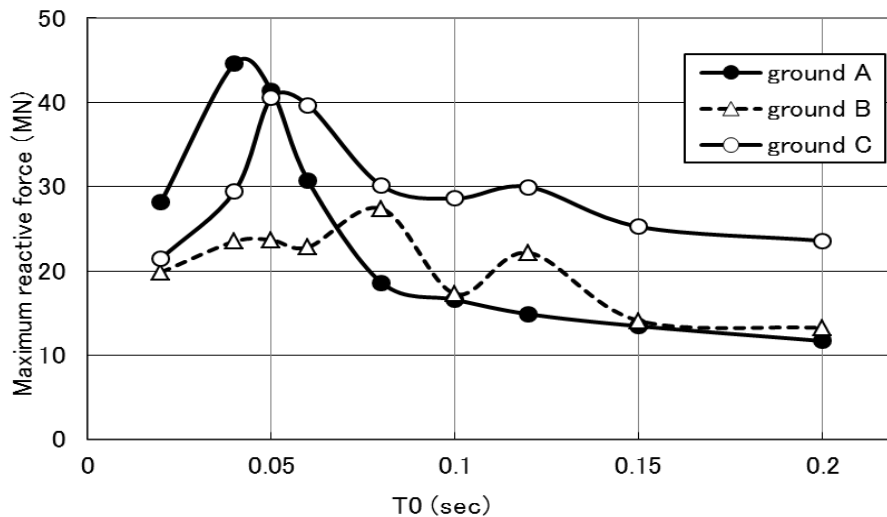


Fig.4.4 Maximum ground reactive forces in grounds A,B and C ($M_{u0} = 500ton$, $v_0 = 0.1m/s$)

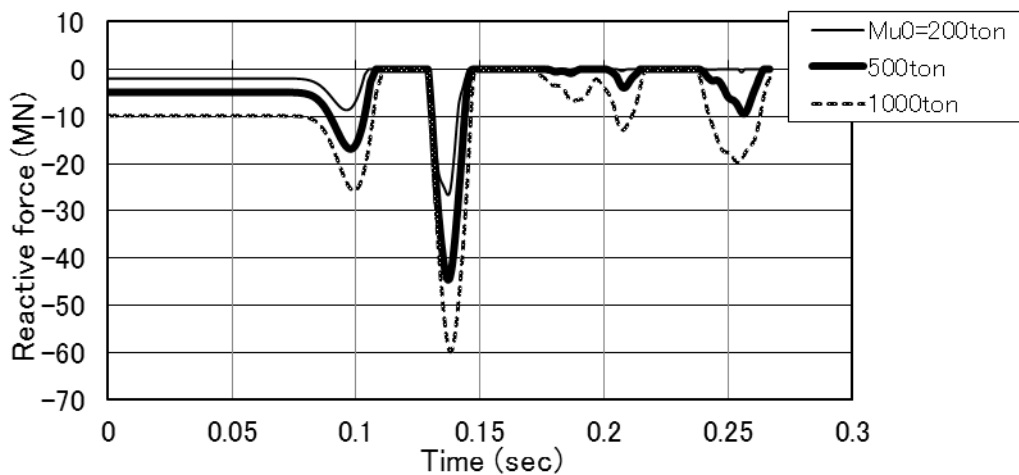


Fig.4.5 Ground reactive forces and structure's masses (ground A, $v_0 = 0.1m/s$, $T_0 = 0.04sec$)

Next, for the grounds A, B and C in Table 4.1 with the structure of $M_{u0} = 500ton$, relation between the maximum ground reactive forces and the period (T_0) of incident velocity being $v_0 = 0.1m/s$ are shown in Fig.4.4 in which the maximum ground reactive forces appear at $T_0 = 0.04sec$ for the ground A, at $T_0 = 0.08sec$ for the ground B and at $T_0 = 0.05sec$ for the ground C, respectively, and those peak values considerably vary by the different ground characteristics. It can be noted, however, that the larger ground reactive forces in comparison with the static reactive force of 4.9 MN appear only in a high frequency zone of $T_0 < 0.08sec$.

Furthermore, to examine influence of the weight of structure on ground reactive force, the cases of $M_{u0} = 200\text{ton}$, 500ton and 1000ton under $v_0 = 0.1\text{m/s}$ at $T_0 = 0.04\text{sec}$ are also calculated and the results of Fig.4.5 are obtained. In this figure, it can be seen that the maximum ground reactive forces become larger as M_{u0} is larger, but the ratio of those to the static ground reactive forces becomes smaller such as 9.1 for $M_{u0} = 200\text{ton}$ and 6.1 for $M_{u0} = 1000\text{ton}$.

5. Axial stress characteristics of viaduct pier column on multi-layered grounds

Here, axial stress characteristics of reinforced concrete column of viaduct pier supported on multi-layered grounds are investigated. The ground properties are same as those in Table 4.1. Same FEM element divisions as Fig.4.1 are applied for the ground part, and for the viaduct pier, a simple model as shown in Fig.5.1 which is consisting of rigid footing and rigid structure and elastic spring for column is applied, in which spring constant of the column is sought as $k_c = E_c A_c / H_c$, where E_c :Yong's modulus of column concrete, A_c :the cross sectional area of column, H_c :height of column.

The incident vertical displacement and velocity at the bottom of base stratum are given by Eqs. (4.1), (4.2) and (4.3).

Figure 5.1 shows the three dimensional axisymmetric viaduct model used here. The column height and cross sectional area are H_c and A_c , respectively. The radius of footing basement is B_1 , and the finite element division for multi-layered grounds are same as Fig.4.1, in which $H_1 = 10\text{m}$, $H_2 = 20\text{m}$, $H_B = 40\text{m}$, $B_1 = 5\text{m}$, $B_2 = 20\text{m}$, and $B_3 = 100\text{m}$.

First numerical example is given for the case of $H_c = 10\text{m}$, $A_c = 3.14\text{m}^2$, the bottom face area of footing is $A_f = 78\text{m}^2$, mass of superstructure (M_{u0}) is 500ton and mass of footing (M_f) is 380ton . Figs 5.2(a) and (b) show axial stress response of column with $H_c = 10\text{m}$ under $v_0 = 0.1\text{m/s}$ for the ground A in Table 4.1. The maximum intensity of axial column stress appears at $T_0 = 0.04\text{sec}$ or 0.05sec , which attains to 20MPa in compression and 19MPa in tension. Figure 5.3 shows relation between the peak stress intensities and periods (T_0) for the grounds A, B and C in Table 4.1. It can be seen that high stress intensities only appear in the vicinity of $T_0 = 0.05\text{sec}$ and in the frequency zone of $T_0 > 0.08\text{sec}$, those intensities much diminish. On the other hand, Fig.5.4 shows a similar relation for the case of $H_c = 20\text{m}$ and $A_c = 3.14\text{m}^2$. The peak column stress intensities become lower than those in Fig.5.3 for $H_c = 10\text{m}$, but the zone inducing a large stress intensity expands.

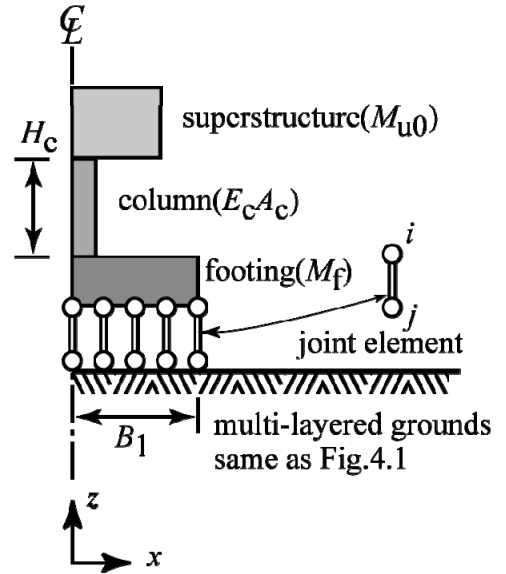


Fig.5.1 Viaduct pier model on multi-layered grounds

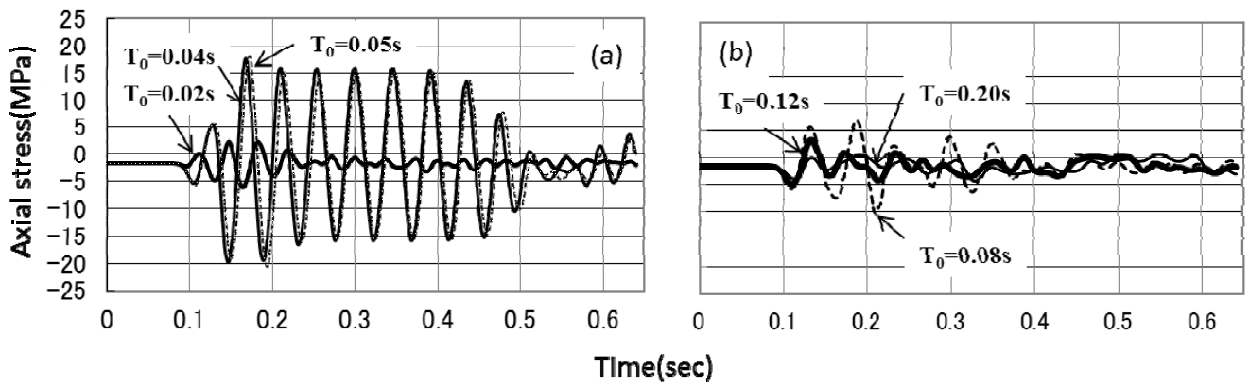


Fig.5.2 Axial stress responses of column under $v_0 = 0.1\text{m/s}$ (ground A, $H_c = 10\text{m}$)

Eigen period of viaduct pier of Fig.5.1 with the footing base fixed can be estimated by

$$T_{st0} = 2\pi \sqrt{\frac{M_{u0}}{k_c}}, \quad k_c = \frac{E_c A_c}{H_c} \quad (5.1)$$

where, T_{st0} :eigen-period, E_c :Young's Modulus of column, k_c :spring constant. Putting $M_{u0} = 500$ ton, $A_c = 3.14m^2$, and $E_c = 30GPa$, one obtains $T_{st0} = 0.046$ sec for $H_c = 10m$ and $T_{st0} = 0.065$ sec for $H_c = 20m$. Therefore, considering the predominant period (T_{G0}) for ground reactive forces as shown in Fig.4.4, it can be regarded that the axial stress amplitude of column enlarges by a kind of resonance by T_{st0} and T_{G0} .

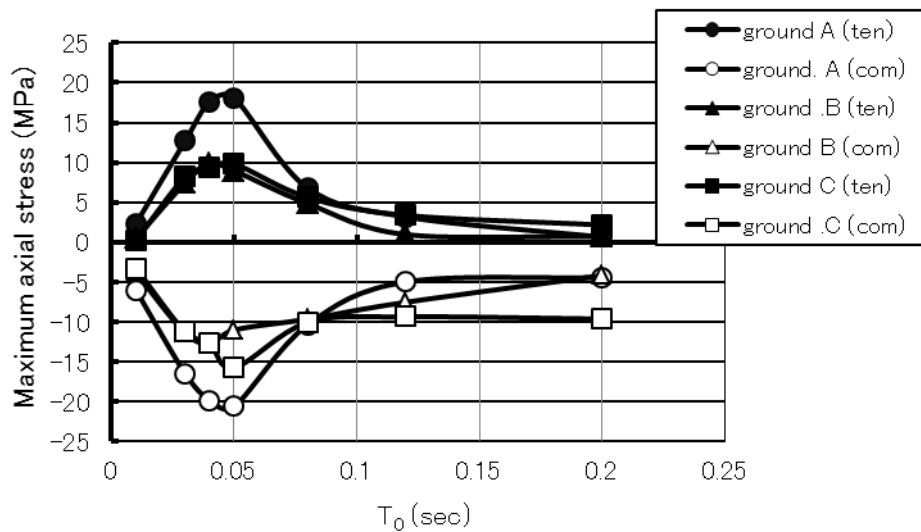


Fig.5.3 Maximum axial stress intensities of column with $H_c = 10m$ (under $v_0 = 0.1m/s$)

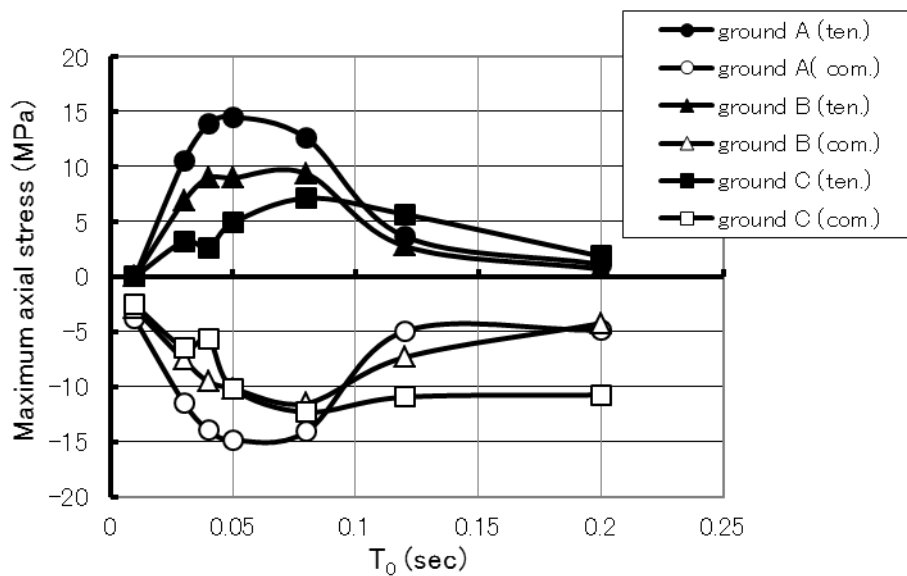


Fig.5.4 Maximum axial stress intensities of column with $H_c = 20m$ (under $v_0 = 0.1m/s$)

Summarizing the results of Figs 5.3 and 5.4, we can mention that the maximum tensile stress intensities being 15 or 19 MPa that appear in the vicinity of $T_0 = 0.05 \text{ sec}$, are sufficient to induce a tensile fracture of column concrete under $v_0 = 0.1 \text{ m/s}$. Therefore, it may be expected that, by the acting of repeated tensile and compressive stresses, a tensile and compressive combined fracture mode is induced in a viaduct reinforced concrete column section, which were observed at Hyogo-ken Nanbu earthquake.

5. Summary

- (1) Stress wave propagation characteristics within a multi-layered elastic grounds consisting of top alluvium stratum, middle diluvium stratum and base stiff stratum were investigated using one dimensional elastic wave theory. The vertical stress intensities were much influenced by the ground property and the incident velocity wave period, T_0 , in the base stratum. Noticing the interface of top and middle strata, significant large vertical stress intensities appeared in the short period zone such as $T_0 < 0.2 \text{ sec}$, while those intensities diminishes greatly as larger than $T_0 = 0.2 \text{ sec}$.
- (2) First, applicability of numerical simulation method using a lumped mass-spring model was examined as a preliminary study. Following the characteristics of ground reactive forces of an overloaded structure on the top ground surface were investigated by three dimensional axisymmetric FEM analyses. As the results obtained, in the case of $v_0 = 0.01 \text{ sec}$, where v_0 is the incident velocity of the bottom of base stratum, the ground reactive forces of structure remained within a compressive region, but in the case of $v_0 = 0.1 \text{ sec}$, the dynamic ground tensile forces exceeded the static ground compressive forces and a pulse-like ground compressive reactive force was formed in the high frequency zone of $0.02 \text{ sec} < T_0 < 0.08 \text{ sec}$. The peak value of such a pulse-like ground reactive force became much larger as the own weight of structure increased.
- (3) The last numerical analyses were devoted to investigate the axial stress characteristics of a viaduct pier column on the multi-layered grounds. The ground models were the same ones used before and a simple model of viaduct pier consisting of rigid structure, rigid footing and a elastic spring for the column were applied. The numerical examples indicated that the significant large stress intensities of column section appeared when the incident velocity wave period was near the vertical eigen period of the viaduct column. Therefore, it can be said that a reinforced concrete viaduct column is apt to fracture in a combined tensile and compressive mode by a resonance effect of vertical vibration in both the multi-layered grounds and the viaduct pier column.

6. Acknowledgements

The authors express much appreciation for valuable discussions with Shunsuke Sakurai, Professor Emeritus of Kobe University and Taijiro Nonaka, Professor Emeritus of Kyoto University.

7. References

- 1) The 3rd Port Construction Bureau of the Ministry of Transportation in Japan: Restoration document of Seismic disaster in Kobe Port (1998) (in Japanese)
- 2) K. Kanai, *Bull. Earthq. Res. Inst.*, **35**, 457 (1957)
- 3) K. Sonoda, H. Kobayashi, and T. Nakajima, On Quasi-impact Failure of Civil Engineering Structures by Earthquake, *Symposium on Damage to Structures by Impulsive Effects of the Hyogoken-Nanbu Earthquake*, Architectural Institute of Japan (1997) (in Japanese)
- 4) K. Sonoda, N. Takada, and H. Kobayashi, *Proceedings of Second International Conference on Earthquake Resistant Engineering Structure (ERES)*, WIT Press, Southampton, UK, pp.83-92 (1999)

Applicability of Strain Softening Analysis for Tunnel Excavation

Kenichi NAKAOKA* and Hiroaki KITOH**

(Received October 2, 2015)

Synopsis

As a one of alternative model to predict the behavior of tunnel excavation in unconsolidated ground, the strain hardening up to softening model has been proposed in this paper. The model based on plastic theory has been formulated, not in ordinary stress space but in strain one because of consistent unloading definition due to strain softening. Material model parameters were estimated from unconfined and tri-axial compression tests. After the defined model parameters applied into FEM procedure, centrifuge test model has been simulated. As the results, obtained surface settlement and lateral face displacement were well agreed with experimental results. Furthermore, the distribution of predominant shear strain around tunnel obtained was also comparable with the sliding phenomena observed in the experimental test. In conclusion, the proposed model can be applicable to tunnel stability problem in unconsolidated ground.

KEYWORDS: Strain softening, Lade model, Finite element analysis, Tunnel face stability, Strain-space

1. Introduction

New Austrian Tunneling Method: NATM is being increasingly used for excavation of shallow tunnels within unconsolidated soils. The main reason is that the lower cost for tunnel construction than that by shield tunneling method and lower impact for traffic than that by open cut method around the construction site.

Some reports have indicated that a tunnel excavation by NATM within unconsolidated soil often expands the high shear zone, called, “shear band,” from the tunnel sides upward¹⁾. And by experiment it was shown that the “shear band” expands also from tunnel face towards surface samely²⁾. If this zone approaches the surface, it can cause large settlement of surface above the tunnel and lead to tunnel collapse in the worst case. Therefore a numerical model is required that can simulate the expanding of the shear band to determine the stability of a tunnel in unconsolidated soil. Usually, however, normal elastic^{ex.3)} or elasto-plastic models^{ex.4)} are used in the analysis of tunnel stability, so it is insufficient to evaluate behavior of ground around the tunnel. It is not easy to observe the extension of actual shear bands or to simulate experimentally. So, validation of strain softening model for the evaluation of extension of shear band is not progressing. It is considered the reason that the model does not become widely used as the analysis method for a design. Therefore, it is important to increase the validation example about the extension of shear band.

Lee⁵⁾ and Akutagawa⁶⁾ developed a strain softening model to predict ground behavior taking into account the shear band caused by tunnel excavation. And applied to evaluation the expanding of shear band from actual tunnel sides upward. After that, it was shown that the strain softening model can simulate the surface settlement that was considered to have been caused by the shear band. Nakaoka et al⁷⁾ expanded the model to three dimensional problem, and it was shown that the model can simulate the discontinuous displacement developed from tunnel face in centrifugal experiment that was carried out by Takahashi et al⁸⁾.

The manner of this model is that, if material yielded, stress is redefined by shrinking of Mohr’s stress circle to fit into the Mohr-Coulomb criterion line. The strain softening is taken account by reducing the cohesion and internal frictional angle according to maximum shear strain. Also, the anisotropy is considered by decreasing of shear stiffness on local coordinates along a slip line in consideration of shear band developing. The model doesn’t use dilatancy parameter, so the model became simple mathematically, and increase a practicality.

On the other hand, it is considered that the numerical model based on plastic theory that was developed for simulation of the soil behavior will become one of the choices for design of tunnel in unconsolidated ground. However the numerical model like that was not investigated whether it can simulate correctly the shear band around the tunnel. Then, we focused on the numerical model that was developed by Lade⁹⁾ (Lade model). This model intended for evaluation of non-cohesive sandy soil. And by taking into the plastic work as an index, this model can simulates strain hardening and softening seamlessly.

The model is newly added the cohesion term for cohesive soil. A strain-space-based plasticity formulation

* Student, Doctor Course of Department of Civil Engineering (Obayashi Corporation)

** Professor, Department of Urban Engineering, Osaka City University

is used to represent strain hardening and softening behavior completely. After that the numerical model is mounted on the code of finite element method (FEM), and applicability is ascertained by simulating about the centrifuge tests of tunnel model.

In this paper, at first, Lade model that takes into account of cohesion is outlined. And, the parameters such as for strain hardening and softening are estimated by fitting to strain-stress curve of unconfined and tri-axial compression tests using the same compounding material with soil in tunnel model. After that, the centrifuge model tests⁸⁾ are simulated with parameters obtained as previously shown, and by comparing analysis results with model tests, applicability of the numerical model is discussed.

2. Strain hardening and softening model

(1) Strain softening model

Lade proposed an elasto-plastic constitutive model that was specified the strain hardening and softening formation to present the nonlinear behavior of non-cohesive soil⁶⁾. Using parameters of the numerical model that was estimated by tri-axial compression tests, he showed that the model can simulate well the strain hardening and softening behavior of non-cohesive soil. Mizuno¹⁰⁾ studied about applying the model on concrete material, the strain hardening and softening behavior of concrete in tri-axial compression test under low confined stress which was from 0.3 to 1.2% of uniaxial compressive strength was simulated⁷⁾. Mizuno described an elasto-plastic constitutive law that involves strain hardening and softening should be formulated in strain-space.

In this study, we apply the Lade model modified by Mizuno using strain-space-based plasticity formulation. Denoting that the loading function f in stress-space and F in strain-space respectively, and corresponding increment df and dF according to increment of stress $d\sigma_{ij}$ and increment of strain $d\varepsilon_{ij}$ are represented as shown in Eq.1 and Eq.2.

$$df = \frac{\partial f}{\partial \sigma_{ij}} d\sigma_{ij} \quad (1)$$

$$dF = \frac{\partial F}{\partial \varepsilon_{ij}} d\varepsilon_{ij} \quad (2)$$

As shown in right half of Fig.1, when $df > 0$, it means hardening by loading. On the other hand, when $df < 0$, it means elastic unloading or unloading by softening. It cannot determine which is the real state of unloading only by the stress. As shown in left half of Fig.1, applying the loading function defined in strain space, it means elastic unloading with $dF < 0$. On the other hand, it means hardening or softening by loading with $dF > 0$. There is no need to distinguish which is the state of loading. Strain hardening and softening are described in constitutive law continuously in strain space. Thus, the problem seen in formulation in stress space can be solved. Loading function applied in this study is represented by Eq.3 in stress-space.

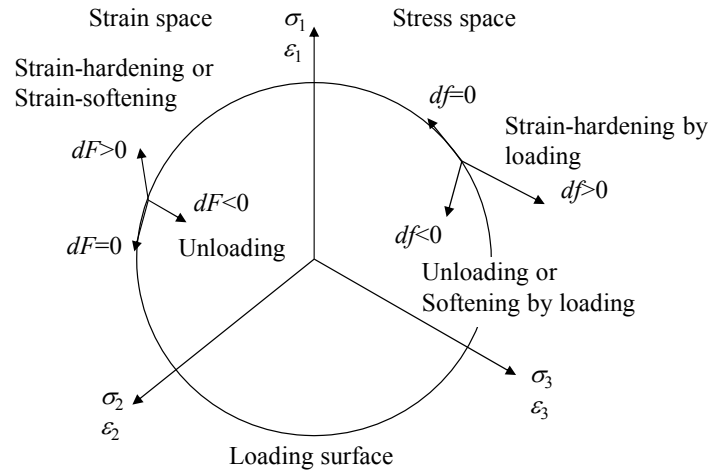


Fig.1 Stress state in stress-space and strain-space

$$f = (I_1 + a)^3 - \left(27 + f_p \left(\frac{P_a}{(I_1 + a)} \right)^m \right) \times \left(\frac{1}{27} (I_1 + a)^3 - \frac{1}{3} (I_1 + a) J_2 + J_3 \right) = 0 \quad (3)$$

Here, the meanings of the parameters in equation are shown below:

a : As shown in Fig.2, the amount of parallel shift of the yield surface along hydrostatic axis in tensile direction.

m : Curvature of the yield surface. If $m = 0$, the distance between yield surface and hydrostatic axis becomes linear relationship with respect to hydrostatic pressure. If $m > 0$, the relationship becomes concave down with respect to hydrostatic pressure. And if $m < 0$, the relationship becomes concave up.

f_p : Strain hardening and softening, parameter, which is defined as a function of plastic work W_p . The parameter defines the material strength, the value is 0 initially. It increases owing to hardening and becomes maximum value η_1 when the corresponding stress attains at its peak. Afterward, it decreases with softening.

P_a : pressure of the atmosphere.

I_1, J_2, J_3 are the stress invariants, these are shown in Eqs.4 ~ 6, respectively, using strain invariants.

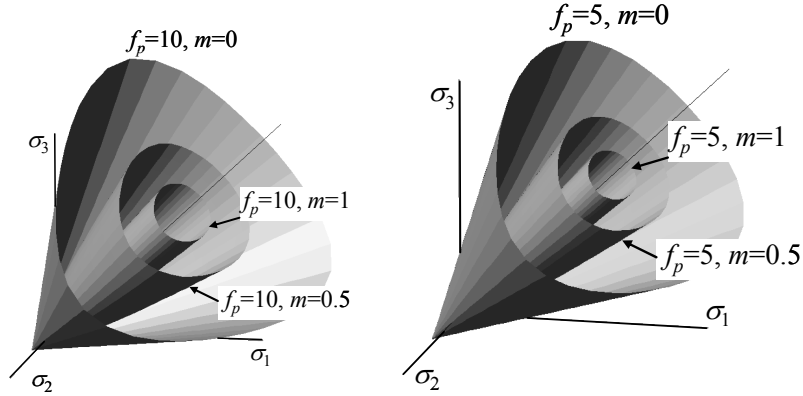


Fig.2 Lade loading surface according to m and f_p

$$I_1 = \sigma_{ii} = 3K(\varepsilon_{ii} - \varepsilon_{ii}^p) = 3K\bar{I}_1 = \bar{A}\bar{I}_1 \quad (4)$$

$$J_2 = \frac{1}{2} s_{ij} s_{ij} = 2\mu^2 (e_{ij} - e_{ij}^p)(e_{ij} - e_{ij}^p) = \bar{B}\bar{J}_2 \quad (5)$$

$$J_3 = \frac{1}{2} s_{ij} s_{jk} s_{ki} = \frac{8}{3} \mu^3 (e_{ij} - e_{ij}^p)(e_{jk} - e_{jk}^p)(e_{ki} - e_{ki}^p) = \bar{C}\bar{J}_3 \quad (6)$$

The loading function in strain space is described as Eq.7.

$$F = (\bar{A}\bar{I}_1 + a)^3 - \left(27 + f_p \left(\frac{P_a}{(\bar{A}\bar{I}_1 + a)} \right)^m \right) \times \left(\frac{1}{27} (\bar{A}\bar{I}_1 + a)^3 - \frac{1}{3} (\bar{A}\bar{I}_1 + a) \bar{B}\bar{J}_2 + \bar{C}\bar{J}_3 \right) = 0 \quad (7)$$

$$\bar{A} = 3K \quad (8)$$

$$\bar{B} = 4\mu^2 \quad (9)$$

$$\bar{C} = 8\mu^3 \quad (10)$$

Where, $\varepsilon_{ij}^p, e_{ij}, e_{ij}^p$ means plastic strain, deviator strain, deviator plastic strain respectively. K and μ are elastic volumetric modulus and shear modulus, respectively

$$K = \frac{1}{3(1-2\nu)} \quad (11)$$

$$\mu = \frac{1}{2(1+\nu)} \quad (12)$$

(2) Procedure of non-linear calculation

A finite element method: FEM is used for this study. The method of calculation of non-linearity is to apply a gradually increasing load. Fig. 3 is the flowchart of the calculation.

Modified Newton Raphson scheme is employed to converge residual force. The scheme is as follows: At first, overall stiffness matrix K is made, and strain increment $\Delta\varepsilon$ is obtained with K and increment of load Δf_{load} . Next, plastic strain $\Delta\varepsilon^p$ is obtained by elasto-plastic constitutive equation using the previous values of $\Delta\varepsilon$, and ε^e and W_p to be explained in detail. Now, it is possible to obtain the current stress increment: $\Delta\sigma = D\Delta\varepsilon^e$, where D is elastic stiffness matrix, and $\Delta\varepsilon^e = \Delta\varepsilon - \Delta\varepsilon^p$ is relevant elastic strain in increment. Then the current stress: σ updated owing to the obtained increment. Residual force of next step is estimated from σ obtained as above. Stress of next step is obtained by loading the residual force. Again, σ is changed by the $\Delta\sigma$ that is calculated under new σ . Residual force generated by stress change is calculated again. When the maximum residual force becomes less than allowable value, the calculation is terminated.

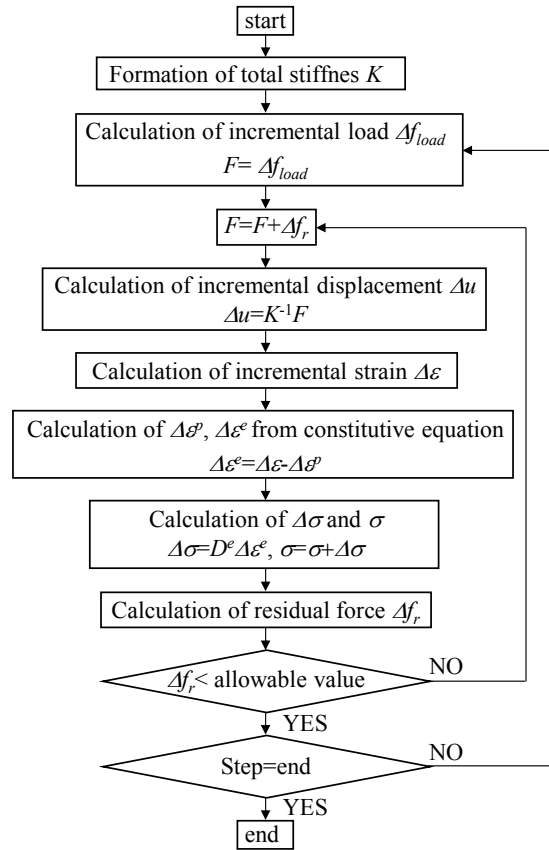


Fig.3 Flowchart of non-linear analysis

3. Defining of model parameters

(1) The parameters and procedure of definition

The parameters were defined using the results of unconfined and tri-axial compression test. Test specimens had the same composition as the material applied to the centrifuge model experiment⁸⁾. The material was soil cement as mixture of low plasticity kaolin clay and cement. Kaolin clay is an article on the market, which plastic index: IP=10%. Cement content was 100kg/m³ to become the unconfined compressive strength 70kPa of target strength. Fig. 4 shows the proceeding of each parameters definition.

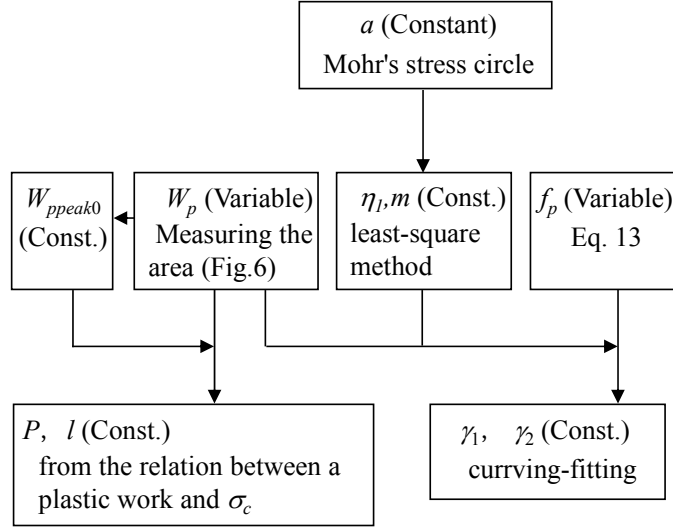


Fig.4 Procedure of parameters setting

Material parameters were as follows: Young's modulus $E=16.6\text{MPa}$, Poisson's ratio $\nu=0.4$, and as the parameters that define the loading function, a and m these define the shape of curved surface, f_p that is the parameter of material strength, η_1 that defines the maximum value of f_p , and the parameters $W_{pppeak0}$, P , l , γ_1 , γ_2 to link f_p and plastic work W_p . Eq. 13 shows the relation between f_p and W_p . The number of the essential parameters was eight.

$$f_p = \eta_1 \left(\frac{e \cdot P_a}{W_{pppeak}} \right)^{\frac{1}{\gamma}} \times \exp \left(- \frac{W_p}{\gamma W_{pppeak}} \right) \times \left(\frac{W_p}{P_a} \right)^{\frac{1}{\gamma}} \quad (13)$$

$$W_{pppeak} = P \left(\frac{\sigma_c}{P_a} \right)^l P_a + W_{pppeak0} \quad (14)$$

$$\gamma = \gamma_1 \sigma_c + \gamma_2 \quad (15)$$

Here, σ_c is confined pressure of the triaxial compressive test. On the FEM calculation, the average of maximum principal stress and intermediate principal stress was used as confined pressure in which negative value means compression. The relation between strain and stress that was obtained by the unconfined compression test and the triaxial compression test is shown together with the results of calculation later. And to be consistent with the results of the uniaxial compression test, it was multiplied by a constant on the results of the triaxial compression test. To define the parameter, the results obtained in this way were used.

(2) Definition of each parameter a , m , η_1

The first parameter a is the shift distance of curved surface of loading function along the hydrostatic axis as Fig.2, which was estimated as the intersection point of envelope line and σ axis shown in Fig.5. The parameter a is an absolute value. From Fig.5, it was estimated to be 532kPa.

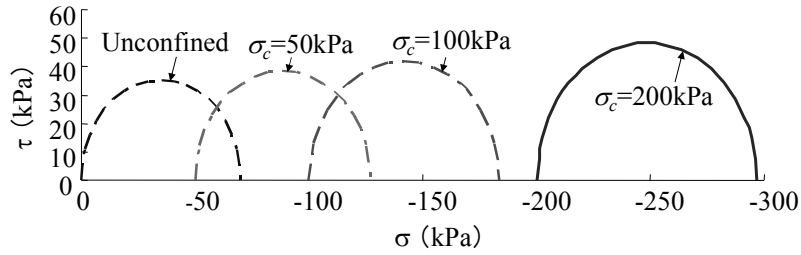


Fig.5 Mohr's stress circle at each confining stress

The parameter η_1 and m represent peak strength and curvature of loading surface respectively; those were estimated by the assigning parameter a that described above to plastic-potential function. After that, parameter m and η_1 were adjusted to minimize the standard variation of η_1 that is obtained by each of the element tests. From element tests, it was set to $m=1.08$, $\eta_1=7.10$.

(3) Definition of each parameters W_{ppeak0} , P , l

Plastic work is estimated from strain-stress curve obtained from the compression tests. Here, it is assumed that the material is in elastic state when unloading. The plastic work can be obtained by measuring the area of hatching in Fig.6.

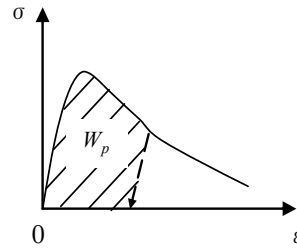


Fig.6 Work of plasticity

W_{ppeak} is the plastic work when difference of principal stress by tri-axial compression test becomes maximum. W_{ppeak0} is also the plastic work when axial stress of unconfined test becomes maximum. Table 1 shows the W_{ppeak0} values estimated from the results of each test. By using the parameters of W_{ppeak0} , P and l , W_{ppeak} under confined pressure σ_c can be calculated by Eq.14. From relationship between $(W_{ppeak0} - W_{ppeak})/P_a$ and σ_c/P_a in double logarithmic plot shown in Fig.7, P and l were estimated by least-square technique as $P=0.00779$ and $l=0.761$. If the values of W_{ppeak0} , P and l are increased, strain at peak stress is increased.

Table 1 W_{ppeak} (kPa)

Confined Pressure σ_c (kN/m ²)	W_{ppeak}
0	0.66
50	1.07
100	1.56
200	1,82

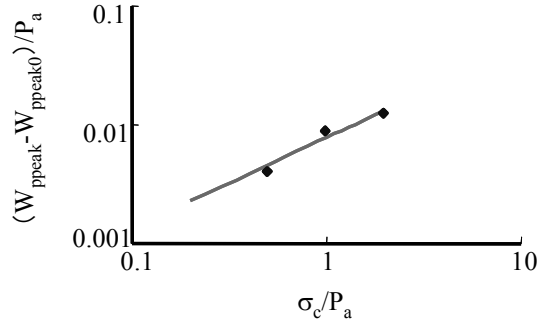


Fig.7 Relation of $(W_{peak0} - W_{peak})/P_a$ and σ_c/P_a

(4) Definition of each parameters γ_1, γ_2

Among the parameters included in the function f_p shown by Eq.3, γ value mainly defines the gradient of strain-stress curve after peak. It is assumed that γ is proportional to the confining pressure σ_c as shown by Eq.15. Procedure of defining γ is as follows. At first, measured value f_p is calculated by assigning the parameters a and m to the loading function that is shown as Eq.3. Next, the parameters η_1, W_{peak0}, P and l are assigned into Eq.13 and Eq.14. And by curve-fitting which is done to conform the calculated value of f_p to the measured value, γ is estimated. Fig. 8 shows the results of the curve-fitting. γ obtained under each confining pressures are shown in Fig.9. However, γ becomes large value unrealistically because softening did not occurred almost in the case of the confining pressure=200kPa. So the case was eliminated. Parameter γ_1 as the gradient of relationship between σ_c and γ was defined as 0.130 from the figure. Also, the intercept γ_2 was defined as 0.453. Table 2 shows the parameters set as explained.

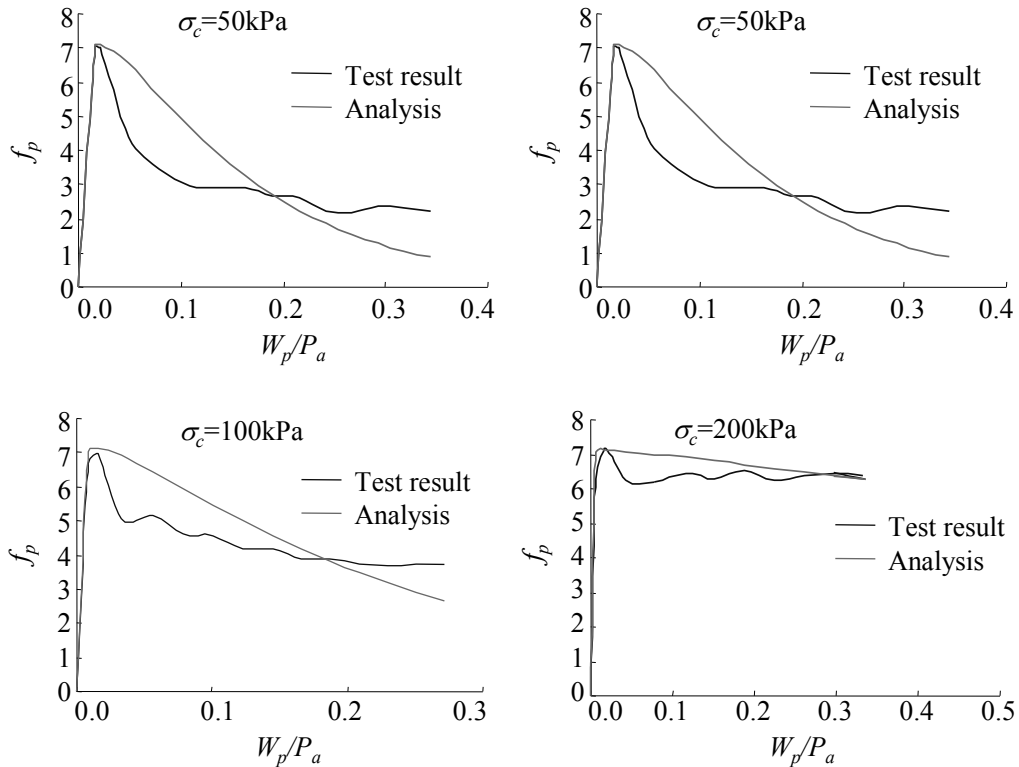


Fig.8 Relationship between W_p and f_p that obtained by curve-fitting

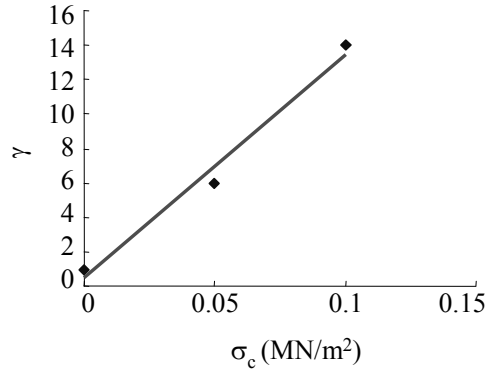


Fig.9 Relationship between γ and σ_c

Table 2 The parameters for numerical simulation

Parameters	value
the amount of parallel shift (a)	0.532 MPa
Degrees of loading function curvature (m).	1.08
the maximum value of f_p (η_1)	7.1
Relation between W_{ppeak} and σ_c (P)	0.00779
Relation between W_{ppeak} and σ_c (P)	0.761
Relation between f_p and W_p (γ_1)	130 m ² /MN
Relation between f_p and W_p (γ_2)	0.453
The value of W_{ppeak} at $\sigma_c = 0$	6.57×10^{-4} MPa
Atmospheric pressure (P_a)	0.101 MPa
Young's modulus (E)	16.6MPa
Poisson's ratio (ν)	0.4
Density (ρ)	1740 kg/m ³

4. The results of numerical analysis

(1) The results of simulation of element test

Fig. 10 shows the results of both simulation of the unconfined compression tests and the tri-axial compression tests. The results of simulations of unconfined tests were similar with the test results. The results of peak strength by simulation of tri-axial compression tests were also similar with the test results. The obtained gradients after peak, however, were slower than those from the test results.

As shown in Fig. 8, we tried to fit the simulation results with actual measurement, but a difference still remained. It is considered that this is the reason of difference between numerical simulation and test results in Fig. 10. Because peak stress is in agreement, and analysis results approach test results as strain increases, we expected that the numerical analysis could obtain the similar results with the experiment.

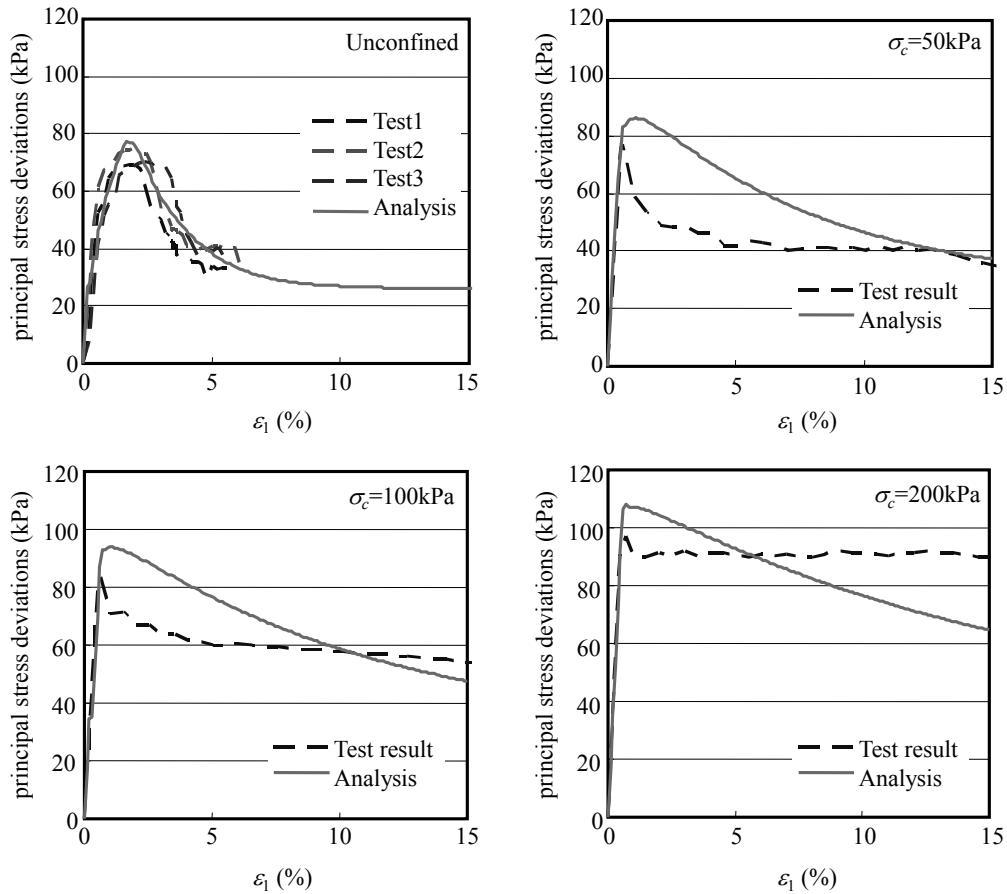


Fig.10 The results of simulation of unconfined compression and triaxial compression tests

(2) Numerical simulation of centrifuge model tests

(a) Outline of the tests

The tunnel model for centrifuge is shown in Fig.11 and Fig.12⁸⁾. Model ground was installed in steel container, called container hereafter as shown in Fig.12. The half hole was created in the model ground as the tunnel face from the start. After that, centrifugal acceleration was gradually increased up to 80G. The shape of tunnel is hemicycle and its diameter was 10cm as shown in Fig.11. When acceleration attained to 80G, It correspond to tunnel diameter of 8m and earth covering of 16m. The tunnel was regarded as a half pipe of right side toward the tunnel face. Tunnel body except 5cm interval close to the face was supported by acrylic half pipe. The support prevented a collapse of tunnel body before the collapse of tunnel face focusing on in this experiment. Front face of container was covered by acrylic board to measure the displacement of ground through the board.

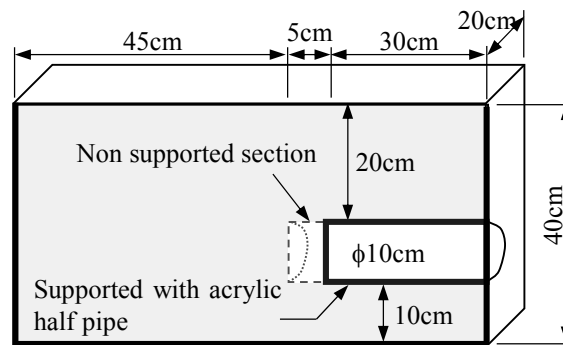


Fig.11 Tunnel face of centrifuge model tests

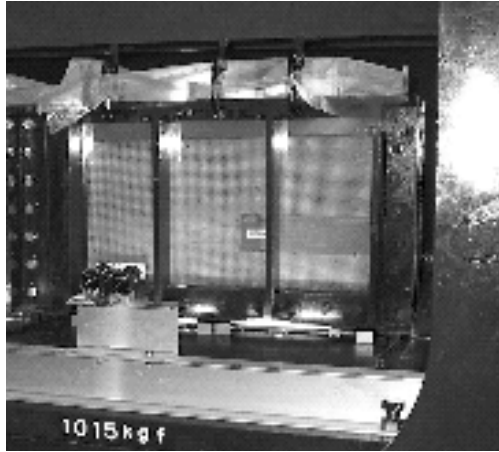


Fig.12 The model on loading stage⁸⁾

Settlement of ground surface just above the tunnel face and lateral displacement of center of tunnel face were measured. It is targeted the experiment condition close to undrained by not installing the drainage in the container.

(b) Analytical model

Fig. 13 shows analytical model, in which the view point of displacement for comparison with the experiment is shown. Dimension of analysis model was same as the experimental model.

Tunnel supporting was also modeled by solid elements as shown in Fig.13, and the relevant elements were assigned enough high elasticity compared to elements for ground. As the boundary condition, displacement of model bottom was fixed, and normal direction of surface around the model was also fixed. It is not assigned boundary condition in ground surface. All load of numerical analysis was dead load of ground. Gravity acceleration was increased gradually up to 80G as same as the experiment. The total number of increment step was 100.

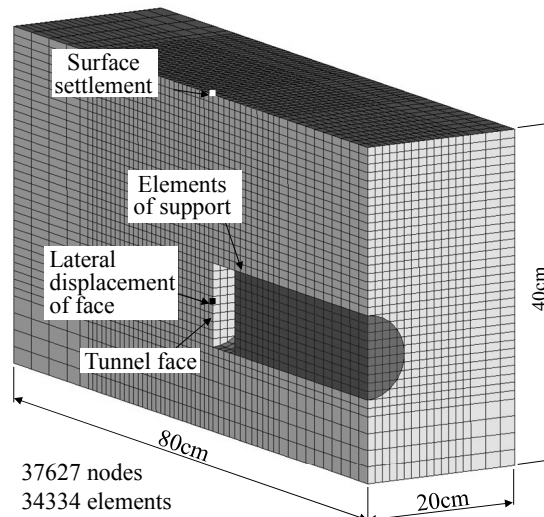


Fig.13 Finite element mesh

(c) Analysis results

Fig. 14 shows relation between centrifuge acceleration and settlement, and also another relation between acceleration and lateral displacement. For reference, it also shows the results of elastic analysis. From the experimental results (○), we can see the rapidly increasing of displacement at about 55G. Elastic analysis indicated with straight lines could not follow naturally such the behavior. On the other hand, settlement gradient of analysis indicated with blue line curve increased at about 50G. Finally, the obtained settlement reached 16mm at 80G. It can be seen that the analysis evaluated the settlement obtained by experiment well.

Lateral face displacement of the experiment rapidly increased at about 55G similarly with the settlement. After that, at about 70G, a crack extended from bottom of the face upward. Finally it caused a collapse.

According to analysis indicated with red curve, lateral displacement increased rapidly at about 50G. It simulated well the lateral face displacement of the experiment.

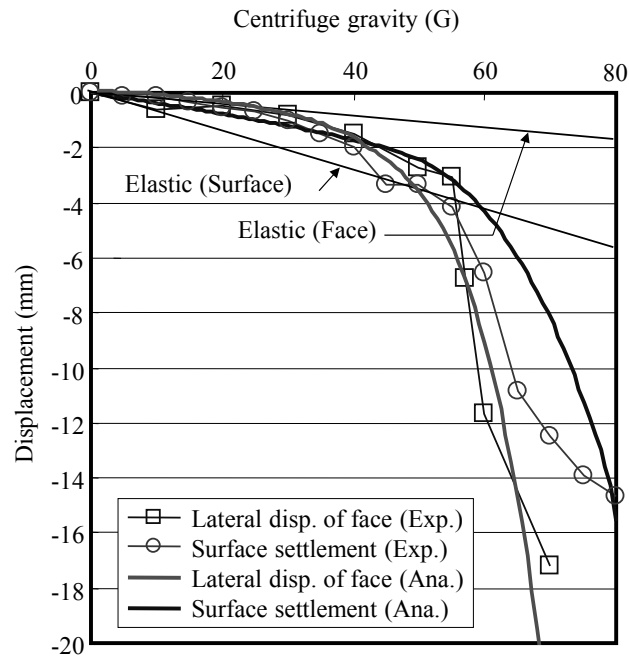


Fig.14 Comparison between results of analysis and experiment

Fig. 15 shows the crack location obtained by experiment when acceleration was 50G. Also, the distribution of maximum shear strain at 50G obtained by analysis is shown together.

At 40G, crack as broken line in experimental model extended upward from bottom of the tunnel face where the stress concentrated. At 50G, the crack as solid line reached to crown of the face. As the obtained result, shear strain in the bottom and top of the tunnel face was larger than 5%. Crack and large shear strain area were limited in location close to the face in this stage. We could not find the behavior that these region extending upward beyond the face crown.

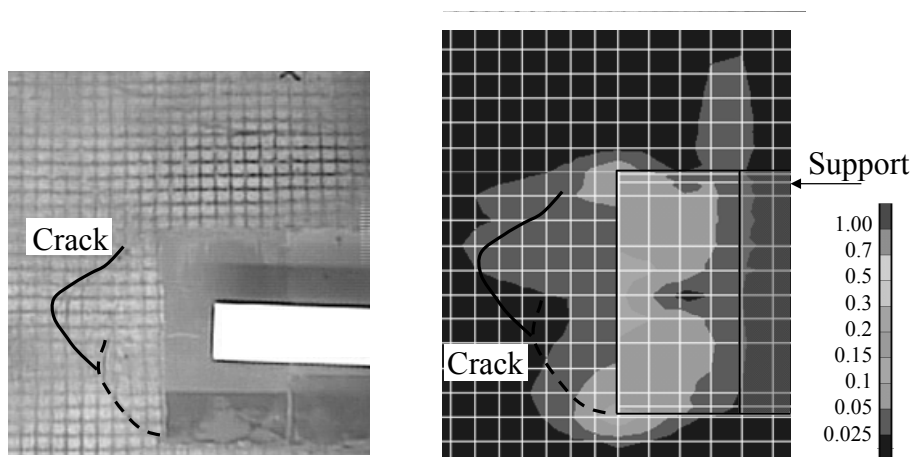


Fig.15 Left: cracking of the experimental model in 50G⁸⁾, Right: distribution of maximum shear strain by analysis in 50G

Fig. 16 shows the experimentally obtained crack location and calculated maximum shear strain distribution at 80G. With the experimental model, crack extended upward from bottom of tunnel face, and finally it led the collapse of tunnel face. Also, crack extended vertically from the edge of near the tunnel face. Also by the analysis, high strain region extended upward from front of the tunnel face and from edge of acrylic support, the region which is called shear band. So, it could be drawn that the numerical model simulates the behavior of the experimental model well.

The crack from the edge of acrylic support in the experimental model did not reach to surface of ground. On the other hand, the shear band in analysis reached to surface. The reason of this difference is that there are some blocks fell into the tunnel discontinuously from around of the tunnel face in the experimental model. So, mass load of fell blocks do not apply to upper ground of tunnel.

On the other hand, a behavior that fall of discontinuous block cannot be simulated in the numerical model, so the load acting on the upper ground does not decrease. It is considered that the load acting on upper ground of numerical model become larger than experiment. So shear band in the numerical model reached to surface whereas crack in the experimental model did not reach.

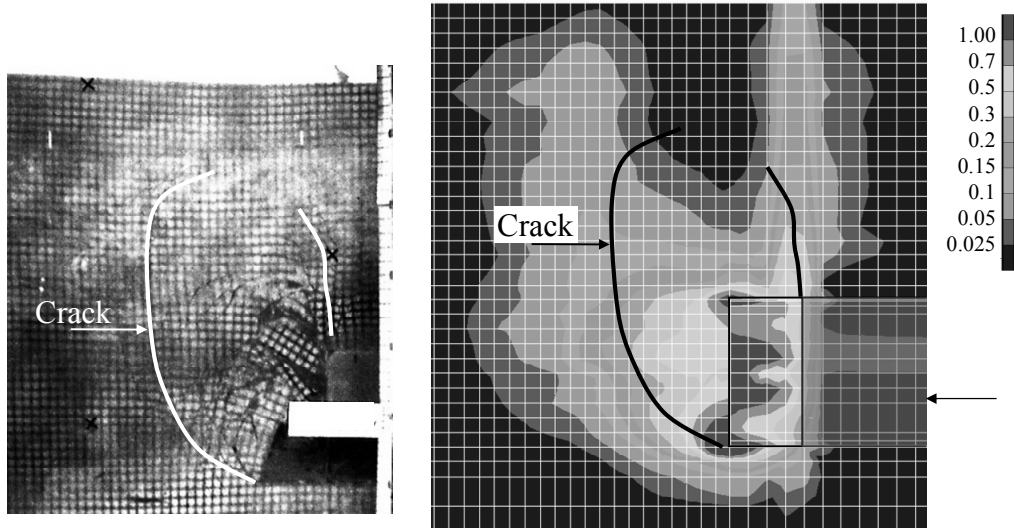


Fig.16 Left: cracking of the experimental model in 80G⁸⁾, Right: distribution of maximum shear strain by analysis in 80G

Fig. 17 shows the displacement by analysis at 80G. From the figure, it can be seen that ground of front of tunnel face displaces like flow in the direction of the tunnel.

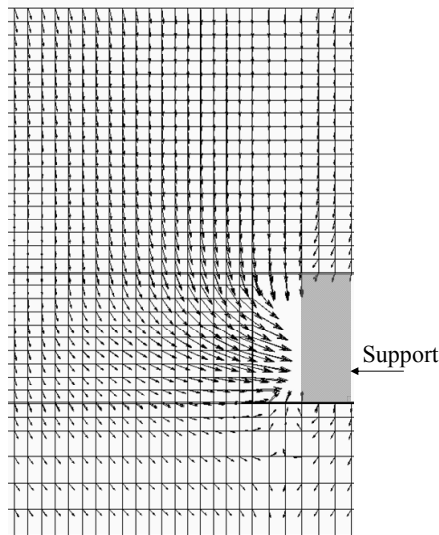


Fig.17 Displacement vector by analysis at 80G

5. Conclusion

In this study, to evaluate the applicability of strain softening-hardening model to problem of stability of tunnel face in unconsolidated ground with shear band extensions, Lade type elasto-plastic model that is added cohesion term is applied.

At first, unconfined compression tests and tri-axial compression tests with same composition specimen of centrifuge ground model are simulated by numerical model. And by fitting results to elemental tests, eight parameters are estimated. After that, centrifuge model tests are simulated. The results of these, the relation between lateral face displacement and centrifuge acceleration and relation between surface settlement and acceleration are estimated well. Also, location of crack developed in experimental model is well predicted as shear band by numerical model.

By using the method of evaluate the nonlinearity by modifying the stress, Lade type elasto-plastic model that predict the strain softening and hardening can be applied to problem of tunnel stability. It can be determined that it becomes an option in the case of tri-axial compression test data is available.

6. References

- 1) W. H. Hansmire, and E. J. Cording, *J. Geotech. Eng.*, **111**, 1301 (1985)
- 2) D. Steripi, and A. Cividini, *Rock Mech. Rock Eng.*, **37**, 277 (2004)
- 3) H. Ohtsu, Y. Hakoishi, M. Nago, and H. Taki, *Proceedings of the South East Asian Symposium on Tunneling and Underground Space Development*, 157-164 (1995)
- 4) S. Abdel-Baki, A. Ata and M. Hamza, *Proceedings of the North American Tunneling '96*, 11 (1996)
- 5) J. Lee, S. Akutagawa, T. Kitagawa, A. Isogai, and T. Matsunaga, *Proceeding of Tunnel Engineering*, **15**, 69 (2005)
- 6) S. Akutagawa, K. Matsumoto, and H. Nagai, *Proceeding of Tunnel Engineering*, **10**, 113 (2000) (in Japanese)
- 7) K. Nakaoka, K. Hata, S. Akutagawa, and S. Takahashi, *Proceeding of 2nd International Conference on Computational Methods in Tunneling*, **2**, 281 (2009)
- 8) S. Takahashi, S. Sugie, T. Kuwahara, and M. Toriihara, *Proceeding of the Japan National Conference on Geotechnical Engineering*, **40**, 1867 (2005) (in Japanese)
- 9) P. V. Lade, *Int. J. Solid Struct.*, **13**, 1019 (1977)
- 10) E. Mizuno, and S. Hatanaka, *J. Eng. Mech.-ASCE*, **118**, 1546 (1992)

Study on Evaluation of Fine Fraction Content of Soil Using Soil-Metal Friction Sound for Liquefaction Assessment by Swedish Ram Sounding

Suguru YAMADA* and Akihiko OSHIMA**

(Received October 2, 2015)

Synopsis

This article presents a possible idea for evaluating fine fraction content of subsurface soil through an operation of Swedish Ram Sounding (SRS) by employing acoustic properties of friction sound generating by friction occurs between surface of metallic penetration cone and surrounding soil. A series of soil-metal friction test was performed on silica sand with various fines content using a modified direct box shear apparatus to simulate a friction phenomenon between SRS cone and surrounding soil. As a result of experiments, it was found that the sound pressure level (SPL) of friction sound was depended on relative density as well as fines content of sandy specimen. Based on obtained testing results, an idea for evaluating fines content of ground by SRS was tentatively proposed.

KEYWORDS: Liquefaction, Dynamic cone penetration, Friction, Sound pressure level

1. Introduction

In response to liquefaction-caused severe damages in residential ground during the 2011 off the Pacific coast of Tohoku Earthquake, demands for applying measures against liquefaction to residential properties has been risen up in Japan. It is, however, not simple to assess the safeness against liquefaction in an individual residential property with applying conventional *FL* method, in which grain-size properties of particular stratum are required, because of the difficulty to take soil samples from ground by conventional field investigation techniques which have been employed in the small house constructions. Therefore, it is necessary to develop technologies, with reasonable cost, evaluating grain-size properties of soil for the residential ground, in order to achieve liquefaction assessment to residential properties.

In the present study, it was attempted evaluating fines content by employing the friction sound generating underground during the work of Swedish Ram Sounding (SRS). The SRS, a dynamic cone penetration test, has been recently becoming a major field investigation technique for residential property in Japan. As a part of process in SRS work, the torque is measured by rotating a penetration rod at every 0.2m in the penetration length to correct the effect of skin friction resistance on number of blow (N_{dm}). A stainless steel cone with a diameter of 45mm was made 2 turns at an angular velocity approximately 47deg/sec in the ground during torque measurement. Meanwhile, the generated friction sound by the friction of cone with soil was recorded. If this frictional behaviour is assumed as the shear occurs between stainless steel and soil, it can be thought that the recorded sound was generated when large shear deformation was developed between stainless steel and soil. Therefore in this study, a series of direct box shear test was performed on silica sand with various fines content using a direct box shear apparatus, simulating the friction behaviour between stainless steel and soil in the torque measurement. The friction sound was recorded during shear, then relations between sound pressure level (*SPL*) of friction sound and fines content as well as relative density of specimens were investigated.

2. Apparatus and Experimental Procedure

Direct box shear test

Direct box shear tests were performed using a standard type direct box shear apparatus (JGS 0560-2000)¹⁾. An upper shear box of the apparatus was switched to a plate of stainless steel (SUS304) in which a piezoelectric

* Lecturer, Department of Urban Engineering

** Professor, Department of Urban Engineering

microphone was installed. The friction sound generated by shearing between soils and stainless steel was recorded. A schematic of upper and lower box of direct shear apparatus used is shown in Figure 1. Soils used for the direct box shear tests were silica sands which were prepared so that their fines content (F_c) to be 0, 9.8, 19.6, 29.4, 49.0, 68.6 and 98.0% by mixing 2 kinds of commercially available silica sands were Silica No5 and Fine Silica, whose F_c are 2% and 98%, respectively. Both were produced at a factory in Gihu prefecture, Japan. Soil samples were given IDs as SM0, SM10, SM20, SM30, SM50, SM70 and SM100 in ascending order of fines content. The grain size distribution curves of all soil sample used in this investigation are shown in Figure 2.

Specimens of 10mm in height and 60mm in diameter were prepared by the tamping method with 3 different conditions in initial density which were loose, middle and dense conditions. Table 1 summarizes physical properties of soil samples and testing conditions in direct box shear tests. Contents shown in the table are fines content (F_c), maximum and minimum void ratio (e_{max} and e_{min}), relative densities before consolidation (D_{ri}) and after consolidation (D_{rc}), consolidation stress (σ_n) and the displacement rate in the direct shear. All the specimens were subjected to one dimensional consolidation pressure at $\sigma_n=50\text{kPa}$, after that shear load was applied to the upper box until shear displacement reached to 15mm at 10mm/min of the constant shear rate. The friction sound was recorded continuously while shearing. The shear force was applied by rotating a screw jack handle manually to reduce mechanical noise would be recorded together with friction sound as much as possible.

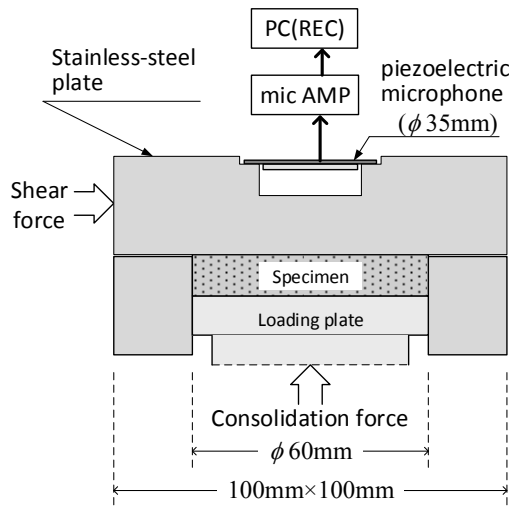


Fig. 1 Shear box used for direct box shear test.

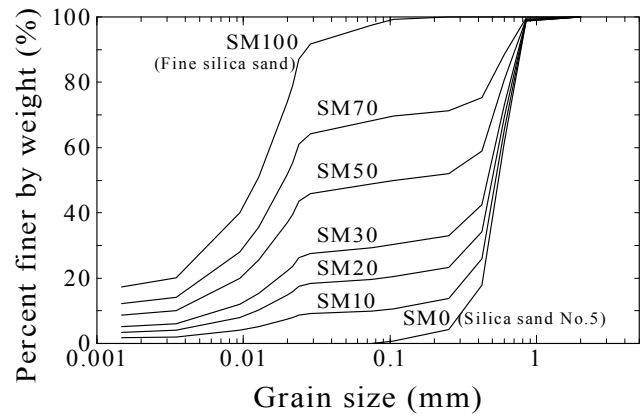


Fig. 2 Grain size distribution curves of silica sand mixture used in direct box shear tests.

Table 1. Physical properties of soil samples and experimental conditions in direct box shear tests.

Soil name	F_c (%)	e_{max}	e_{min}	Initial Density	D_{ri} (%)	D_{rc} (%)	σ_n (kPa)	Disp. rate (mm/min)
SM0 (Silica sand No.5)	0	0.63	1.00	Loose	10	38	50	10.0
				Middle	48	77		
				Dense	78	80		
SM10	9.8	0.49	0.92	Loose	-6	22		
				Dense	80	86		
SM20	19.6	0.40	0.88	Loose	-11	32		
				Dense	82	87		
SM30	29.4	0.40	0.95	Loose	-13	49		
				Middle	49	81		
SM50	49.0	0.46	1.16	Dense	81	88		
				Loose	-6	70		
SM70	68.6	0.62	1.42	Middle	52	74		
				Dense	81	85		
SM100	98.0	0.91	2.07	Loose	25	74		
				Dense	82	86		
				Dense	82	91		

Swedish Ram Sounding (SRS)

Swedish Ram Sounding (SRS) which is corresponding to a DPSH-A (Super Heavy-A) in the dynamic probing category according to ISO 22476-2(2005)²⁾, measures two parameters; the one is the number of blow (N_{dm}) per 0.2m in penetration length with dropping a hammer having the mass of 63.5kg from the height of 0.5m, the other is the torque (M_v) required to rotate the rod at every 0.2m of penetration length in N-m. The SRS N_d -value can be given by following equation, in which M_v is employed to correct the skin friction resistance from N_{dm} (Dahlgerg and Bergdahl, 1974³⁾ and Oshima, 2013⁴⁾). The SRS N_d -value can be considered nearly equal to the SPT N -value (N_{SPT}) because the equal potential energy of free-falling hammer per unit penetration length has been adopted in both tests.

$$N_{SPT} \approx N_{dm} - 0.04M_v \quad (1)$$

Figure 3 is a schematic of a condenser microphone embedded penetration cone used for recording friction sound by SRS. Note, the reason for employing the condenser microphone which is different kind from that used in the direct box shear test was to prevent the microphone from breaking or coming off during SRS work. A condenser microphone has higher structural strength than a piezoelectric microphone. The cone was screwed to the penetration rod, so that both could rotate together while the torque measurement. The torque was measured at every 0.2m of penetration depth by rotating penetration rod. The friction sound recording was continued while each 1m dynamic penetration would be completed.

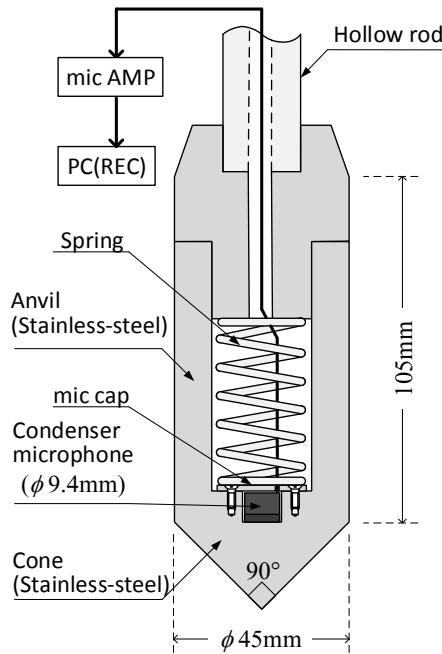


Fig. 3 Schematic of penetration cone used for SRS.

Measurement and Analysis of Friction Sound

The sound sensed by a microphone was amplified by a mic-amplifier then recorded at a sampling frequency of 44.1 kHz using PC software in both of direct box shear test and SRS. Employing a recorded sound by SRS performed at Urayasu city (Yamada and Oshima, 2015)⁵⁾ as an example, the procedure of analyzing the friction sound is described below.

Figure 4 shows a waveform of sound which was recorded continuously during 1 m dynamic penetration, the corresponding penetration depth was from 10.4m to 11.4m. The process of SRS work and the position of microphone, which is equal to depth of the cone, are indicated in the figure. Where, “blow” and “tor” indicate the rammer blow process and the torque measurement process, respectively. It is observed that amplitude of sound recorded in all blow process was over the range of recordable volume, and amplitude in every torque measurements process demonstrates almost constant values. Considering facts that the cone was stationary in the

ground and almost no signal was observed at the time from the end of “blow” to the start of “tor”, the sound recorded in the torque measurement process can be determined as the sound generated by friction between outer periphery of stainless steel cone and surrounded soil.

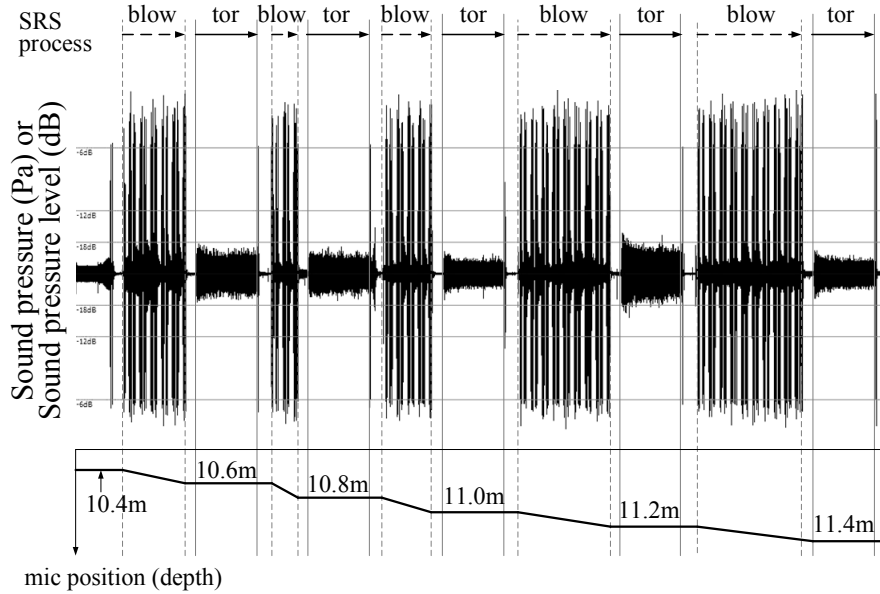


Fig. 4 Example of waveform recorded in SRS (Yamada and Oshima, 2015).

Figure 5 (a) shows a time history of sound pressure recorded at 10.6m in depth shown in Figure 4. The data shown in the figure is the signal of friction sound which was extracted from a raw data by applying the spectral subtraction (Boll, 1979)⁶⁾. The data of 2 seconds before the start of torque measurement, cone was stationary at this time, were applied as a noise sample to the denoising. Figure 5(b) shows the corresponding sound pressure level (*SPL*) to Figure 5(a). The *SPL* can be calculated by following equation as an expression in Decibel.

$$SPL = 10 \log_{10} \left(\frac{p^2}{p_0^2} \right) \quad (\text{in dB}) \quad (2)$$

Where, p is the sound pressure in Pa and p_0 is a referential sound pressure equal to $20\mu\text{Pa}$ which is known as minimum sound pressure human being can recognize.

Figure 5(c) shows a spectrogram calculated from the data shown in Figure 5(a) in the gray scale display in which the larger *SPL* is indicated by deeper black color. Where, the spectrogram is often-used expression in the acoustic phonetics which expresses a time series variation of the frequency spectrum indicating the intensity of frequency component by color gradations. It can be understood from Figures 5(b) and (c) that the friction sound recorded during the torque measurement is indicating stable *SPL* with approximately 65dB as well as showing the less variation in the frequency spectrum along time. In the present study, therefore, an average of *SPL* of entire data recorded in single torque measurement is defined as the mean *SPL*, representing an acoustic property of the friction sound.

3. Experimental Result

As an example of the field measurement by SRS, the results obtained at a site in Osaka city is shown in Figure 6. As for details of site profile etc., refer Mine et al. (2015)⁷⁾. The figure illustrates relations between mean *SPL* and F_c at same depth. The data of F_c were obtained from soil samples of SPT performed at same date. Symbols are indicating an individual soil classifications. A general trend can be observed that the mean *SPL* decreases with an increasing in F_c , the trend seems to be independent from the difference of soil type. This result may suggest that there is a correlation between the loudness of the friction sound and the grain-size characteristics.

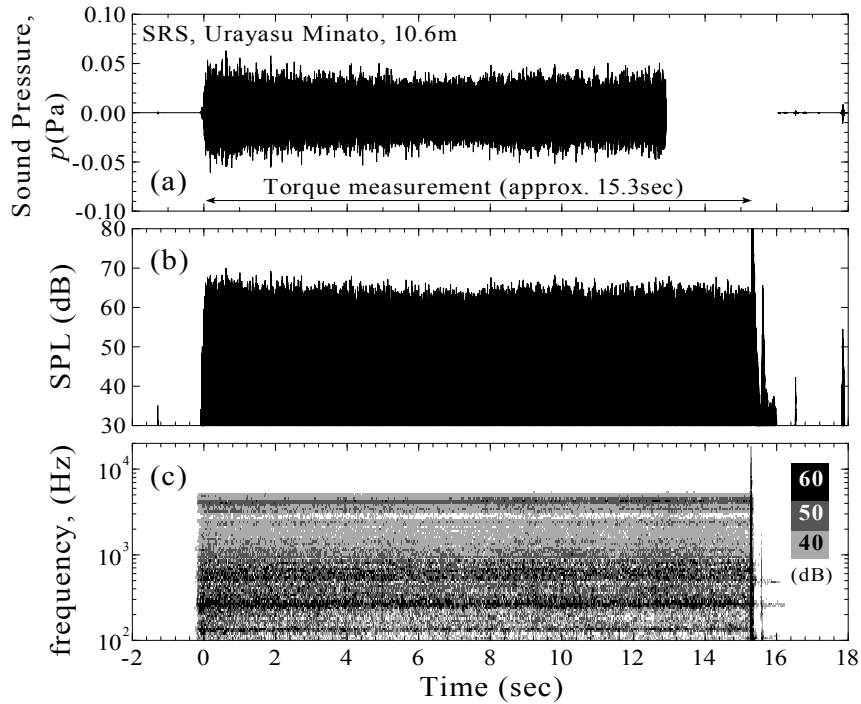


Fig. 5 Time histories: (a) sound pressure, (b) sound pressure level and (c) power spectrum.

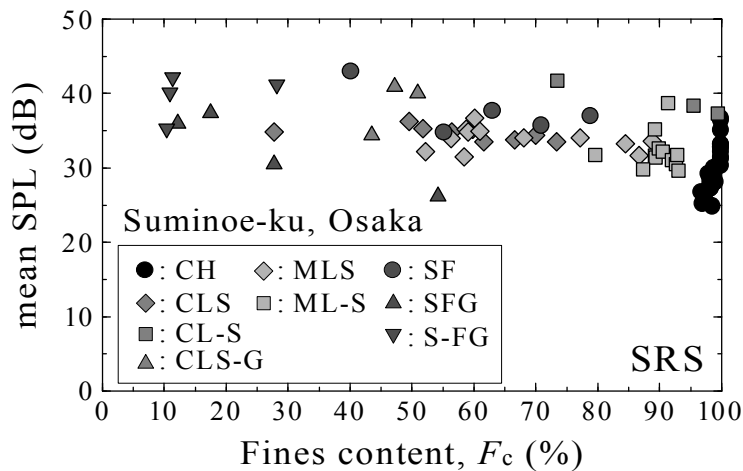


Fig. 6 Relation between SPL and fines content, result of field measurement by SRS.

Figure 7(a) and (b) show relations between shear stress and shear displacement as well as *SPL* and shear displacement obtained from direct box shear test on SM10 with loose density. In Figure 7(b), the Black colored indicates *SPL* recorded with 44.1 kHz in sampling frequency and the Yellow colored indicates data of their 4096 period (approximately 0.09 sec) moving average. The shear stress indicates almost constant value with small fluctuation after peak shear stress appeared at the beginning of the shearing. It can be observed in Figure 7(b) that *SPL* indicates larger value at the shear displacement less than approximately 1mm, and after that it indicates constant value in average showing large fluctuations in conjunction with the change of shear stress. Since almost constant value in both shear stress and *SPL* were obtained from all test conducted in the present study, the mean *SPL* which is a parameter represents an acoustic property of the friction sound was defined as an averaged *SPL* value obtained from 10 second's data between 35 and 45 sec, which is corresponding to the range of the shear displacement from 5.8 to 7.5mm.

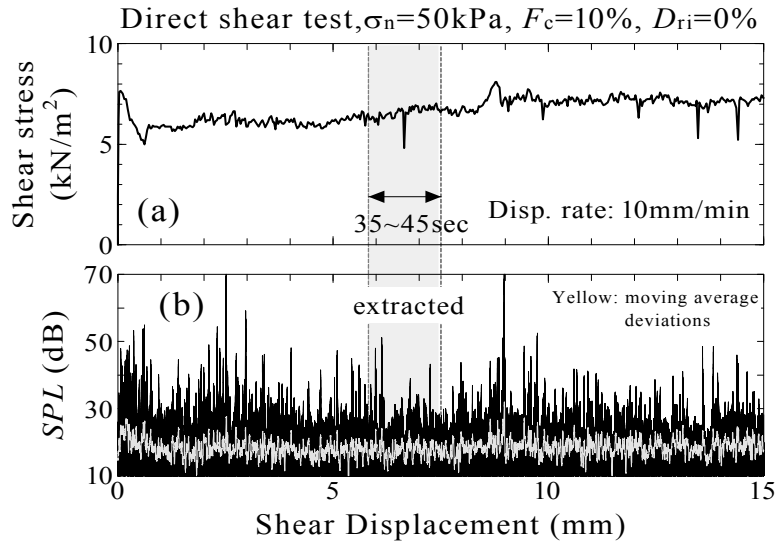


Fig. 7 Example result of direct box shear test: (a) Shear stress vs. shear disp.; (b) *SPL* vs. shear disp.

Figure 8 shows a relationship between mean *SPL* and F_c obtained from all direct box shear test performed. It should be mentioned that there is large difference in the mean *SPL* between SRS and direct box shear test. This difference can be considered to be due to that there were differences in the type of microphone, the shape of apparatus and the shear rate among the tests. However, a general trend can be observed that the mean *SPL* decreases with increasing in F_c except for the results of SM0 ($F_c=0\%$) specimens. This observed trend is agreed with that shown in Figure 6 which was obtained from the field measurement by SRS. A probable reason for the smaller mean *SPL*s were resulted on SM0 is that most of particles were hard to move during shear because SM0 has narrow grain size range i.e. there is a minor difference in grain size among adjoining particles. Same reason might be applicable to the result on SM100. Figure 9 illustrates relations of mean *SPL* and relative density after consolidation (D_{rc}). Lines indicated in the figure can be given by Equation 2 will be described later. It is evidence that mean *SPL*s of sandy soil with constant F_c are depended on D_{rc} and they decrease with an increases in D_{rc} . It can be considered that soil particles in specimens with high density should be difficult to move because the degree of confinement acting to soil particles to be greater when density of specimen is higher.

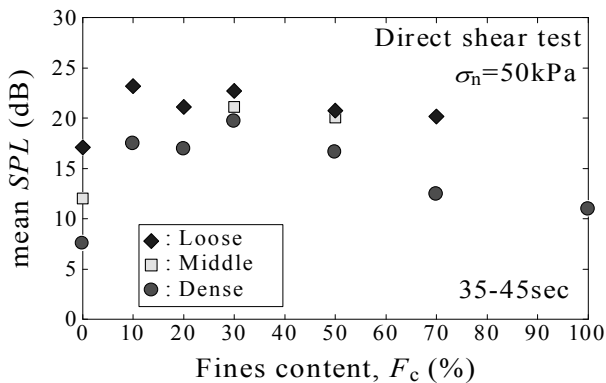


Fig. 8 Relation between mean *SPL* and fines content.

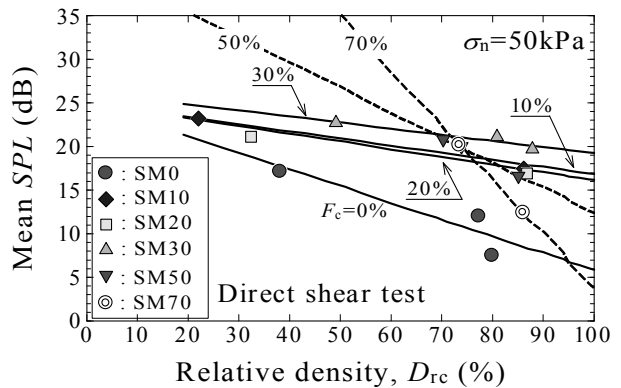


Fig. 9 Relation between mean *SPL* and relative density after consolidation.

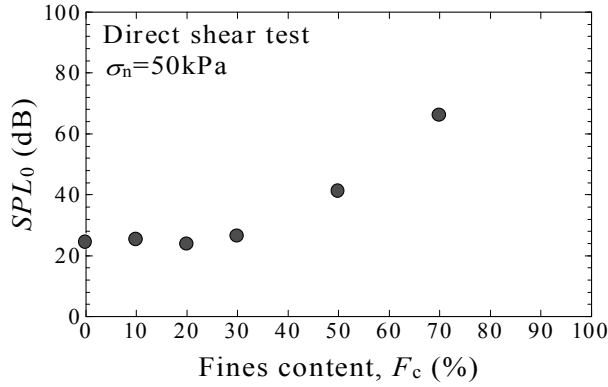


Fig. 10 Relationship between SPL for $D_{rc}=0\%$ and fines content.

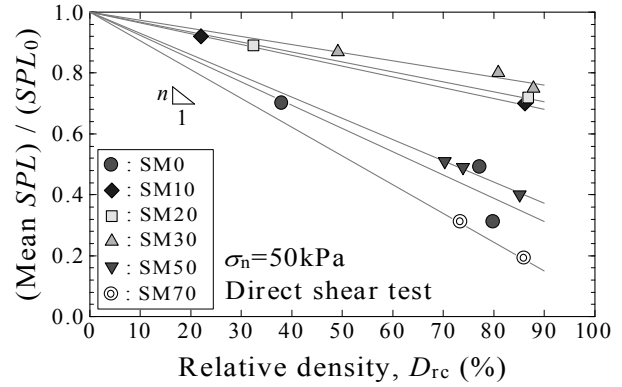


Fig. 11 Normalized mean SPL versus Relative density after consolidation.

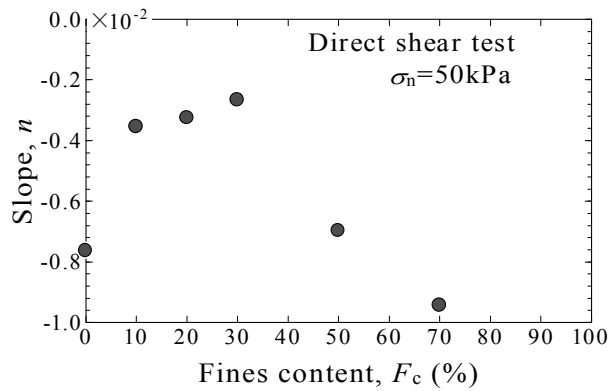


Fig. 12 Relation between relative density dependence factor n and fines content.

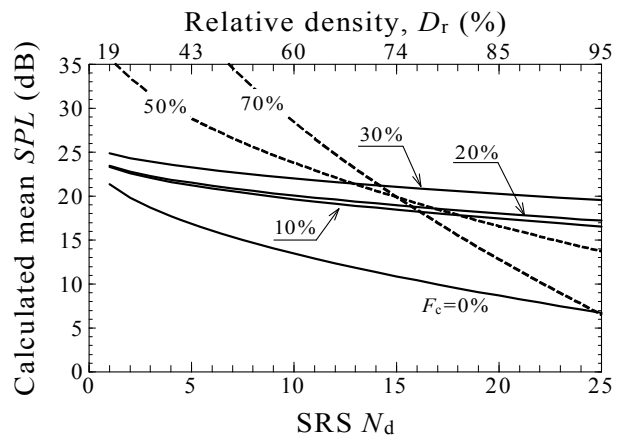


Fig. 13 Relation between Calculated mean SPL and $SRS N_d$ -value.

4. An idea for evaluating fine fraction content of soil by SRS

Based on experimental results discussed above, a tentative idea for evaluating F_c at site by SRS is described below. If relations between the mean SPL and D_{rc} shown in Figure 9 are able to be assumed to be linearly approximated on each F_c , the intercepts of approximated lines are equivalent to the mean SPL s at $D_{rc}=0\%$. By defining these intercepts as SPL_0 , a relation of SPL_0 and F_c is illustrated in Figure 10. The SPL_0 indicates almost same value in the range of F_c from 0 to 30%, and it increases linearly with increasing of F_c when F_c is greater than 30%. This trend may indicate that fine particles do not contribute to the magnitude of friction sound of very loose sandy soils in the range of F_c up to 30%. However, there is some doubt about the reliability on SPL_0 s of $F_c = 50$ and 70% because they were obtained from results of two experiments on specimens whose D_{rc} were greater than 70%. Additional experiments are needed to confirm the accuracy of this trend.

In order to define the available range of the mean SPL of friction sound of soils having various relative densities and F_c , the normalized mean SPL was determined by dividing measured mean SPL by SPL_0 . Hence, every relation between the mean SPL and D_{rc} can be approximated by a straight line passing through an intercept 1 as shown in Figure 11. The slopes of approximation lines taking negative value represent the magnitude of dependency on relative density in the mean SPL . By reading slopes (n) of each lines from Figure 11, a relationship between n and F_c was illustrated in Figure 12. The values of n are corresponded to the range of variation in the mean SPL shown in Figure 8.

Therefore, the mean SPL can be expressed in the linear expression given by Equation 3. The lines drawn for each F_c in Figure 9 were calculated by Equation 3.

$$\text{meanSPL} = nD_r + \text{SPL}_0 \quad (\text{in dB}) \quad (3)$$

According to the well-known expression of Meyerhof (1957)⁸⁾, the relative density (D_r) can be expressed in a function of SPT N -value (N_{SPT}) and the effective overburden stress σ_v' as below,

$$D_r = 21 \sqrt{\frac{N_{\text{SPT}}}{0.7 + \sigma_v'/98}} \quad (\text{in Percent}) \quad (4)$$

This equation has been employed for evaluating liquefaction resistance by insitu sounding (e.g. Ishihara, 1996⁹⁾). Additionally, the N_{SPT} in Equation 4 can be considered to be equal to SRS N_d -value when the torque $M_v=0$ is substituted in Equation 1, for a simple assumption. Hence, the mean SPL can be expressed in a function of SRS N_d -value by substituting Equation 4 in Equation 3. Then, relationships between calculated mean SPL and SRS N_d -value can be obtained as shown in Figure 13. Note that all the value shown in the figure were calculated with the effective overburden stress $\sigma_v'=50\text{kPa}$ which is equal to the normal stress applied to specimens in direct box shear tests. Although Figure 13 was derived from the direct box shear tests on limited number of silica sands contain non-plastic fines, it may be indicating a prospect that the fines content of particular stratum can be estimated by measuring the friction sound adding to the conventional measurement of N_{dm} and M_v in a single SRS work.

5. Conclusions

Direct box shear tests were performed on silica sands with various fines content, simulating the friction of stainless steel cone with surrounding soil occurring during the torque measurement in SRS. The results indicates that the mean SPL obtained from both SRS test and direct box shear tests are affected by the relative density as well as by fines content. An idea to determine the fines content from conventional SRS work was proposed. However, the idea is tentative and should not be applied in practice at this moment, because it was based on results of direct box shear tests performed under considerably limited conditions, not only carried out using different equipment from that used in the field measurement by SRS. In order to develop an evaluating method of fines content using Soil-Metal friction sound by SRS, it is necessary to accumulate more experimental data on various kinds of soil by further testing in which reasonable conditions in the field measurement should be considered.

6. References

- 1) Japanese Geotechnical Society, *Method for consolidated constant pressure direct box shear test on soils*. JGS 0561-2000 (2000)
- 2) International Organization for Standardization, *Geotechnical investigation and testing –Field testing- Part 2; Dynamic probing*. ISO 22476-2: 2005 (2005)
- 3) R. Dahlberg, and V. Bergdahl, *Investigations of the Swedish Ram Sounding method, Proc. European Symposium on Penetration Testing*, **2**, 93 (1974)
- 4) A. Oshima, *Geotechnical engineering magazine*, **61**, 40 (2013) (in Japanese)
- 5) S. Yamada, and A. Oshima, *Proc. of 15th ARC of SMGE* (2015) (in press)
- 6) S. F. Boll, *IEEE Transactions on Acoustics, Speech and Signal Processing*, **27**, 113 (1979)
- 7) S. Mine, et al. *Ground investigation at Suminoe-ku, Osaka (Part1: Sounding), Proc. of 50th annual conf. of JGS*, 169-170 (2015) (in Japanese)
- 8) G. G. Meyerhof, *Proc. 4th Int. Conf. on SMFE*, **1**, 110 (1957)
- 9) K. Ishihara, *OXFORD engineering science series*, **56**, 287 (1996)

Analysis of Resident Interest and Intentions for Community Bus Network Reorganization

Yumie SAWADA* and Takashi UCHIDA**

(Received October 2, 2015)

Synopsis

Continuous reorganization of a community bus network to maintain the service is extremely important. This study specifically examines residents, who must play an important role in the reorganization of a community bus network, in terms of their interests and intentions for reorganization of community bus network. The target case is Akashi community bus "Taco Bus." This bus is well known in the PDCA cycle.

The questionnaire results of the reveal usage conditions and socioeconomic characteristics in addition to the state of their interests and intentions. Based on the data of the questionnaire, the interests and intentions are classified into five groups by principal component analysis and cluster analysis. To clarify the group characteristics, discriminant analysis was conducted. We discuss the problems of maintaining a bus network based on the group characteristics.

KEYWORDS: Public transportation, Transportation poor, PDCA cycle, Questionnaire, Statistical analysis

1. Research Background and Objectives

(1) Research background

Recently, the Bus business has not been very rewarding. In rural areas, many bus services have been forced to stop. In urban areas, numerous problems such as heavy traffic and reorganization of bus networks and providing efficient services have decreased the number of passengers. Management rationalization of buses has been demanded in both areas. However, in the local government, the need exists for the maintenance of life transportation of residents to maintain and improve the welfare services of residents.

In Japan, aging has become a serious problem. Aging of the population in Japan is expected to proceed faster than in Western countries. In the future, people will increasingly give up driving because of aging. However, social participation of elderly people as workers is expected to increase. Their demand for mobility is expected to increase.

In February 2002, because of the revision of road transport laws, supply and demand adjustment regulations in omnibus businesses have been discontinued. Buses have attracted attention as a mode of public transport. The introduction of a "Community Bus" that maintains close contact with the community is expected to be useful for community development and activity.

Maintaining convenience and ongoing review and improvement for utilization is extremely important in the community bus management. It is conducted in many areas. Takebayashi¹⁾ et al. introduced many favorable comments from residents related to the method of service review in the PDCA cycle, including the operational review criteria.

(2) Research objectives

This study targets Akashi community bus "Taco Bus," which is carrying out reorganization of community bus network steadily²⁾. Because residents serve important roles in the reorganization, their interests and intentions for the reorganization become clear by doing the questionnaire survey. The following must be

*Students, Master Course of Department of Urban Engineering

** Professor, Department of Urban Engineering

clarified through analyses.

- 1) Understanding the state of resident interests and intentions
- 2) Grouping resident interests and intentions
- 3) Elucidating characteristics of the group

(3) Research approach

The flow of research is presented in Figure 1. First, material of Akashi City local public transport meeting understands outline about the Taco Bus such as methods of handling, the number of users, methods and achievements for reorganization and promotions to resident. Second, a questionnaire is administered to residents. The questionnaire is constructed around promotions to resident. By multivariate analysis of the questionnaire data, the interests and intention are classified into groups to reveal the impact factors.

2. Questionnaire

(1) Questionnaire objectives

It is necessary to understand how residents have knowledge and emphasize efforts of promotion of utilization and reorganization of the community bus network. The results can be used to clarify whether some willingness exists to cooperate in these efforts, in addition to the resident interests and intentions. These objectives guide the pursuit of basic knowledge for executing an ideal reorganization for a community bus network.

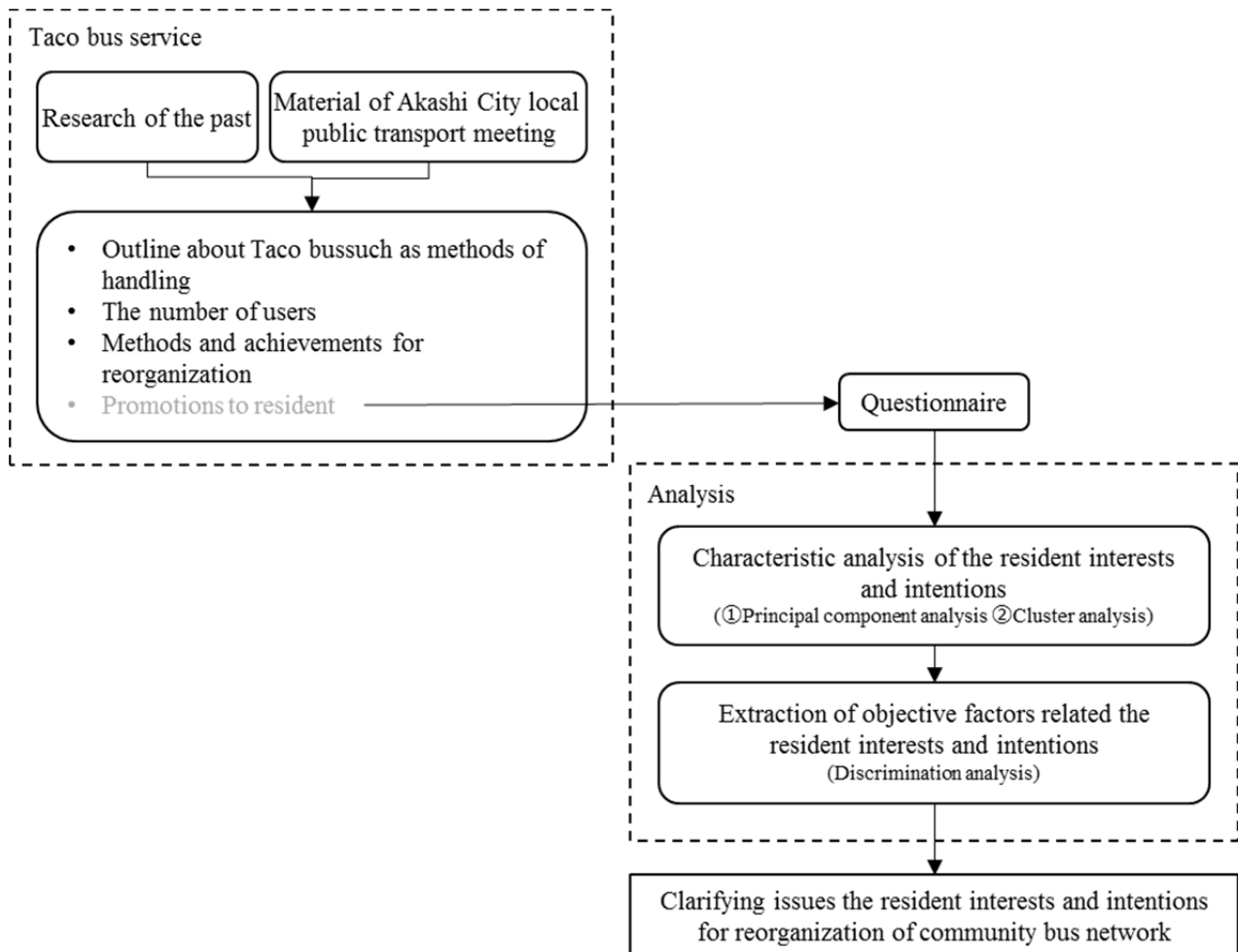


Fig. 1 Flow of research.

(2) Questionnaire outline

This study questionnaire survey is targeted at Akashi citizens with a specific examination of Taco Bus users. The survey dates are August 28, 2014 (Thursday), 30 (Saturday), 31 (Sunday), and September 4 (Thursday), 6 (Saturday), 7 (Sunday). The locations are JR Nishi Akashi Station, Okubo Station, Uozumi Station, and Sanyo Higashi Futami Station. At each location, the questionnaire survey is administered twice on holidays and once on weekdays. This survey was administered face-to-face or through distribution and recovery of questionnaires by post.

(3) Question contents

The questionnaire consists of seven questions (Table 2): [1] Knowledge of utilization promotion measures, [2] Number of use of utilization promotion measures, [3] Importance evaluation of utilization promotion measures, [4] Cooperation intention to maintain the operation, [5] Relation with Taco Bus on the daily life, [6] Respondent attributes, and [7] Free description.

Individual conditions for the Taco Bus are shown by “[1] Knowledge of utilization promotion measures”, “[2] Frequency of use of utilization promotion measures,” and “[5] Relation with Taco Bus on the daily life”. In addition, “[3] Importance evaluation of utilization promotion measures” and “[4] Cooperation intention to maintain the operation” are the resident interests and intentions. This study compares the individual conditions and the resident interests and intentions.

This study only uses postal recovery. Utilization promotion measures are (13) from (1) in [1], [2], and [3]. In “[4] Cooperation intention to maintain the operation,” (1)–(6) are concrete cooperation contents, (7)–(9) are negative choices for cooperation.

3. Characteristic analysis of resident interests and intentions

(1) Methods of analysis

This study groups the respondents for each characteristic of resident interests and intentions. First, do principal component analysis using the answers of “[3] Importance evaluation of utilization promotion measures” and “[4] Cooperation intention to maintain the operation.” Second, respondents are divided into groups by doing cluster analysis using principal component scores.

(2) Principal component analysis

This study does principal component analysis. The data to be handled are 22 items: (13) from (1) of “[3] Importance evaluation of utilization promotion measures” and (9) from (1) of “[4] Cooperation intention to maintain the operation” (Table 3). In fact, (7) and (8) are integrated.

The eigenvalue, contribution rate, and cumulative contribution rate of each principal component are shown in Table 4. The eigenvector of each principal component is shown in Table 5 and Figure 2. As a condition of determining the principal component number, the principal component is 1.0 or more of the eigenvalues. This analysis uses four principal components.

These components are characterized in Figure 2 by each eigenvector.

1st: The positive degree of evaluation for the current measures

All “Importance evaluation of utilization promotion measures” are positive values and “[4] (7) (8) Do not cooperate” are negative values.

2nd: Having intention of contribution including the specific use

“[4] (1) Discussion in familiar place about easier use”, “[4] (2) Joint purchase of book of tickets and free passes”, “[4] (3) Suggestion of using Taco Bus to surrounding residents” and “[4] (5) Cooperate if there are people who are working to support” were positive values.

3rd: (+) Emphasizing substantial cooperation for improvement vs. (-) Cooperation with using or existing efforts

“[4] (1) Discussion in familiar place about easier use” is a positive value. “[4] (3) suggestion of using Taco Bus to surrounding residents”, “[4] (4) Taking as many Taco Buses as possible” and “[4] (6) Taking advantage of existing efforts” are negative values.

4th: (+) No idea – although having intention to cooperate vs. (-) No intention to cooperate

“[4] (9) No idea” is a positive value. “[4] (7) (8) Do not cooperate” is a negative value.

Table 1 Questionnaire outline

Method	Face-to-face or the distribution and mailing recovery of questionnaires
Location	Nishi Akashi Station, Okubo Station, Uozumi Station (JR) Higashi Futami Station (Sanyo)
Subject	Passengers and passers-by (Taco bus users and Akashi citizen)
Date	Twice on holidays and once on weekdays at each place August 28, 2014 (Thursday), 30 (Saturday), 31 (Sunday) September 4 (Thursday), 6 (Saturday), 7 (Sunday).
Recovery number	Face-to-face: 182 Mailing recovery: 231(Rate 33.4%)

Table 2 Question contents

Content		Item
Utilization promotion measures	[1] Knowledge	(1) Taco bus Akashi eco family system (2) Book of tickets (3) Taco bus supporter (4) Taco bus cheer shop (5) Bingo and a stamp rally on Taco bus (6) Taco bus with Christmas decoration
	[2] Number of use	(7) Cooperation with the local community such as high school students and child care support organizations (8) Visitation of facilities along the way (9) Events surrounding Taco bus (10) Giving Akashi city bus trial ticket
	[3] Importance valuation	(11) Information transmission by Twitter and Facebook (12) Performance reporting in the "Akashi regional public transportation conference" (13) Regional briefings
[4] Cooperation intention to maintain the operation		(1) Discussion in familiar place about easier use (2) Joint purchase of book of tickets and free passes (3) Suggestion of using Taco bus to surrounding residents (4) Taking as many Taco buses as possible (5) Cooperate if there are people who are working to support (6) Taking advantage of existing efforts (7) Difficult to cooperate now (8) Do not cooperate (9) No idea (10) Other
[5] Relation with Taco Bus on the daily life		(1) Ride frequency of Taco bus (2) Bus utilization on the survey day (3) Taco bus stop on home nearest (4) Knowledge of the route map distribution location of Taco bus (5) How to get information about Taco bus (6) Thinking that there is a bus in life
[6] Respondent attributes		(1) Sex (2) Age (3) Who do live together (4) Postal code (5) Available move means (6) Usage of the bus other than Taco bus (7) Bus usage of housemate
[7] Free description		

Table 3 Data for principal component analysis

	Variable	Range of variables
[3] Importance evaluation of utilization promotion measures	(1) Taco bus Akashi eco family system (2) Book of tickets (3) Taco bus supporter (4) Taco bus cheer shop (5) Bingo and a stamp rally on Taco bus (6) Taco bus with Christmas decoration (7) Cooperation with the local community such as high school students and child care support organizations (8) Visitation of facilities along the way (9) Events surrounding Taco bus (10) Giving Akashi city bus trial ticket (11) Information transmission by Twitter and Facebook (12) Performance reporting in the "Akashi regional public transportation conference" (13) Regional briefings	1. Not really important 2. Not important 3. Neutral 4. Important 5. Very important
[4] Cooperation intention to maintain the operation	(1) Discussion in familiar place about easier use (2) Joint purchase of book of tickets and free passes (3) Suggestion of using Taco Bus to surrounding residents (4) Taking as many Taco buses as possible (5) Cooperate if there are people who are working to support (6) Taking advantage of existing efforts (7) (8) Do not cooperate (9) No idea	0. No 1. Yes

Table 4 Eigenvalue, contribution rate, and cumulative contribution rate of each principal component

NO	Eigenvalue	Contribution rate (%)	Cumulative contribution rate (%)
1	8.181	38.955	38.955
2	1.908	9.084	48.039
3	1.287	6.130	54.169
4	1.146	5.455	59.625

(3) Cluster analysis

This study classifies the respondents using the principal component scores obtained in (2), and does hierarchical cluster analysis by Ward Method. A summary of the treated cases is shown in Table 6. A dendrogram is shown in Figure 3. Results of cluster analysis show that they can be grouped into five at a position where coupling distance is 10. The five groups are named A, B, C, D, and E from the top.

(4) Group characteristics

This section explains characteristics of each group obtained by (3). Figure 4 shows the first principal component scores of the respondents to the X-axis and the fourth principal component scores to the Y-axis. Figure 5 shows the second principal component scores to the X-axis and the third principal component scores to the Y-axis.

Specifically with respect to Figure 4, on the X-axis, the higher the value is, the more positive a respondent is about the current measures. On the Y-axis, the higher the value is, it is no idea - although having intention to cooperate. There is a concrete cooperation intention around the origin. The lower the value is, the less intention a respondent has to cooperate. Therefore, the group on the lower left of Figure 4 is negative about maintaining bus operations. The group around the origin has awareness of the issues about maintaining the operation and concrete cooperation intentions. At the top of Figure 4, a respondent has no idea about cooperation. At the bottom of Figure 4, a respondent has awareness of issues related to maintaining the operation, but no cooperation intention.

Table 5 Eigenvector of each principal component

Variable		Eigenvector (E)			
		1	2	3	4
[3] Importance evaluation of utilization promotion measures	(1) Taco bus Akashi eco family system	.783	-.185	-.178	.097
	(2) Book of tickets	.739	-.225	-.276	.230
	(3) Taco bus supporter	.722	.034	.222	.074
	(4) Taco bus cheer shop	.786	-.093	.190	.008
	(5) Bingo and a stamp rally on Taco bus	.776	-.192	.018	.032
	(6) Taco bus with Christmas decoration	.655	.017	.077	-.084
	(7) Cooperation with the local community such as high school students and child care support organizations	.786	-.092	.106	.006
	(8) Visitation of facilities along the way	.828	-.108	.106	-.008
	(9) Events surrounding Taco bus	.814	-.223	.105	-.100
	(10) Giving Akashi city bus trial ticket	.768	-.132	.101	-.029
	(11) Information transmission by Twitter and Facebook	.702	.120	-.031	-.173
	(12) Performance reporting in the "Akashi regional public transportation conference"	.734	-.067	.011	-.157
	(13) Regional briefings	.776	.101	-.006	-.242
[4] Cooperation intention to maintain the operation	(1) Discussion in familiar place about easier use	.142	.653	.479	.253
	(2) Joint purchase of book of tickets and free passes	.276	.587	.212	.091
	(3) Suggestion of using Taco Bus to surrounding residents	.198	.423	-.401	.014
	(4) Taking as many Taco buses as possible	.325	.384	-.443	.061
	(5) Cooperate if there are people who are working to support	.240	.588	.221	-.066
	(6) Taking advantage of existing efforts	.347	.288	-.543	.089
	(7) (8) Do not cooperate	-.483	-.191	.199	-.493
	(9) No idea	-.106	-.312	.167	.784
	$(E = \sum E_i)$		$0.4 \leq E_i < 0.6$		$0.6 \leq E_i $

Specifically with respect to Figure 5, on the X-axis, higher values represent a contribution intention including the specific use. On the Y-axis, higher values signify substantial cooperation for improvement. Lower values indicate cooperation with existing efforts. Therefore, the group on the left of Figure 5 is reluctant to contribute. The group on the upper right is emphasizing importance of cooperation to the improvement. The group on the lower right is cooperative about using buses or existing efforts.

The characteristics of these figures give the name of each group.

A: Negative about maintaining bus operations

A is on the lower left of Figure 4 and near the origin of Figure 5.

B: Having concrete cooperation intentions and emphasizing the importance of cooperation for improvement

B dominates the area near the origin of Figure 4 and the upper right of Figure 5.

C: Having awareness of issues related to maintaining operations, but no ideas about cooperation

C is on the top of Figure 4 and on the left of Figure 5.

D: Having concrete cooperation intentions and cooperation related to using buses or existing efforts

D dominates the area near the origin of Figure 4 and the lower right of Figure 5.

E: Having awareness of issues related to maintaining the operations, but reluctant to make contributions

E is located at the bottom near the origin of Figure 4 and on the left of Figure 5.

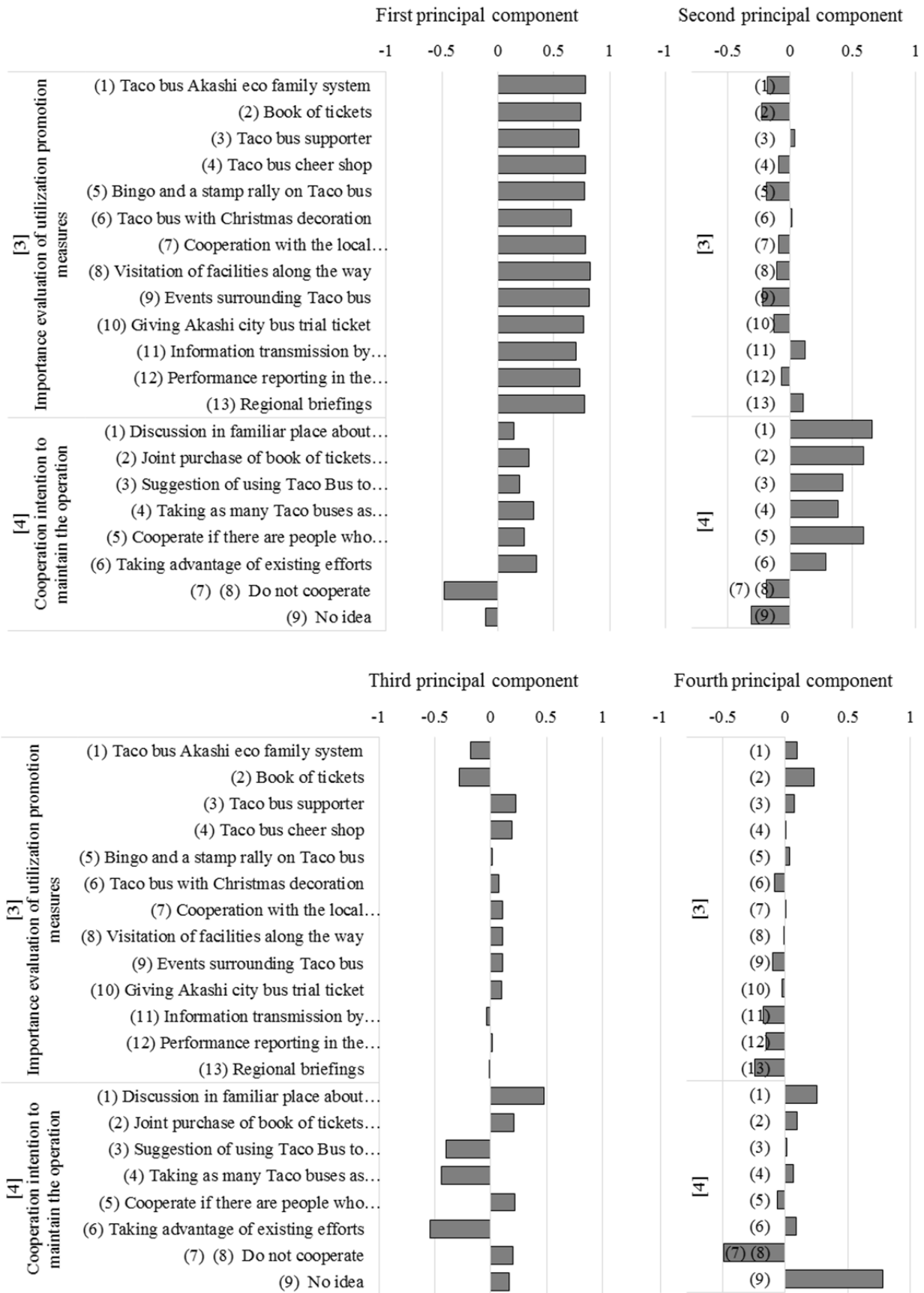


Fig. 2 Eigenvector of each principal component.

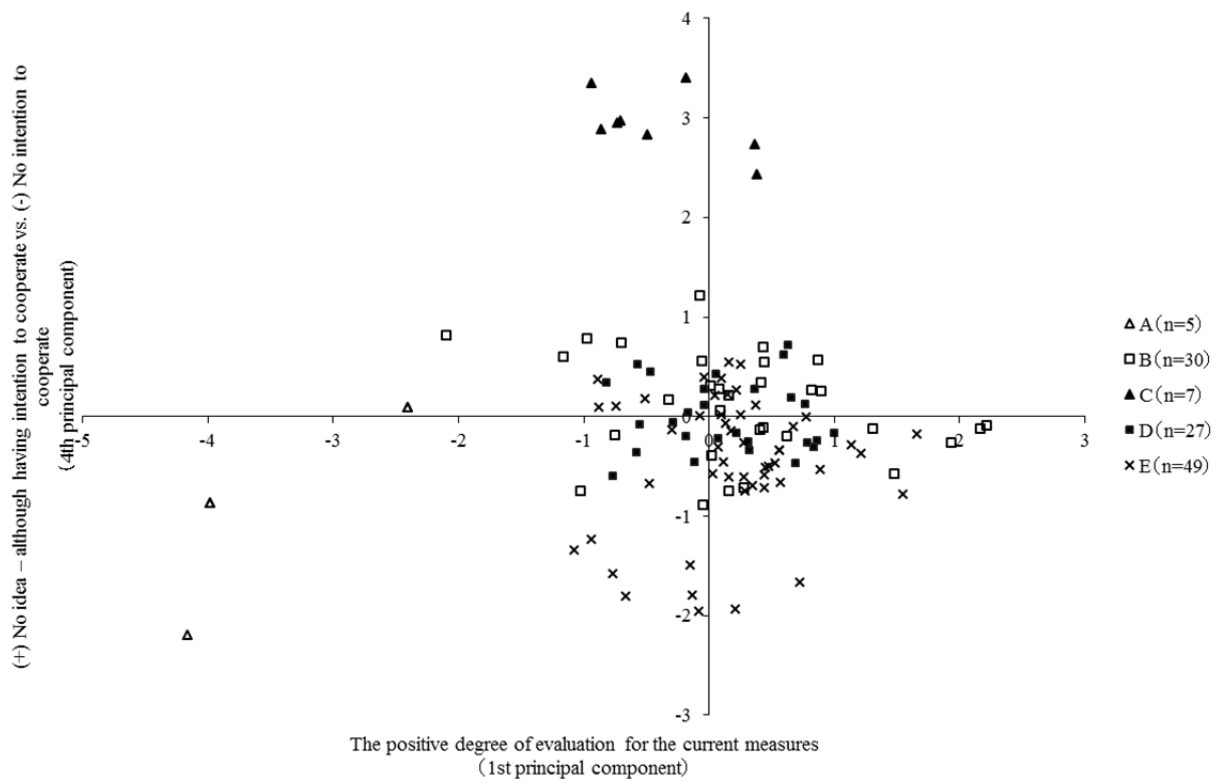


Fig. 4 First – Fourth principal component

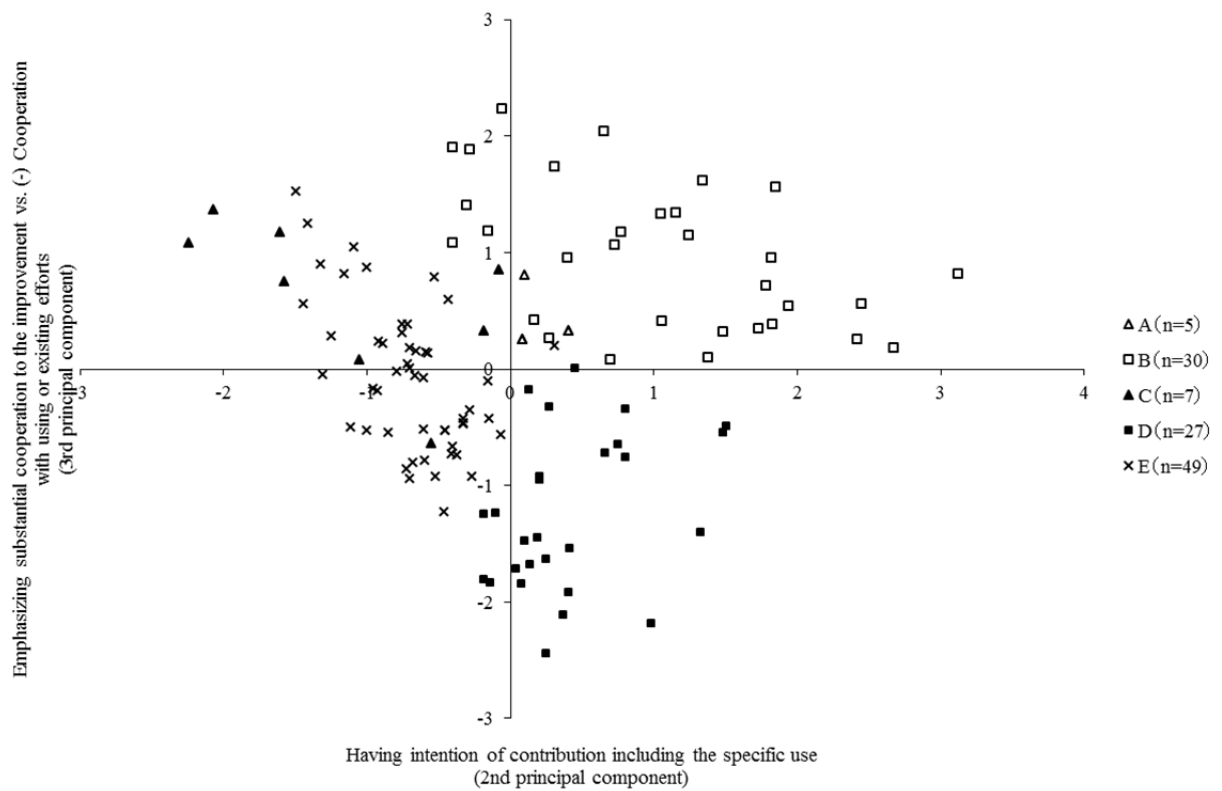


Fig. 5 Second – Third principal component

4. Extraction of objective factors related to resident interests and intentions

(1) Methods of analysis

This study does discriminant analysis to understand what kind of objective factors affect the group. The factors mean "[2] Number of uses of utilization promotion measures," "[5] Relation of Taco Bus to daily life," and "[6] Respondent attributes" among the questions. They are used as explanatory variables for this analysis.

(2) Discriminant analysis

Explained variables are the 5 groups obtained in 3. Explanatory variables are shown in Table 7. In all, there are 37 variables. These are considered that particularly affect the groups.

A summary of the treated analysis case is presented in Table 8. The eigenvalue, contribution rate, cumulative contribution rate and canonical correlation of each discrimination function are shown in Table 8. Standardized canonical discriminant function coefficients are shown in Table 9. Standardized canonical discriminant function coefficients are shown in Table 10. Table 11 and Figure 7 show the center of gravity of the group. It is obtained by canonical discriminant functions that are evaluated in the group average but not standardized. A summary of the classification is shown in Table 12. Table 13 presents classification results. The result shows that 51.7% of the original grouped cases are classified correctly.

From Table 13, B, D, and E show that the accuracy of the analysis is low. B is misjudged in C and E. D is misjudged in E and vice versa because B, C, D, and E show similar distributions at the 1st principal component (Figure 4). Especially, B, D, and E show similar distributions at the 4th principal component. D and some E are negative values at the 3rd principal component. Misclassifications reveal similar characteristics of each group. These are not related to the objective factors. Therefore, this misclassification presents no problems for these analyses.

To clarify the objective factors affecting the group, we next specifically examine standardized canonical discriminant function coefficients (Table 10). Regarding $0.4 \leq |a_i|$, one can describe the descending order of influence.

1st discriminant function:

It is common practice to use a book of tickets. There is no spouse among housemates. It is common to use Taco Bus with Christmas decorations. There are no bus users in the family.

2nd discriminant function:

The young user does not live with a sibling. The frequency of ticket book use is low. There is no bus user in the family.

3rd discriminant function:

There is no son or daughter among housemates. It is possible to drive a car. It is common to use a Taco Bus. Sex is female.

4th discriminant function:

There is a bus user in family. It is possible to drive a car and advanced age. The user live with a spouse.

Table 7 Explanatory variables for discriminant analysis

Variable		Range of variables
[2] Number of uses of utilization promotion measures	(1) Taco bus Akashi eco family system (2) Book of tickets (5) Bingo and a stamp rally on Taco bus (6) Taco bus with Christmas decoration	1. Never use 2. Use 3. Use well
[5] Relation with Taco Bus on the daily life	(1) Ride frequency of Taco bus	1. Almost everyday 2. A few days for a week 3. Once for a week 4. Once for a month 5. Usually not used, only when necessary use 6. Not use 7. Blank
	(3) Taco bus stop on home nearest	1. Don't know or Blank 2. Know or Nothing
[6] Respondent attributes	(1) Sex	1. Male 2. Female
	(2) Age	1. Under 10 years 2. The teens 3. Twenties 4. Thirties 5. Forties 6. Fifties 7. Sixties 8. Seventies 9. Eighties 10. 90 years or older.
	(3) Who do you live together	1) Parent 2) Son or daughter 3) Grandchild 4) Grandparents 5) Spouse 6) Sibling 7) Live alone 0. No 1. Yes
	(5) Available move means	1) Car 2) Motorbike 0. Can't 1. Can
	(6) Usage of the bus other than Taco bus	1. Use 2. Don't use
	(7) Bus usage of housemate	1. Yes 2. No

Table 8 Summary of the treated analysis case

		Number	%
Effective number		118	50.9
Exclusion	Not classified	93	40.1
	Missing one or more explanatory variables	4	1.7
	Not classified and missing one or more explanatory variables	17	7.3
	Total	114	49.1
Total		232	100.0

Table 9 Eigenvalue, contribution rate, cumulative contribution rate and canonical correlation of each discrimination function

Function	Eigenvalue	Contribution rate (%)	Cumulative contribution rate (%)	Canonical correlation
1	.494	43.8	43.8	.575
2	.289	25.6	69.4	.473
3	.223	19.8	89.2	.427
4	.122	10.8	100.0	.329

Table 10 Standardized canonical discriminant function coefficients

Variable		Function coefficients (a)			
		1	2	3	4
[2] Number of uses of utilization promotion measures	(1) Taco bus Akashi eco family system	.068	.039	.027	.266
	(2) Book of tickets	.818	-.408	.214	.217
	(5) Bingo and a stamp rally on Taco bus	-.001	.236	-.134	-.312
	(6) Taco bus with Christmas decoration	.344	.175	-.184	.332
[5] Relation with Taco Bus on the daily life	(1) Ride frequency of Taco bus	.473	.221	-.449	.254
	(3) Taco bus stop on home nearest	.108	.323	.210	.070
[6] Respondent attributes	(1) Sex	-.087	.151	.448	.216
	(2) Age	-.274	-.415	.069	.436
	1) Parent	-.227	.185	.270	-.054
	2) Son or daughter	.210	-.031	-.608	.096
	3) Grandchild	-.077	-.267	.311	.026
	(3) 4) Grandparents	-.151	.330	.074	-.173
	5) Spouse	-.603	.394	.030	.367
	6) Sibling	.124	.448	-.165	.251
	7) Live alone	.160	.370	.154	.226
	(5) 1) Car	-.205	-.206	.452	.497
	2) Motorbike	-.262	.147	.375	-.289
	(6) Usage of the bus other than Taco bus	-.020	.200	.151	-.259
	(7) Bus usage of housemate	.108	.404	.006	.574

$0.4 \leq |a_i|$

Table 11 Center of gravity of group

Group	Function			
	1	2	3	4
A	.150	-.889	-1.979	-.398
B	-.949	-.144	.231	-.286
C	-1.110	-.187	-.313	1.215
D	.755	-.662	.335	.078
E	.308	.571	-.079	-.001

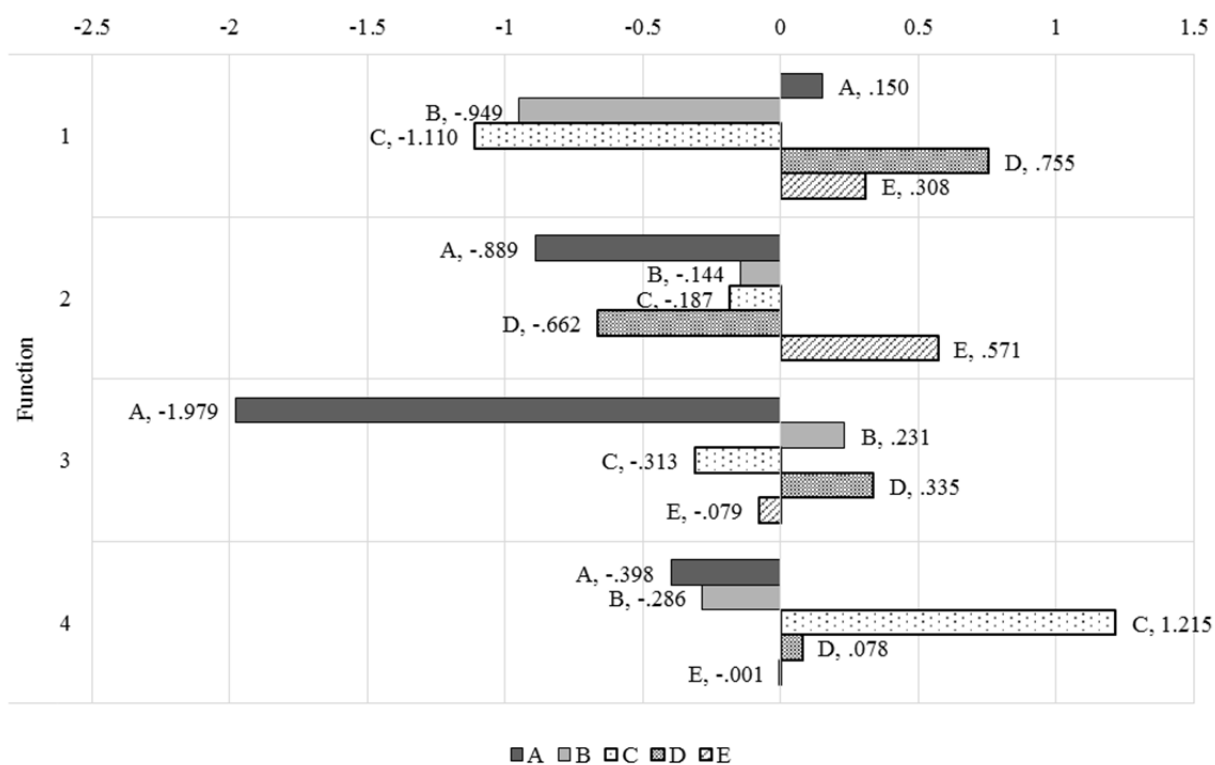


Fig. 6 Center of gravity of the group.

Table 12 Summary of the classification

Treated		232
Exclusion	Not classified	0
	Missing one or more explanatory variables	21
Used for classification		211

Table 13 Classification result

			Prediction data					Total
			A	B	C	D	E	
Original data	Number	A	4	0	0	0	1	5
		B	1	14	8	1	6	30
		C	0	1	5	0	1	7
		D	4	2	3	13	5	27
		E	4	5	6	9	25	49
	Cases that are not grouped		8	28	22	25	10	93
%	A	80.0	0.0	0.0	0.0	20.0	100.0	
	B	3.3	46.7	26.7	3.3	20.0	100.0	
	C	0.0	14.3	71.4	0.0	14.3	100.0	
	D	14.8	7.4	11.1	48.1	18.5	100.0	
	E	8.2	10.2	12.2	18.4	51.0	100.0	
Cases that are not grouped		8.6	30.1	23.7	26.9	10.8	100.0	

5. Conclusion

This study provided the following results.

- 1) Resident interests and intentions for the reorganization were divisible into five groups. These five groups are described below:
 - A: Negative about maintaining bus operations
 - B: Having concrete cooperation intentions and emphasizing the importance of cooperation for improvement
 - C: Having awareness of issues related to maintaining operations, but no ideas about cooperation
 - D: Having concrete cooperation intentions and cooperation related to using buses or existing efforts
 - E: Having awareness of issues related to maintaining the operations, but reluctant to make contributions
- 2) Because there is awareness of issues related to maintaining operations in the group other than A, most residents have the idea that it is necessary to maintain the bus network.
- 3) Results of discriminant analysis show that differences in cooperation methods and thoughts about the bus are affected by the presence of housemates, age, sex, manner of using the Taco Bus and the ability to drive a car.

Studies of the near future must provide cooperation methods commensurate with the characteristics, such as age or home environment. For example, C, “Having awareness of issues related to maintaining operations, but no ideas about cooperation,” presents a concrete cooperation method; E, “Having awareness of issues related to maintaining the operations, but reluctant to make contributions,” presents an indirect cooperation method.

6. References

- 1) H. Takebayashi, and Y. Nitta, *Jpn. Assoc. Inclusive Soc.*, **10**, 29 (2008) (in Japanese)
- 2) Y. Kurashima, and T. Uchida, *Proc. Infrastructure Planning*, **48**, 1-4 (2013) (in Japanese, CD-ROM)

Major Issues of Bicycle Use in Urban Area from View Point of Community Development

Yurie ISHINURA^{*}, Yasuo HINO^{**} and Yuuka WATANABE^{***}

(Received October 5, 2015)

Synopsis

The problems of illegally parked bicycles have been shifting in a central area from around rail station. In order to improve such problem, the activities based on public involvement must be necessary, because there are not only many small stores without parking facilities of bicycles, but also many stakeholders such as habitants and the store owners and the visitors, who have different interests. However, it is not always revealed the differences of interests for using bicycles among them. Then the aims of this study must be to investigate the consciousness of each stakeholder in the commercial area in Osaka city. As a result, it became clear that the illegal parked bicycles must be the common problem among of them, nevertheless the thinking of community development may be different. These interesting findings should be important information to realize the activity based on the public involvement.

KEYWORDS: Illegally parked bicycle, Community development, Commercial area, Public involvement, Questionnaire survey

1. Introduction

The problems of illegally parked bicycles have been shifting in a central area from around rail station according to improving the bicycle parking facilities¹⁾. Therefore, in the local government, although the regulations about the supplying parking facilities with the building was enforced in 2010, it is hard to expect the immediate effect. Therefore some urgent solutions must be required. On the other hand, there is the way of thinking to use the convenience of the bicycle in the commercial area for community development. However, there are various stakeholders such as habitants and the store owners and the visitors, who have different interests.

Therefore in order to improve such problem, the activities involved such stakeholders to realize the desirable community development must be necessary²⁾.

Then the aims of this study must be to investigate the consciousness of each stakeholder in Horie area of Nishi-ku district as a commercial area in Osaka city, in order to improve the common problems concerned with illegal parked bicycles. By using the questionnaire survey to the inhabitants, shop owners and/or managers and visitors, it may be expected to know the consciousness about “the desirable image of community development”, “the achievement of its community development”, “major issues of community development”, and “the way of bicycle use”. These findings must be expected to be not only the important information but also realize the activities based on the public involvement

2. Outline of Target Area

Horie area located in city center of Osaka city is divided into three zones as the residential zone (North-horie(1) and South-horie(1)), the mixture zone (North-horie(2) and South-horie(2)) and the commercial zone (North-horie(3) and South-horie(3)) by the pattern of major land use, as shown in Figure 1.

There are many illegal parked bicycles in all zones. But it must be clear that illegally parked bicycle number has increased especially in the commercial zone, as shown in Figure 2.

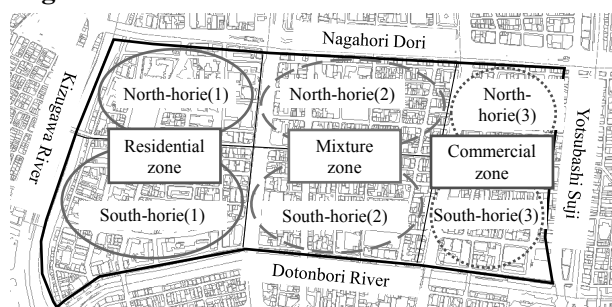


Fig. 1 Outline of target area
(Horie area of Nishi-ku district, Osaka city)

* Student, Master Course of Dept. of Urban Engineering, Osaka City University

** Professor, Dept. of Urban Engineering, Osaka City University

*** Engineer, Yachiyo Engineering Co., Ltd

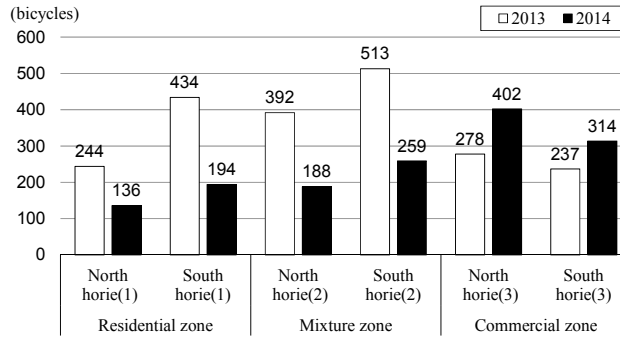


Fig. 2 Change of number of illegally parked bicycles by each zone

3. Outline of survey

In order to investigate the differences of consciousness for community development and thinking way of bicycle use by each stakeholder, the questionnaire survey was conducted for residents and store managers in North and South horie(3) as the commercial zone and South-horie(2) as the mixture zone. The number of distribution of questionnaire sheets and respondents were shown in Table 1.

The major questionnaire items are individual and household (only residents) attributes, conditions of possession and use of bicycles, parking facility, town development (ideal town and degree of achievement of ideal) and measures for parking problems as shown in Table 2.

Table 1 Number of distribution of questionnaire sheets and respondents

	resident	store manager
The number of the distribution	630 households	111 stores
The number of respondents	60 house holds (82 persons)	41 stores
The response rate	10%	37%

Table 2 Major questionnaire items for each stakeholder

Resident			Store manager		
Survey method			Survey method		
Distribution method	• Delivering to each house with cooperation of the neighborhood association		Distribution method	• Hearing to managers with cooperation of the neighborhood and store manager • Direct distribution to stores	
Collection method	• Postal service		Recovery method	• Postal service • Direct collection	
Main study subject			Main study subject		
Question items for Household	Household attribute	(1)Sex (2)Age (3)Residence career (4)Family composition (5)Zip code	Personal attribute	(1)Sex (2)Age (3)Store name (4)Industry type (5)Zip code (6)Employee number (7)Visitor number	
	The bicycle use storage space	(1)Number of own Bicycles (2)Preparation of parking space (3)Place of the parking		(1)Permission of the bicycle use of the employee (2)Number of employee' bicycles (3)Having bicycle parking or not in the store (4)Responsible person for cost of bicycle parking facilities (5)Degree of preparation bicycle parking facilities	
Question items for Individuals	Personal attribute	(1)Sex (2)Age (3)Occupation	The bicycle use storage space	(1)Future vision of town/Development criterion (2)Present conditions of the town (3)Problems of the town (4)Point at issue of illegally parked bicycles (5)Need of the bicycle use (6)Reason of the need of the bicycle use	
		Town development		(1)Future vision of town/Development criterion (2)Present conditions of the town (3)Problems of the town (4)Point at issue of illegally parked bicycles (5)Need of the bicycle use (6)Reason of the need of the bicycle use	
				Measures for Parking problems	(1)Need of measures for illegally parked bicycles (2)Responsible persons/organizations (3)Cooperation intention to an activity (4)Measures of for illegal parked bicycles (5)Method of preparing bicycle parking facilities
	(5-1)Cooperative intention to prepare parking facilities				
	(5-2)Cooperative intention to on-road parking facilities				
	(5-1)Cooperative intention to prepare parking facilities (5-2)Cooperative intention to on-road parking facilities				

This survey aims to clarify the differences of the direction of town development, the thinking of bicycle and problems of community development. These results may be useful to realize the work shop to deepen mutual understandings, and follow the actual activities to improve the bicycle problems based on the public involvement.

4. Way of thinking for community development and the bicycle use

The conditions of the ideal town for residents must be "safety and security" and "environment for residence", while "activity" and "prosperous business condition" must be important to store managers, as shown in Figure 3. Furthermore, it was clear that both of stakeholders evaluated their ideals were not enough to achieve, as shown in Figure 4. The common one of reasons of insufficient evaluation must be existence of illegal parked bicycles as shown in Figure 5.

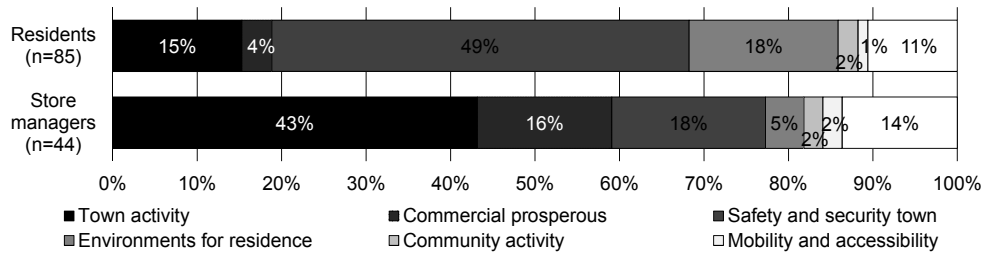


Fig. 3 Conditions of ideal town

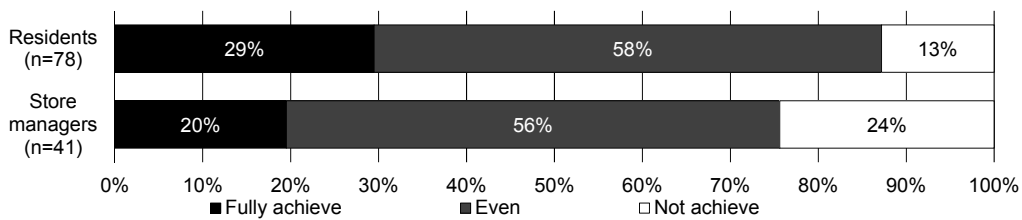


Fig. 4 Evaluation of achievement of ideal town

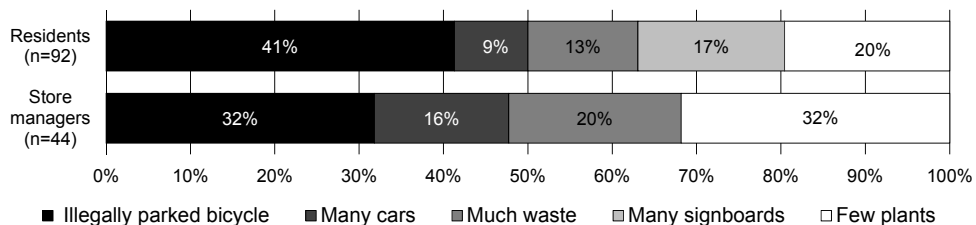


Fig. 5 Major problems of town

On the other hand, the evaluation of bicycle use are different of them, nevertheless they recognize the convenience of bicycle as shown in Figure 6. That is, store managers evaluate the convenience for visitors, while residents evaluate the convenience for their shopping.

Anyway, the illegal parked bicycles must be common problems. Therefore, it should be important to improve the problem with keeping the convenience for each stakeholder.

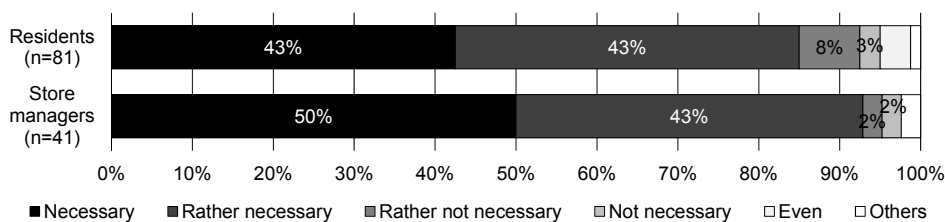


Fig. 6 Necessity of bicycle use

5. Measures for illegal parking of bicycles based on cooperation of stakeholders

Both residents and store managers recognize the necessity of measures against illegal parked bicycles, nevertheless they evaluate the convenience of bicycle use. Therefore, it must be essential to cooperate to improve the problem. As for this issue, both residents and store managers respond the necessity of all stakeholders, while they require the governmental measures as shown in Figure 7. This result may mean the possibility of activities based on public involvement. Especially, it may be possible to realize the cooperation concerned with sharing cost and/or offering space as shown in Figure 8. As an example of measure with cooperation of them, almost respondents show the cooperation consciousness of road use for bicycle parking, as shown in Figure 9. This result may show the possibility of not only introducing the temporary measure but also realizing the public involved activity in near future.

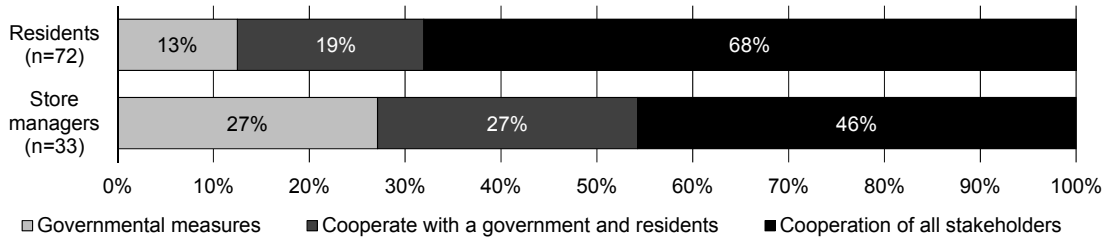


Fig. 7 Responsibility of measures against illegal parked bicycles

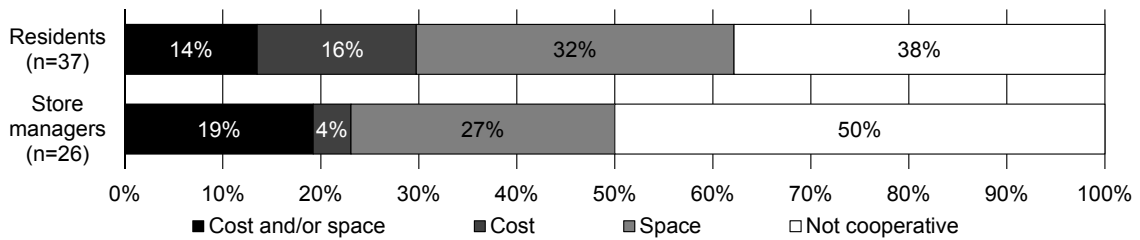


Fig. 8 Methods of cooperation against illegal parked bicycles

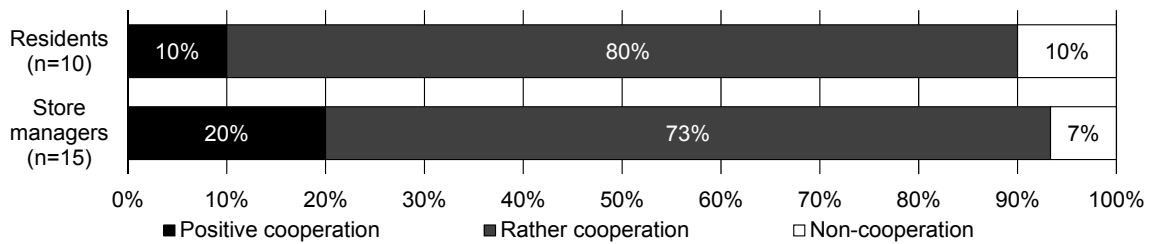


Fig. 9 Cooperation consciousness of road use for bicycle parking

6. Conclusion and next step

In this paper, some important findings concerned with illegal parked bicycles as a common problem for residents and store managers as different stakeholders in community development. These findings may be important information to not only introduce the temporary measure against illegal parked bicycles but also realize the continuous activities for community development based on public involvement.

Therefore, as the next step, it may be expected to hold the workshop with residents, store managers, visitors, local government and university members, in order to improve the bicycle problem and town development.

7. Acknowledgement

This study was implemented under the support of Nishi-ku local government, Osaka city. We would like to thank members of staffs of local government, members of the work shop in Takakiya district and all respondents to the questionnaire surveys.

8. References

- 1) Construction Bureau of Osaka City, *Fundamental Plan for Improving the Environments of Bicycle Use* (2011) (in Japanese)
- 2) Y. Ishimura, Y. Hino, X. Yamashiro, and T. Uchida, *Proc. Ann. Conf. JSCE Kansai Chapter*, IV-57 (2014) (in Japanese)

Abstracts of Papers

Published in Other Journals

Mechanical Engineering

Residual Bubble Volume Formed behind a Sphere Plunging into Liquid Bath

Kenji KATOH, Ryosuke MINAMI, Tatsuro WAKIMOTO, Yoshiaki UEDA (Setsunan Univ.) and Manabu IGUCHI (Osaka Electro-Communication Univ.)

Japanese Journal of Multiphase Flow, Vol. 28, pp. 547-553 (2015) (in Japanese)

An air cavity is formed behind a spherical particle plunging into a liquid bath. The residual bubble attached to the sphere has an important effect on the performance of CaO particle used for desulfurization of melted iron. Based on the water model with the same kinematic viscosity as the melted iron, the behavior of air cavity was observed for the spheres coated by two kinds of water repellent preparations. In this report, the volume of residual bubble was theoretically estimated for the quasi-static immersion of sphere as a reference condition. First the critical depth at which the axi-symmetric meniscus breaks is obtained by using Laplace equation. Then the bubble volume was obtained from a simple energy minimum principle in which we considered the effect of the interfacial energy including the wetting behavior and the liquid potential energy. The calculated volumes can approximate fairly well the measured results for two kinds of contact angles of 115° and 162° .

Development of a Wave Power Generation System Using a Slit Type Break Water (Water Wheel and Bending Plate Type Generators)

Kenji KATOH, Tatsuro WAKIMOTO, Takaaki SHIGEMATSU and Shin'ya YOSHIOKA

Proc. Int. Conf. on Jets, Wakes and Separated Flows 2015, Stockholm June 16-18, No. 2148169 (6 pages, USB memory) (2015)

A mini wave power generation system was proposed to be installed in a vertical slit type breakwater. The merits of the system are listed as follows. (i) no occupation of sea surface, (ii) maintenance facility, and (iii) high energy efficiency by using accelerated flow from the slit of breakwater. In this study, a new type of generator is proposed to perform higher efficiency. An elastic rectangular plate connected to a wheel and axle via a wire is set in the water chamber. When the wave drag bends the plate, a tension appears in the wire and the wheel connected to a generator is rotated. In order to estimate the power of the proposed systems in the real scale, the wave energy flowing into the breakwater was simulated numerically. More than 60% wave energy is collected in the water chamber behind the slit with 1/6 opening ratio. Although the output of the bending plate is rather small, the power per unit occupied sea area is superior to that of other types in literatures.

Experimental Observation and Numerical Simulation of Dynamic Wetting Behavior of Triple-Phase Contact line Passing over a Wall Defect

Kenji KATOH, Tatsuro WAKIMOTO, Shuhei HIGASHIDA, Yasufumi YAMAMOTO (Kansai Univ.) and Takahiro ITO (Nagoya Univ.)

Proc. ASME-JSME-KSME Joint Fluids Engineering Conf. 2015, Soul July 26-31, No. 19427 (2 pages, USB memory) (2015)

The effect of wall defects (impurities) on the dynamic wetting behavior was investigated experimentally and numerically. In the experiment, a silicon plate coated by SAMs (Self-Assembled Monolayers) was used as a test plate and a circular defect (diameter $300\mu\text{m}$) was made artificially by using a Ga beam to strip the SAMs film locally. The test plate was drawn up from the bath of test liquid with a constant speed (Capillary number $Ca=0.02\sim 0.1$) and the dynamic wetting behavior of triple-phase contact line was observed. The local contact angle on the centerline of the circular defect was measured precisely by using the deflection of a laser beam from the liquid surface. The same problem was simulated numerically with the GNBC (Generalized Navier Boundary Condition) to represent the slip motion of contact line on the wall. The stick slip motion of contact line observed experimentally was reproduced in the numerical results. The local contact angle and slip velocity of contact line qualitatively agree between numerical and experimental results. The work necessary to deform the liquid surface increases and approaches a limit at higher Ca number. This tendency should be responsible to determine Ca dependence of the macroscopic contact angle.

Development of Wave Power Generation System using a Slit Type Breakwater: Optimization of Waterwheel and Scaling Law

Tatsuro WAKIMOTO, Kenji KATOH, Takaaki SHIGEMATSU and Shin'ya YOSHIOKA

J. of JSEM, Vol. 15, pp. 26-30 (2015)

We developed a new wave power generation system installed in a slit type breakwater. This system has great advantages of no requirement of sea surface affecting on shipping route or fishing ground. In this system, accelerated flow from the slit of the breakwater drives waterwheels. In this study, the output power of the waterwheels was measured using a 1/12 reduced scale model to examine the optimal condition of type, diameter and mounting configuration of the waterwheels. Scaling law for estimating real scale output power from the reduced scale experiment was also examined by numerical simulation. A single mounted crossflow waterwheel achieved the maximum output power when its diameter is 1.5 times the width of the slit. Output power was predicted to be proportional to 3.5th power of scale and the square of wave height.

Measurement of Dynamic Surface Tension for Liquid Metal by Capillary Jet Method

Tatsuro WAKIMOTO and Kenji KATOH

Proc. Int. Conf. on Jets, Wakes and Separated Flows 2015, Stockholm June 16-18, No. 2147116 (6 pages, USB memory) (2015)

Most liquid metal is oxidized easily and its surface tension is decreased for a certain time. In this study, a novel measurement method for the temporal variation of surface tension, i.e. dynamic surface tension, is proposed. This method is based on the phenomenon that a downward trajectory of a capillary jet ejected horizontally from a small orifice with slow speed depends on not only inertia force and gravity force but also surface tension, which varies downstream by the oxidization. We derived a theory model to predict the jet trajectory and determined dynamic surface tension of the liquid metal from the theoretical trajectory which gives the most excellent approximation of an experimentally measured trajectory. Actual measurement for Wood's alloy in various oxygen concentrations demonstrates very fast surface tension variation of the order of 10 ms and proved the effectiveness of this method.

Experimental Analysis of Stabilization Mechanism of a Liquid Sheet Formed with Aqueous Surfactant Solution (Influence of Molecular Adsorption Density)

Tatsuro WAKIMOTO and Kenji KATOH

Proc. 13th Int. Conf. on Liquid Atomization and Spray Systems, Tainan August 23-27, No. D3-1-023 (5 pages, USB memory) (2015)

Surfactant is commonly added to ink or paint as dispersive agents for pigment or dye. The surfactant also interferes with the atomization of the liquid sheet injected from a spray nozzle since it has stabilizing effect on liquid surface, as soap film. However, the stabilization mechanism of liquid sheets formed with surfactant solutions is not fully understood. To investigate the stabilization mechanism, slight force was applied to the liquid sheet non-invasively, and time variable sheet thickness was measured optically until the rupture of the liquid sheet. The slight force was created using thermo-capillary effect. When the soap film is heated locally with a laser, spatial temperature distribution induces Marangoni force. The Marangoni force pulls the heated spot out-ward and causes the rupture. We estimated Marangoni force from absorbed heat in the liquid sheet and demonstrated the relation between the time required for the rupture and Marangoni force using aqueous solutions of 1, 10 and 25ppm of a typical anionic surfactant, dodecyl sodium sulfate (SDS). Brittle fracture of the soap film is observed by the measurement of sheet thickness. Sheet thickness decreases gradually to about 0.7 μm from the initial value of 1 μm , and then suddenly ruptured in spite of continuous increase of Marangoni force. We also estimated molecular adsorption density of the surfactant at each concentration and investigated the dependency of the measured rupture time on molecular adsorption density. The dependency indicated that stabilizing effect of surfactant grows discontinuously from 0 to 0.03 $\mu\text{mol}/\text{m}^2$ and increases with the adsorption density linearly above 0.03 $\mu\text{mol}/\text{m}^2$.

Relation between Micelle Disintegration and Turbulent Transition in Drag-Reducing Surfactant Solution Flow

Tatsuro WAKIMOTO, Koichi ARAGA(Kinki University Technical College), Kenji KATOH and Shin'ya MORIMOTO

Proc. ASME-JSME-KSME Joint Fluids Engineering Conf. 2015, Seoul July 26-31, No. 19561 (2 pages, USB memory) (2015)

It is widely known that the addition of a certain kind of surfactant reduces drag in a pipe flow. This effect is considered to be a result of suppression of turbulent transition caused by ordered structure of rod-like micelles, which is referred to as Shear-Induced Structure, SIS. However, this hypothesis is not verified conclusively and the mechanism of the drag reduction is not fully understood because the detection of SIS is very difficult in an actual moving flow. In this study, we determine the relationship between the SIS and the

turbulent transition in a pipe flow by simultaneous measurement of the amount of the micelles and coefficient of pipe friction. The amount of micelles was measured by fluorescence probe method. When the micelles are formed, fluorescence intensity is reduced since the fluorescence probe is entrapped in the micelle. In this study, it is revealed that the fluorescence intensity also decreases with SIS construction. In addition, experimental results demonstrate that fluorescence intensity change has high correlation to turbulent transition. It suggests that disintegration of SIS in near-wall region causes turbulent transition.

Ultrasonic Detection of Uncured Region in GFRP Laminates for Rehabilitation of Sewerage Pipes

Akihiro WADA, Tomohiro YAMASAKI, Eiji KITAGAWA and Hiroshi ITO

J. Jpn. Soc. Comp. Mat., Vol.41, No.4, pp.128-137 (2015) (in Japanese)

A new technique using Lamb wave is proposed to detect uncured region in GFRP laminates nondestructively. Polymer based composites play an increasingly important role in the field of civil engineering in recent years. For example, laminated sheets consisting of thermoplastic layer, organic fabric sheets and SMC (Sheet Molding Compound) are used to rehabilitate aged sewerage pipes. The cylindrical laminate is inserted in the pipe, and is inflated and cured by steam blowing to create close-fit pipe. This CIPP (Cured in Place Pipe) is one of several trenchless rehabilitation methods to repair aged pipes. In this study, ultrasonic Lamb wave is applied to the detection of uncured region in a laminated composite plate. Oblique incidence method in which ultrasonic waves are launched by the transducer inclined at a selected angle is applied to excite specific mode of Lamb waves in the laminate. Wheel type probes are used to improve inspection efficiency. Beside wave attenuation, AU parameters which are derived from power spectrum of a broadband signal are introduced. It is found that application of AU parameters leads to the improvement of the detectability of uncured region.

Study on Locomotion Mechanisms of an outer- pipe Inspection Robot

Naoto IMAJO, Yogo TAKADA and Mikiji KASHINOKI

Proc. of the 6th International Conference on Positioning Technology, pp.173-178 (2014)

In petrochemical plants, there are a large number of steel pipes running horizontally, vertically, and obliquely, and inspecting them is difficult and time-consuming. There is therefore a strong demand for practical pipe inspection robots to aid in this task. Although several such robots already exist, their mechanism for overcoming obstacles is too bulky to use them on narrow pipes. The aim of the present study is to develop an outer-pipe inspection robot that can move along narrow pipes and wires, and a prototype two-wheel-drive robot has been developed. The wheels are rimless, and each of the sixteen spokes is tipped by a permanent magnet, which allows the robot to remain attached to even a vertical steel pipe. Moreover, the robot has a mechanism for adjusting the camber angle of the right and left wheels, allowing it to tightly grip pipes with different diameters. The robot is equipped with guides at the rear to hold the pipe and prevent yawing motion when it moves along the pipe. Experiments were conducted to check the performance of the inspection robot using steel pipes with different diameters, placed horizontally, vertically or obliquely. The robot attempted to move a certain distance along a pipe, and its success rate was measured. It was found that the robot could successfully travel along pipes with vertical or oblique orientations, although it sometimes fell from horizontal pipes. The most likely reason for this is identified and discussed. Nevertheless, the tests confirmed the practical potential of the robot for pipe-inspection tasks.

Multi-channel Laser Doppler Velocimetry Using a Two-dimensional Optical Fiber Array for Obtaining Instantaneous Velocity Distribution Characteristics

Tomoaki KYODEN, Youichi YASUE, Hiroki ISHIDA, Shunsuke AKIGUCHI, Tsugunobu ANDOH, Yogo TAKADA, Tsunenobu TERANISHI and Tadashi HACHIGA

Japanese Journal of Applied Physics, Robotics, Vol.54, p.012501 (2015)

A laser Doppler velocimeter (LDV) has been developed that is capable of performing two-dimensional (2D) cross-sectional measurements. It employs two horizontal laser light sheets that intersect at an angle of 13.3° . Since the intersection region is thin, it can be used to approximately determine the 2D flow field. An 8×8 array of optical fibers is used to simultaneously measure Doppler frequencies at 64 points. Experiments were conducted to assess the performance of the LDV, and it was found to be capable of obtaining spatial and temporal velocity information at multiple points in a flow field. The technique is fast, noninvasive, and accurate over long sampling periods. Furthermore, its applicability to an actual flow field was confirmed by measuring the temporal velocity distribution of a pulsatile flow in a rectangular flow channel with an obstruction. The proposed device is thus a useful, compact optical instrument for conducting simultaneous 2D cross-sectional multipoint measurements.

High-resolution In-situ LDV Monitoring System for Measuring Velocity Distribution in Blood Vessel

Tomoaki KYODEN, Shotaro ABE, Hiroki ISHIDA, Shunsuke AKIGUCHI, Tsugunobu ANDOH, Yogo TAKADA, Tsunenobu TERANISHI and Tadashi HACHIGA

Optics Communications, Vol. 353, pp. 122-132 (2015)

We herein describe a cross-sectional multiple-point laser Doppler velocimetry (CS-MLDV) system for monitoring blood vessels that are sutured and connected during an operation. In order to observe the condition of a blood vessel during an operation, the previously developed linear MLDV (L-MLDV) system can realize velocity distribution imaging of the carotid artery in a living mouse by means of traverse laser light. We subsequently developed a CS-MLDV system, which can measure the instantaneous two-dimensional (2D) flow velocity, by upgrading the optical components and signal processing used in L-MLDV. The validity of the CS-MLDV results was verified through comparison with the results of a computational fluid dynamics (CFD) analysis. The results of the CFD analysis were similar to the experimental results obtained under the same flow field condition. Moreover, an instantaneous 2D velocity distribution can be obtained even for the case of flowing blood. Finally, we carried out in-vivo measurement in a mesenteric vessel of a mouse in order to demonstrate the potential of the CS-MLDV for use in surgery.

Development and Evaluation of Compact Robot Imitating a Hermit Crab for Inspecting the Outer Surface of Pipes

Naoto IMAJO, Yogo TAKADA and Mikiji KASHINOKI

Journal of Robotics, Vol. 2015, Article ID 312780 (7 Pages) (2015)

Terrestrial hermit crabs which are a type of hermit crabs live on land, whereas typical hermit crabs inhabit the sea. They have an ability of climbing a tree vertically. Their claws allow them to hang on the tree. In this study, an outer-pipe inspection robot was developed. Its locomotion mechanism was developed in imitation of the terrestrial hermit crab's claws. It is equipped with two rimless wheels. Each of the spokes is tipped with a neodymium magnet, which allows the robot to remain attached to even a vertical steel pipe. Moreover, the robot has a mechanism for adjusting the camber angle of the right and left wheels, allowing it to tightly grip pipes with different diameters. Experiments were conducted to check the performance of the robot using steel pipes with different diameters, placed horizontally, vertically, or obliquely. The robot attempted to move a certain distance along a pipe, and its success rate was measured. It was found that the robot could successfully travel along pipes with vertical orientations, although it sometimes fell from oblique or horizontal pipes. The most likely reason for this is identified and discussed. Certain results were obtained in laboratory. Further experiments in actual environment are required.

Effects of NaOCl Aqueous Solutions and Ethyl Alcohol Solutions on Removing Protein Surface Contaminants and Re-establishing Antibacterial Activities of Copper-Alloyed Stainless Steel

Hiroshi KAWAKAMI, Hideaki NISHIKUBO, Keita HIRAYAMA, Satoshi SUZUKI (Nisshin Steel Co., Ltd.), Yoshihiro SATO and Yasushi KIKUCHI

Biocontrol Sci., Vol. 20, pp. 193-198 (2015)

Effects of wiping copper-alloyed stainless steel surfaces with disinfectants to remove protein surface contaminants and re-establish their antibacterial activities were quantitatively studied. Disinfectants used were sodium hypochlorite aqueous solutions and ethyl alcohol aqueous solutions. Wiping with NaOCl aqueous solutions effectively removed protein surface contaminants. Ethyl alcohol aqueous solutions were also effective for cleaning, but their efficiency was less than that of NaOCl aqueous solutions. When the amount of residual surface contaminants was reduced to 0.4 ng/mm^2 , the surfaces of the copper-alloyed stainless steel regained antibacterial activities to the same level as those in a clean surface condition.

Mechanical properties of Fiber/Matrix Interface in Polymer Matrix Composites

Jun KOYANAGI, Shinji OGIHARA, Hayato NAKATANI, Tomonaga OKABE and Satoru YONEYAMA

Advanced Composite Materials, Vol. 23, pp. 551-570 (2014)

This paper reviews the mechanical properties of interface adhesion between the fiber and matrix mainly by interpreting the authors' past articles. First, the methods for evaluating interface mechanical properties are described considering micromechanical testing using single-fiber composite specimens. In particular, the test-type dependence of the obtained interfacial strength is discussed, and this paper suggests that the cruciform specimen technique is an appropriate testing method. Then, this paper presents another way to obtain interface properties that is extracted from a bulk composite test. Moreover, the time and temperature dependence of the interface strength and the interface failure envelope under a combined stress state are

described, respectively. Interface toughness is also discussed at the end of this paper, and it is implied that the value might be much lower than those presented in many conventional articles.

A Two-step Hybrid Technique for Accurately Localizing Acoustic Source in Anisotropic Structures Without Knowing Their Material Properties

Tribikram KUNDU, Xiaojuan YANG, Hayato NAKATANI and Nobuo TAKEDA

Ultrasonics, Vol. 56, pp. 271-278 (2015)

Acoustic source localization techniques generally assume straight line propagation of waves from the acoustic source to the sensor. However, it is well-known that in anisotropic plates the acoustic energy does not always propagate in straight lines. Even for isotropic plates containing a cavity or an inclusion between the acoustic source and the sensor the straight line propagation assumption is violated. In such cases only options available in localizing acoustic source is to use relatively expensive distributed sensor systems, or to follow time reversal techniques based on the impulse response functions which is labor intensive and computationally demanding. A two-step hybrid technique is proposed in this paper for predicting acoustic source in anisotropic plates. During the first step it was assumed that the waves propagated along straight lines from the acoustic source to the sensor. The source was localized with this simplifying assumption. Then this first prediction was improved in the second step by solving an optimization problem. Experimental results showed that the second step always moved the estimates towards the actual source location. Thus it always reduced the prediction error irrespective of whether the final prediction coincided with the actual source location or not.

Effect of Fiber Discontinuity on Mechanical Properties of Interlaminar-toughened CFRP Laminates

Yu NAGATA, Hayato NAKATANI, Akira MATSUBA, Yousuke KOUNO and Shinji OGIHARA

Transactions of the JSME, Vol. 81, No. 825 (2015) (in Japanese)

In fabricating complicated laminated composite structures by using prepregs, various kinds of fiber discontinuities such as ply drop-off and seams can be formed. Special care must be taken for the fiber discontinuity since they can induce stress concentration, and damage onset and growth originated from them may lead to catastrophic failure of the structure. The present study evaluates mechanical behaviour in unidirectional CFRP laminates that contain centered or dispersed fiber discontinuities fabricated by using interlaminar-toughened CFRP prepregs. Tensile testing has shown that higher onset stress of the interlaminar delamination between continuous and discontinuous plies can be achieved by interlaminar-toughened CFRP with centered fiber discontinuity compared to that for conventional CFRP prepregs. As for the specimen with dispersed fiber discontinuities, fracture stress keeps almost constant with more than 20 mm of interval of the dispersed fiber discontinuities. By applying the onset stress of the delamination that is experimentally obtained using centered discontinuity to an analytical model, critical energy release rate by the delamination onset is calculated. Then it is indicated that one can predict the fracture stress of the specimen with the dispersed fiber discontinuities with more than 20 mm interval of the discontinuities by using the critical energy release rate. This indicates that fracture of the laminate is dominated by the interlaminar delamination between discontinuous plies with more than 20 mm of interval.

Distance-domain Based Localization Techniques for Acoustic Emission Sources: A Comparative Study

Krzysztof GRABOWSKI, Mateusz GAWRONSKI, Hayato NAKATANI, Pawel PACKO, Ireneusz BARAN, Wojciech SPYCHALSKI, Wieslaw STASZEWSKI, Tadeusz UHL and Tribikram KUNDU

Proc. SPIE 9438, Health Monitoring of Structural and Biological Systems 2015, 94381T (2015); doi:10.1117/12.2084296, (from Conference Volume 9438, San Diego, California, USA, March 8, 2015)

Acoustic Emission phenomenon is of great importance for analyzing and monitoring health status of critical structural components. In acoustic emission, elastic waves generated by sources propagate through the structure and are acquired by networks of sensors. Ability to accurately locate the event strongly depends on the type of medium (e.g. geometrical features) and material properties, that result in wave signals distortion. These effects manifest themselves particularly in plate structures due to intrinsic dispersive nature of Lamb waves. In this paper two techniques for acoustic emission source localization in elastic plates are compared: one based on a time-domain distance transform and the second one is a two-step hybrid technique. A time-distance domain transform approach, transforms the time-domain waveforms into the distance domain by using wavenumber-frequency mapping. The transform reconstructs the source signal removing distortions resulting from dispersion effects. The method requires input of approximate material properties and geometrical features of the structure that are relatively easy to estimate prior to measurement. Hence, the method is of high practical interest. Subsequently, a two-step hybrid technique, which does not require a

priori knowledge of material parameters, is employed. The method requires a setup of two predefined clusters of three sensors in each. The Lamb wave source is localized from the intersection point of the predicted wave propagation directions for the two clusters. The second step of the two-step hybrid technique improves the prediction by minimizing an objective function. The two methods are compared for analytic, simulated and experimental signals.

Suppression of Interlaminar Crack in UD-CFRP containing Fibre Discontinuity using Polyamide Mesh

Hayato NAKATANI, Tatsuya IMAMURA and Katsuhiko OSAKA

Proc. 20th International Conference on Composite Materials, Copenhagen, Denmark, July 19-24, Paper ID 1115-6 (2015)

A fiber discontinuity in fibre reinforced composite laminates may act as a source of stress concentration that induces damage onset. A mesh made of thermoplastic polyamide (PA) as an interlayer is inserted between fiber continuous and discontinuous plies in order to suppress an interlaminar cracking as a second damage mode in unidirectional CFRP laminates that contain centred fiber discontinuity. It is experimentally shown that by inserting PA mesh the onset stress of the interlaminar crack increased significantly. The end notched flexure (ENF) testing using unidirectional CFRP laminates with PA mesh inserted demonstrates that the mode II interlaminar fracture toughness $G_{IIC} = 1.91 \text{ kJ/m}^2$ can be achieved; this should be compared to 1.30 kJ/m^2 without PA mesh. It is also shown that the mode II interlaminar fracture toughness $G_{IIC'} = 3.67 \text{ kJ/m}^2$ which is related to the second critical load, not the first one, during ENF testing should be applied to the prediction of the crack onset stress by using an analysis model that incorporates energy release rate by the crack growth.

Optimization of Acoustic Source Localization in Large Plates

Krzysztof GRABOWSKI, Mateusz GAWRONSKI, Hayato NAKATANI, Pawel PACKO, Wieslaw J. STASZEWSKI, Tadeusz UHL and Tribikram KUNDU

Proc. 10th International Workshop on Structural Health Monitoring 2015, Stanford University, Palo Alto, CA, USA, Sep. 1-3, DOI:10.12783/SHM2015/194 (2015)

Acoustic Emission (AE) is a phenomenon of great importance for structural health monitoring (SHM). One of important applications of AE in SHM is the localization of a source of acoustic energy in the structure. For certain types of structures and for large propagation distances where dispersion phenomenon is prominent, it is hard to estimate proper location of the damage. This paper discusses some aspects of AE source localization techniques. It is shown how an acoustic source in large plates can be localized using only six sensors and without *a priori* knowledge of any material parameter, thus omitting the need of considering dispersion phenomena. The method is based on a predefined three-sensor setup, required to determine the Lamb wave propagation direction by detecting the angle at which the Lamb wave hits the array. As introduced in earlier works, the propagation direction of the Lamb wave is detected using arrival time differences between sensors, measured by correlating only the first dip and peak of the recorded signals. With another propagation direction detected by another sensor cluster the acoustic source can be localized as an intersection point of the two directions for planar structures. In this paper special orientation of the sensor cluster is suggested in order to apply the technique to a narrow plate. This modification enables to evaluate a wider area and avoid possible errors in detected propagation directions from some acoustic source locations. The method is compared with another source localization technique based on combined time-domain dispersion removal approach and localization. The dispersion removal technique reconstructs the source signal compensating distortions resulting from dispersion effects and transforms the time domain response directly into the distance one. Both methods are verified numerically and experimentally through artificial sources.

Nondestructive Evaluation and 3-D Imaging of Impact Damage in CFRP/Ti Fibre-Metal Laminates using Synchrotron Radiation Laminography

Hayato NAKATANI, Kentaro KAJIWARA, Koichi AKITA and Shinji OGIHARA

Proc. 14th Japanese-European Symposium on Composite Materials, Kanazawa, Japan, Sep. 16-18, ExtAbst_Nakatani.pdf (USB Memory) (2015)

Fibre-Metal Laminates (FMLs) are hybrid materials that consist of thin layers of metal and fibre-reinforced polymer, and have already been applied several military and commercial aircraft. It is well-known that there is a difficulty in non-destructive assessment of damage in FMLs using laboratory radiography or X-ray computed tomography since FMLs have laminate structure of materials with different X-ray absorption

coefficient. Synchrotron radiation laminography at SPring-8 in Japan is employed to assess low velocity impact damage in CFRP/Ti laminates as FMLs. During computed laminography synchrotron radiation beam is irradiated to an object with the axis of rotation inclined at an angle and thus it is suitable for the laterally extended geometry of composite laminate plates. It is verified that how each damage mode, such as crack in titanium layer, fibre break, matrix cracking, interlaminar delamination in CFRP layers and interfacial debonding between CFRP and titanium layers, can be observed in obtained reconstructed slice images. Three-dimensional imaging of the low velocity impact damage is also demonstrated by stacking the reconstructed slice images, and that is to our knowledge a novel result.

Lattice Rotation in Fe-20%Cr Alloy Single Crystals Subjected to Sliding Wear

Yoshihisa KANEKO and Mutsumi NISHII

J. Soc. Mater. Sci. Japan, Vol. 64 pp.281-286 (2015)

Sliding wear tests were conducted on Fe-20%Cr alloy single crystals having (001), (110) and (111) surfaces, using the ball-on-disk type friction machine under the condition of 10N vertical load and 30m wear distance. After the wear tests, the single crystals were cut to investigate microstructures developed below the worn surface. The cross-sectional observation revealed that subsurface regions of all the worn single crystals were composed of fine grains which were generated by severe plastic deformation introduced by the sliding wear process. It was confirmed from EBSD analyses that, below the fine-grained regions, all the single crystals rotated around the axis which is almost perpendicular to the wear direction. Such lattice rotation was expected to be a preceding event for the grain boundary formation in the fine-grained region. The lattice rotations were evaluated by the misorientation angles from the single crystal matrices. Extent of the lattice rotation depended on crystallographic orientation of the single crystals. The depth where the misorientation angle is 10° increased in ascending order of (001), (110) and (111) single crystals, suggesting that the lattice rotation was promoted favorably at the (111) single crystal. In order to understand the orientation dependence of the lattice rotation, we considered three slip deformation models (horizontal shear, vertical shear and resolved shear stress models) which incorporated the geometrical relationship between a slip system and wear direction.

Multi-scale modeling of degradation behavior for crystalline polymer

Masakazu KUDO, Junichi TAKAHASHI, Toshiharu YAMAMOTO, Makoto UCHIDA and Yoshihiro TOMITA

J. Soc. Mater. Sci. Japan, Vol. 64, pp. 311-366 (2015)

Coarse-grained molecular dynamics simulations are conducted, for the purpose of the study on the microscopic structure change of crystalline polymer due to degradation. Interlamellar structure changes are observed during the degradation, decreasing loop and bridge chains, increasing short tail chains. From the elongation simulation of lamellar structure, craze strength is dropped during the degradation, because of decreasing oriented interlamellar chains and drawing of the molecular chains from the crystal part. Multi-scale modeling is conducted to demonstrate the relationship between microscopic structure changes and macroscopic mechanical properties. As a result, macroscopic fracture strain is reduced by the degradation, because craze growth rate becomes faster with the degradation.

Computational simulation of micro- to macroscopic deformation behavior of cavitated rubber blended amorphous polymer using second-order homogenization method

Makoto UCHIDA and Naoya TADA

Key Engineering Materials, Vol. 626, pp. 74-80 (2015)

To evaluate the effect of the size of the microstructure on the mechanical property of the cavitated rubber blended (voided) amorphous polymer, the FEM simulation based on the rate form second-order homogenization method, in which rates of the macroscopic strain and strain gradient are given to the microstructure, was performed. Computational simulations of micro- to macroscopic deformation behaviors of amorphous polymers including different sizes and volume fractions of the voids were performed. Non-affine molecular chain network theory was employed to represent the inelastic deformation behavior of the amorphous polymer matrix. With the increase in the volume fraction of the void, decrease and periodical fluctuation of stress and localized deformation in the macroscopic field were observed, and were more emphasized with the increase in the size of the void. These results were closely related to the non-uniform deformation and volume increase of the void in the microscopic field.

Potential difference distribution on flat plate around semi-ellipsoidal thinning on the back surface

Naoya TADA, Makoto UCHIDA and Manabu NOHARA

Proceedings of the ASME 2014 Pressure Vessels & Piping Conference (PVP2014), Paper No. PVP2014-28684 (2014)

Local wall thinning is one of serious problems in aged power generating plants and is known to occur mainly by Flow Accelerated Corrosion (FAC) and Liquid Droplet Impingement (LDI) erosion. As the thinning grows inside the pipes, it is difficult to detect and evaluate it from the outer surface of pipe. The direct-current potential difference method (DC-PDM) is thought to be a suitable non-destructive technique to monitor the initiation and growth of these damages. In this study, an approximate analysis method of the potential difference around a semi-ellipsoidal thinning on the back surface of flat plate is presented and the accuracy is discussed based on the results obtained by the finite element analyses.

Transient Viscoelastic Behavior of Glassy Epoxy Networks with Various Crosslink Densities under Large Deformation

Shin'ya YOSHIOKA and Ryuki MASUDA

J. Soc. Mat. Sci. Jpn., Vol.64, pp.52-56 (2015). (in Japanese)

The single relaxation time of glassy epoxy networks having different crosslink densities was evaluated during uniaxial compression processes by using a simple nonlinear single relaxation model to study the effect of crosslinked molecular structures on the transient nonlinear viscoelastic behavior of glassy epoxy networks. The model consisted of two elastic springs expressing linear viscoelastic behavior and a dashpot with variable viscosity as a single parameter representing strain-induced structural change. We calculated the strain-dependent relaxation time τ_{SS} during the compression by fitting the model to the experimental stress-strain curves obtained at various strain rates and at temperatures T 18°C lower than the glass transition temperature T_g of the material being compressed. With increasing strain ϵ_n , τ_{SS} obtained for each epoxy network steeply decreased in the pre-yield region of strain and then reached to low steady values appearing in strain ranges larger than the yield strain, reproducing previously reported typical behavior observed for glassy polymers under large deformation. When compressed at an identical strain rate, τ_{SS} - ϵ_n relations for all epoxy networks almost coincided each other despite the difference in the crosslink density. This result indicates that, if the deformation is performed at the same condition i.e., strain rate and $T-T_g$, strain-induced variation of relaxation time in the epoxy glasses is almost not influenced by crosslinked molecular structures.

Applied Physics and Electronics

4H-SiC/Si Heterojunction Bipolar Transistors Fabricated by Surface Activated Bonding

Jianbo LIANG, Sae SHIMIZU, Shota NISHIDA, Naoteru SHIGEKAWA and Manabu ARAI (New Japan Radio Co. Ltd.)

ECS Solid State Lett., Vol. 4, Q55 (3 pages) (2015)

4H-SiC/Si heterojunction bipolar transistors with emitter-up (E-up) and collector-up (C-up) configurations were fabricated by surface activated bonding for the first time. Their electrical characteristics were measured at raised ambient temperatures. The common-base current gain α increased as the temperature was raised in the both E-up and C-up structures. In the E-up structure, α reached to ≈ 0.99 at 573 K. Improvements in both device structures and surface activated bonding conditions should provide further improvements in device performance.

MOCVD Growth of Thick ($\sim 1 \mu\text{m}$) InGaN on AlN/Si Substrates for InGaN/Si Tandem Solar Cells

Akio YAMAMOTO (Univ. of Fukui), Kazuki KODAMA (Univ. of Fukui), Md. Tanvir HASAN (Univ. of Fukui), Naoteru SHIGEKAWA and Masaaki KUZUHARA (Univ. of Fukui)

Jpn. J. Appl. Phys., Vol. 54, 08KA12 (4 pages) (2015)

In order to develop key technologies for InGaN/Si two-junction tandem solar cells, MOVPE growth of thick InGaN on Si p-on-n cell structures has been studied. By clarifying the phase separation behavior of MOVPE InGaN, a thick ($\sim 1 \mu\text{m}$) $\text{In}_x\text{Ga}_{1-x}\text{N}$ ($x \sim 0.5$) without phase separation is successfully grown on AlN/Si(111) wafers. A sufficient current flow for the operation of the tandem cell is obtained through n-InGaN/AlN/p-Si structures by employing the annealing of AlN/Si wafer at around 1000 °C in NH_3 flow just before InGaN growth. The annealing of AlN/Si wafers also brings about the degradation of the underlying Si pn junction. The optimization of the annealing conditions is required to balance such favorable and unfavorable effects.

Current-Voltage and Spectral-Response Characteristics of Surface-Activated-Bonding-Based InGaP/GaAs/Si Hybrid Triple-Junction Cells

Naoteru SHIGEKAWA, Jianbo LIANG, Ryusuke ONITSUKA (Sharp Co.), Takaaki AGUI (Sharp Co.), Hiroyuki JUSO (Sharp Co.) and Tatsuya TAKAMOTO (Sharp Co.)

Jpn. J. Appl. Phys., Vol. 54, 08KE03 (5 pages) (2015)

We measured the current–voltage (I–V) and spectral-response characteristics of InGaP/GaAs/Si hybrid triple-junction cells that were fabricated by using surface-activated bonding methods. We found by spectral response measurements that the current generated in the Si-based bottom cell was lower than those in the top and middle cells under the conditions of an air mass of 1.5G and one sun. Furthermore we observed a discrepancy between the short-circuit current, which was obtained by subtracting the estimated contribution of Si ledges surrounding InGaP/GaAs mesas to the I–V characteristics, and the results of spectral response measurements. One possible model for explaining the discrepancy was discussed on the basis of the electrical coupling scheme between subcells. The intrinsic conversion efficiency of a $5 \times 5 \text{mm}^2$ triple-junction cell was crudely estimated to be $>26\%$ by compensating for the shadow loss as well as subtracting the contribution of Si ledges.

Growth Temperature Dependent Critical Thickness for Phase Separation in Thick ($\sim 1 \mu\text{m}$) $\text{In}_x\text{Ga}_{1-x}\text{N}$ ($x = 0.2-0.4$)

Akio YAMAMOTO (Univ. of Fukui), Tanvir Md HASAN (Univ. of Fukui), Kazuki KODAMA (Univ. of Fukui), Naoteru SHIGEKAWA and Masaaki KUZUHARA (Univ. of Fukui)

J. Crystal Growth, Vol. 419, pp. 64-68 (2015)

This paper reports phase separation in thick ($\sim 1 \mu\text{m}$) MOVPE $\text{In}_x\text{Ga}_{1-x}\text{N}$ ($x=0.2-0.4$) films grown by MOVPE at 570–750 °C on AlN/Si(111), $\alpha\text{-Al}_2\text{O}_3(0001)$ and GaN/ $\alpha\text{-Al}_2\text{O}_3(0001)$ substrates. Phase separation occurs when InGaN thickness exceeds a critical value. Critical thickness for phase separation is markedly increased with decreasing growth temperature. It is around 0.2 μm for a film grown at 750 °C, while it is more than 1 μm for that grown at 570 °C. No substrate dependencies are found in critical thickness. The cross-sectional SEM views of phase-separated films grown at 650 °C show that phase separation is initiated at parts far more than 0.2 μm from the substrate and extended to the area near the substrate. SIMS analysis shows a possibility that phase separation is initiated at a part with relatively large In/Ga ratio fluctuations in InGaN films.

Thick (~1 μm) p-type In_xGa_{1-x}N (x~0.36) Grown by MOVPE at a Low Temperature (~570 °C)

Akio YAMAMOTO (Univ. of Fukui), Tanvir Md HASAN (Univ. of Fukui), Kazuki KODAMA (Univ. of Fukui), Naoteru SHIGEKAWA and Masaaki KUZUHARA (Univ. of Fukui)

Physica Stat. Solidi B, Vol. 1-4, pp. 909-912 (2015)

This paper reports the post-growth annealing effects of low temperature grown Mg-doped InGaN. By using MOVPE, 1 μm-thick Mg-doped In_xGa_{1-x}N (x ~ 0.36) films are grown at 570 °C. In order to activate the Mg acceptors, grown samples are treated by the conventional furnace annealing (FA) or the rapid thermal annealing (RTA). In the case of the FA at 650 °C for 20 min, the InGaN film is phase-separated. On the other hand, the RTA at a temperature higher than 700 °C enables us to get p-type samples. By using the RTA at 850 for 20 s, p-type samples with a hole concentration 10¹⁸–10¹⁹ cm⁻³ are successfully obtained without phase separation.

Investigation on the Interface Resistance of Si/GaAs Heterojunctions Fabricated by Surface-Activated Bonding

Jianbo LIANG, Li CHAI, Shota NISHIDA, Masashi MORIMOTO and Naoteru SHIGEKAWA

Jpn. J. Appl. Phys., Vol. 54, 030211 (5 pages) (2015)

The electrical properties of p-GaAs/n⁺-Si, p⁺-Si/n-GaAs, p⁺-GaAs/n⁺-Si, p⁺-Si/n⁺-GaAs, n⁺-Si/n⁺-GaAs, and p⁺-Si/p⁺-GaAs junctions fabricated by surface-activated bonding (SAB) were investigated. An amorphous layer with a thickness of 3nm was found across the bonding interface without annealing. The current–voltage (I–V) characteristics of p⁺-GaAs/n⁺-Si, p⁺-Si/n⁺-GaAs, n⁺-Si/n⁺-GaAs, and p⁺-Si/p⁺-GaAs junctions showed excellent linearity. The interface resistance of n⁺-Si/n⁺-GaAs junctions was found to be 0.112Ω·cm², which is the smallest value observed in all the samples. The resistance decreased with increasing annealing temperature and decreased to 0.074Ω·cm² after the junction annealing at 400 °C. These results demonstrate that n⁺-Si/n⁺-GaAs junctions are suitable for the connection of subcells in the fabrication of tandem solar cells.

Effects of Annealing on Electrical Properties of Si/Si Junctions by Surface-Activated Bonding

Masashi MORIMOTO, Jianbo LIANG, Shota NISHIDA and Naoteru SHIGEKAWA

Jpn. J. Appl. Phys., Vol. 54, 030212 (5 pages) (2015)

Effects of annealing on surface-activated bonding (SAB)-based Si/Si junctions were investigated by transmission electron microscopy (TEM) observations and current–voltage (I–V) measurements. We observed an amorphous-like layer at the bonding interface, which was recrystallized by annealing. We extracted the potential barrier heights at Si/Si interfaces annealed at different temperatures from the results of I–V measurements at various ambient temperatures. For p-Si/p-Si junctions, the barrier height increased as the annealing temperature increased from 200 to 400 °C and decreased from 400 to 1000 °C. For n-Si/n-Si junctions, the barrier height increased as the annealing temperature increased from 200 to 600 °C and decreased from 600 to 1000 °C. By using the charge neutral level (CNL) model, we estimated the energy of CNL, E_{CNL} , and the density of interface states, D_{it} , at each annealing temperature. D_{it} decreased as the annealing temperature increased from 400 to 1000 °C. E_{CNL} showed values larger than the reported ones.

Correlation between the Electrical Properties of p-Si/n-4H-SiC Junctions and Concentrations of Acceptors in Si

Shota NISHIDA, Jianbo LIANG, Tomohiro HAYASHI, Manabu ARAI (New Japan Radio Co. Ltd.) and Naoteru SHIGEKAWA

Jpn. J. Appl. Phys., Vol. 54, 030210 (4 pages) (2015)

We fabricated p⁺-, p-, and p⁻-Si/n-4H-SiC junctions by surface activated bonding (SAB). We investigated their electrical properties by measuring their current–voltage (I–V) characteristics at raised ambient temperatures, capacitance–voltage (C–V) characteristics at various frequencies, and capacitance–frequency (C–f) characteristics at room temperature. The activation energy of their reverse-bias current and the flat-band voltage in their C–V characteristics, which were estimated to be 0.97–1.01 eV and 0.83–0.84V, respectively, were insensitive to the concentrations of acceptors in Si substrates. The relaxation times estimated from the C–f characteristics were 0.8 and 1.5 μs for the p-Si/n-4H-SiC and p⁻-Si/n-4H-SiC junctions, respectively. The results are explained by a scheme wherein Fermi level pinning occurs at the Si/4H-SiC interfaces fabricated by SAB.

Influence of InGaN/GaN Multiple Quantum Well Structure on Photovoltaic Characteristics of Solar Cell

Noriyuki WATANABE (NTT Laboratories), Manabu MITSUHARA (NTT Laboratories), Haruki YOKOYAMA (NTT Laboratories), Jianbo LIANG and Naoteru SHIGEKAWA

Jpn. J. Appl. Phys., Vol. 53, 112301 (9 pages) (2014)

We have investigated InGaN/GaN multiple quantum well (MQW) solar cells in terms of the relationship between the short-circuit current and the MQW structure. We previously reported that higher short-circuit current is obtained in solar cells with thinner GaN barrier layers, and in this investigation, we also obtained higher short-circuit current in solar cells with higher numbers of InGaN/GaN periodic layers. These results can be explained by the hypothesis that the transport characteristics of photoinduced carriers are characterized by the specific length within which carriers photoinduced in the InGaN well layer can move before recombination. The carrier collection efficiency is improved by the drift in the barrier layer due to the forward internal electric field and degraded by the carrier accumulation in the well layer caused by the inverse internal electric field and the potential barrier between layers, which well describes the influence of the MQW structure on the specific length. Using this model, we discuss how we can determine the MQW structure that yields higher short-circuit current, and conclude that the optimum thickness of the InGaN well layer is about 2–3 nm when the thickness of the GaN barrier layer is 3–8 nm.

Effects of Interface State Charges on the Electrical Properties of Si/SiC Heterojunctions

Jianbo LIANG, Shota NISHIDA, Tomohiro HAYASHI, Manabu ARAI (New Japan Radio Co. Ltd.) and Naoteru SHIGEKAWA

Appl. Phys. Lett., **105**, 151607 (4 pages) (2014)

Electrical properties of p^+ -Si/n⁻-SiC, p-Si/n⁻-SiC, p^- -Si/n⁻-SiC, and n^+ -Si/n⁻-SiC heterojunctions fabricated by using surface-activated bonding are investigated. Their flat-band voltages obtained from capacitance-voltage (C-V) measurements are found to be ~0.92 eV, which suggests that the Fermi level should be pinned at the bonding interface. An analysis by using the charge neutral level model reveals that the C-V characteristics are sensitive to the density of interface states. The measured C-V characteristics of p^+ -Si/n⁻-SiC and n^+ -Si/n⁻-SiC junctions are in quantitative agreement with modeled ones obtained for the interface states density and the conduction-band discontinuity of $2.3 \times 10^{13} \text{ cm}^{-2} \text{ eV}^{-1}$ and 0.3 eV, respectively.

Hybrid Triple-Junction Solar Cells by Surface Activate Bonding of III-V Double-Junction-Cell Heterostructures to Ion-Implantation-Based Si Cells

Naoteru SHIGEKAWA, Li CHAI, Masashi MORIMOTO, Jianbo LIANG, Ryusuke ONITSUKA (Sharp Co.), Takaaki AGUI (Sharp Co.), Hiroyuki JUSO (Sharp Co.) and Tatsuya TAKAMOTO (Sharp Co.)

Proc. 40th IEEE Photovoltaic Specialists Conference, pp. 534-537 (2014)

A hybrid triple-junction cell was fabricated by surface activated bonding of a lattice-matched invertedly-grown InGaP/GaAs double-junction cell to an ion-implantation-based Si bottom cell. An n^+ -doped layer on the top of bottom cell due to the ion implantation worked as its emitter and bonding layer for the tunnel junction. The bonding interface was found to be stable after the annealing at 400 °C. An efficiency of 24.4% was achieved at air mass 1.5G and one sun at room temperature.

Type-II Band Profile of GaAs/Si Hetero Junctions by Surface Activated Bonding for Hybrid Tandem Cells

Naoteru SHIGEKAWA, Jianbo LIANG, Masashi MORIMOTO and Shota NISHIDA

ECS Trans., Vol. 64, pp. 235-242 (2014)

We fabricated p^+ -GaAs/n-Si and n^+ -GaAs/p-Si junctions by using surface activated bonding and measured their current-voltage and capacitance-voltage characteristics at room temperature. Their conduction band offset, which was extracted from the capacitance-voltage characteristics, was 0.57-0.84 eV. The results suggested that the band profiles of junctions had type-II features, which was likely to be preferable for fabricating low-resistance tunnelling junctions in hybrid tandem cells. The influence of possible interface states on the electrical properties of junctions was also discussed using the charge neutral level model.

Photoemission Spectroscopy Measurements of p^+ -Si/n-SiC and n^+ -Si/n-SiC Junctions by Surface Activated Bonding

Naoteru SHIGEKAWA, Jianbo LIANG, Masato SHINGO (Univ. of Fukui), Manabu ARAI (New Japan Radio Co. Ltd.) and Kenji SHIOJIMA (Univ. of Fukui)

Extended Abstracts of the 2015 International Conference on Solid State Devices and Materials, Sapporo, PS-14-12, pp. 508-509 (2015)

Photoemission spectroscopy measurements were performed for p^+ -Si/n-SiC and n^+ -Si/n-SiC junctions that

had been fabricated using the surface activated bonding. The optical absorption edge was estimated to be 1.36-1.4 and 1.6 eV for the p⁺-Si/n-SiC and n⁺-Si/n-SiC junctions, respectively. The difference in the optical absorption edges as well as that in the responses to bias voltages were discussed in conjunction with the potential profile across the bonding interfaces.

Mapping of Si/SiC Hetero p-n Junctions Using Scanning Internal Photoemission Microscopy

Masato SHINGO (Univ. of Fukui), Jianbo LIANG (Univ. of Fukui), Naoteru SHIGEKAWA, Manabu ARAI (New Japan Radio Co. Ltd.) and Kenji SHIOJIMA (Univ. of Fukui)

Extended Abstracts of the 2015 International Conference on Solid State Devices and Materials, Sapporo, PS-14-11, pp. 506-507 (2015)

We have demonstrated scanning internal photoemission microscopy (SIPM) to map p⁺-Si/n-SiC hetero p-n junctions. By focusing and scanning a laser beam over the junction, a photocurrent map was clearly obtained, and nm-deep scratches were visualized as a pattern. We found that this method is a powerful tool to investigate inhomogeneity of the heterojunctions.

Transport Characteristics of Minority Carriers in 4H-SiC/Si Heterojunction bipolar transistor structures fabricated by surface activated bonding

Jianbo LIANG, Sae SHIMIZU, Shota NISHIDA, Naoteru SHIGEKAWA and Manabu ARAI (New Japan Radio Co. Ltd.)

Extended Abstracts of the 2015 International Conference on Solid State Devices and Materials, Sapporo, PS-14-5, pp. 494-495 (2015)

4H-SiC/Si heterojunction bipolar transistor structures with emitter-up (E-up) and collector-up (C-up) configurations were fabricated by surface activated bonding. Their electrical characteristics were measured at raised ambient temperatures. The common-based current gain α increased as the temperature was raised. The activation energy of α was found to be 0.05 and 0.18 eV for the E-up and C-up structures, respectively. In the E-up structures, α reached to 0.99 at 573 K.

MOVPE Growth and Device Fabrication of Thick n⁺-p InGaN with in Composition of 0.3 and No Phase Separation at 600 °C

Kazuki KODAMA (Univ. of Fukui), Hiroyuki NOMURA (Univ. of Fukui), Naoteru SHIGEKAWA, Akio YAMAMOTO (Univ. of Fukui), and Masaaki KUZUHARA (Univ. of Fukui)

Abstracts of the 11th International Conference on Nitride Semiconductors, Beijing, 2015, TuGP84 (2 pages) (2015)

Electrical Properties of Room Temperature Bonded Si/GaN Heterojunctions without Buffer Layers

Jianbo LIANG, Takuya NISHIMURA, Noriyuki WATANABE (NTT Laboratories) and Naoteru SHIGEKAWA

Abstracts of the 11th International Conference on Nitride Semiconductors, Beijing, WeEP6 (2 pages) (2015)

The electrical properties of n⁺-Si/n-GaN and p⁺-Si/n-GaN heterojunctions without buffer layers fabricated by room temperature bonding were investigated. The current-voltage (I-V) characteristics of n⁺-Si/n-GaN and p⁺-Si/n-GaN heterojunctions showed excellent linearity and rectifying properties, respectively. The flat-band voltage of p⁺-Si/n-GaN heterojunctions was found to be 1.2 V from capacitance-voltage (C-V) measurements, which determines that the valence and conduction band discontinuities are 2.15 and 0.15 eV, respectively, which indicates a type -I band alignment.

Band Lineups in GaAs/GaN Junctions Using Surface-Activated Bonding

Syoji YAMAJO, Jianbo LIANG, Noriyuki WATANABE (NTT Laboratories) and Naoteru SHIGEKAWA

Abstracts of 11th Topical Workshop on Heterostructure Microelectronics (TWHM 2015), Takayama, pp. 41-42 (2015).

Impacts of Annealing in N₂/H₂ Ambient on Electrical Properties of Si/GaN Junctions

Takuya NISHIMURA, Jianbo LIANG, Noriyuki WATANABE (NTT Laboratories) and Naoteru SHIGEKAWA

Abstracts of 11th Topical Workshop on Heterostructure Microelectronics (TWHM 2015), Takayama, pp. 39-40 (2015)

Fabrication and Characterization of GaAs/4H-SiC Junctions by Using SAB

Sae SHIMIZU, Jianbo LIANG, Manabu ARAI (New Japan Radio Co., Ltd.) and Naoteru SHIGEKAWA
Abstracts of 11th Topical Workshop on Heterostructure Microelectronics (TWHM 2015), Takayama, pp. 37-38 (2015)

Fabrication and Characterization of Si-Based Bipolar Transistor Structures Using Low-Temperature Bonding

Sae SHIMIZU, Shota NISHIDA, Jianbo LIANG, Masashi MORIMOTO and Naoteru SHIGEKAWA
Extended Abstracts of 2015 IEEE International Meeting for Future of Electron Devices, Kansai (IMFEDK), pp. 64-65 (2015)

We applied the low-temperature bonding for fabricating base/collector junctions of Si-based bipolar transistor structures. The common-base current gain of fabricated bipolar transistors increased as the ambient temperature was raised up to 165°C, which suggests that the low-temperature bonding might be useful for fabricating high-performance heterojunction devices.

Interface Characteristics of Si/Si Junctions by Using Surface-Activated Bonding

Syoji YAMAJO, Masashi MORIMOTO, Jianbo LIANG and Naoteru SHIGEKAWA
Extended Abstracts of 2015 IEEE International Meeting for Future of Electron Devices, Kansai (IMFEDK), pp. 62-63 (2015)

We investigated the electrical properties of highly-doped n-Si/n-Si and p-Si/p-Si junctions fabricated by using the surface activated bonding. Heights of potential barrier formed at the respective bonding interface were estimated by measuring dependence of their current-voltage characteristics on the ambient temperature. The heights of barrier were found to be varied due to annealing often the bonding process. An analysis using the charge neutral level model suggested that the density of interface states that were likely to be formed during the surface activation process was lowered to $\sim 10^{12} \text{cm}^{-2} \text{eV}^{-1}$ due to the annealing, similarly to results for more heavily doped Si/Si junctions.

Electrical Properties of n⁺-Si/n-GaN Junctions by Room Temperature Bonding

Takuya NISHIMURA, Jianbo LIANG, Naoteru SHIGEKAWA and Noriyuki WATANABE (NTT Laboratories)
Extended Abstracts of 2015 IEEE International Meeting for Future of Electron Devices, Kansai (IMFEDK), pp. 46-47 (2015)

The electrical properties of n⁺-Si/n-GaN junctions by room-temperature bonding were investigated. The n⁺-Si/n-GaN junctions exhibited linear current-voltage characteristics.

Electrical Characterization of GaAs/GaAs Bonding Interfaces

Li CHAI, Jianbo LIANG, Shota NISHIDA, Masashi MORIMOTO and Naoteru SHIGEKAWA
Extended Abstracts of 2015 IEEE International Meeting for Future of Electron Devices, Kansai (IMFEDK), pp. 44-45 (2015)

The electrical properties of GaAs/GaAs junctions fabricated by using surface-activated bonding (SAB) were investigated. We extracted the potential barrier heights at 300-°C-annealed GaAs/GaAs interfaces from their current-voltage characteristics measured at varied ambient temperatures and estimated the energy of charge neutral level E_{CNL} and the density of interface states D_{it} .

Response of Piezoelectric Lead Zirconate Titanate to High-energy Xenon Ion Beam Pulse

Seiji TAKECHI, Yoshinori MIURA, Tomoaki MITSUHASHI, Takashi MIYACHI (Chiba Institute of Technology), Masanori KOBAYASHI (Chiba Institute of Technology), Osamu OKUDAIRA (JAXA), Hiromi SHIBATA (Osaka University), Masayuki FUJII (Famscience), Nagaya OKADA (Honda Electronics), Takeshi MURAKAMI (NIRS) and Yukio UCHIHORI (NIRS)
Jpn. J. Appl. Phys. Vol. 53, pp. 118005-118007 (2014)

To develop a new radiation detector, the characteristics of piezoelectric lead zirconate titanate (PZT) are currently being studied using a 400MeV/n xenon (Xe) beam. In this study, the response of the PZT element to the pulsed beam was investigated by changing the beam intensity. It was found that the time distribution of the Xe ions in the pulse duration must be taken into account to understand the formation of the output signal that appeared on the PZT element.

Present Situation of Plasma Simulation in And in Contact with Liquid

Fumiyoshi TOCHIKUBO and Tatsuru SHIRAFUJI

J. Plasma Fusion Res., Vol. 91, pp. 307-313 (2015) (in Japanese)

This paper describes present situation of plasma simulation in and in contact with liquid, in which we focus on the two topics. The first topic is spatiotemporal evolution of electrical discharges in a gas bubble surrounded with liquid. The second topic is transport and reaction processes at plasma/liquid interface and in liquid. Regarding the second topic, we briefly describes recent research results on the plasma/liquid interface, especially on the fact that pH and concentration of chemical species show extremely steep gradient at the active layer just beneath the liquid surface in contact with plasma.

On the Contribution of Electrons, $\text{Ar}(^3\text{P}_{0,2})$, H_2O^+ , And H_3O^+ to Production of $\text{OH}(\text{A}^2\Sigma^+)$ in a Micro Dielectric Barrier Discharge of Ar/ H_2O

Tatsuru SHIRAFUJI and Tomoyuki MURAKAMI

Jpn. J. Appl. Phys., Vol. 54, 01AC03 (5 pages) (2015)

The numerical simulation of a micro-dielectric barrier discharge of an Ar/ H_2O gas mixture has been performed to understand the behavior of OH (A) in three-dimensionally integrated micro-solution plasma. During the discharge ignition sequence in the period of 0–200 ns, the major OH (A) production reactions are the dissociation of H_2O by high-electron-temperature electrons and metastable excited Ar (^3P). After the main discharge, OH (A) production is dominated by the dissociative recombination of H_3O^+ and low-electron-temperature electrons.

3D Integrated Micro-Solution Plasma for the Treatment of Water - Effects of Discharge Gases -

Ayano NOMURA, Yuta HIMENO, Kenji TANAKA and Tatsuru SHIRAFUJI

Plasma Phys. Technol., Vol. 1, pp. 147-149 (2015)

Methylene blue molecules in aqueous solution have been decomposed by using a novel 3D integrated micro-solution plasma reactor operated with Ar and He gases. Energy efficiency for methylene-blue decomposition in the case of Ar is relatively higher than that in the case of He. This result suggests that cheaper Ar gas has brought about superior performance in water purification. In both cases of Ar and He, methylene-blue decomposition efficiency is one order of magnitude higher than that of conventional solution plasma.

Time-Resolved Optical Emission Spectroscopy on Three-Dimensionally Integrated Micro Solution Plasma in He/ H_2O Mixture

Yuta HIMENO, Yuhei OGURA and Tatsuru SHIRAFUJI

J. Phys. Conf. Ser., Vol. 518, 021021 (6 pages) (2014)

We have performed time-averaged and time-resolved optical emission spectroscopy (OES) on three-dimensionally integrated micro solution plasma (3D IMSP) in He/ H_2O mixture. The results of time-resolved OES on 3D IMSP in He/ H_2O mixture have shown that duration of the optical emission of $\text{OH}(\text{A}^2\Sigma^+ \rightarrow \text{X}^2\Pi$ around 309 nm) is shorter than that in Ar/ H_2O mixture. Possible causes of this difference are discussed by means of difference in the energy of metastable states of Ar and He.

Integrated Multi-Phase-Media Plasma Source

Tatsuru SHIRAFUJI

J. Plasma Fusion Res., Vol. 90, pp. 392-397 (2014) (in Japanese)

This paper describes electrochemical aspects of a plasma/liquid interface, which involves nano-scale electric double layer formed just beneath the liquid surface in contact with plasma. A novel three-dimensionally integrated micro-solution plasma (3D IMSP) is proposed as a method for efficient production of the plasma/liquid interfaces for large scale industrial applications. The process performances of the 3D IMSP are briefly described together with experimental results on the methylene blue degradation and gold nano-particles synthesis

Generation of Micro-Solution Plasmas in Artificial Porous Dielectric Materials Fabricated Using 3D Printer Technology

Tatsuru SHIRAFUJI, Yuhei OGURA, Naoya SOTODA and Kenji TANAKA

Proc. 22nd International Symposium on Plasma Chemistry (ISPC 22), P-I-3-25 (2 pages), Jul. 5-10, Antwerp, Belgium (2015)

We have fabricated a three-dimensionally integrated micro-solution plasma (3D IMSP) reactor using an artificial porous dielectric material using 3D printer technology for generating a large number of microplasmas in contact with a liquid medium. While our previous 3D IMSP reactors are fabricated with

silica pumices which consist of random-size pores, this new 3D IMSP reactor is fabricated with 3D-printed lattice structure in which the same-size pores are arranged regularly. We have successfully obtained microplasmas in this reactor by feeding the gas-liquid mixed medium of Ar and water. Methylene-blue degradation experiments have revealed that pore-size design is very important for achieving higher process performance.

Systematic investigation of effects of exciton–acoustic-phonon scattering on photoluminescence rise times of free excitons in GaAs/Al_{0.3}Ga_{0.7}As single quantum wells

Masaaki NAKAYAMA, Tatsuya OHNO and Yohiaki FURUKAWA

J. Appl. Physics, Vol. 117, 134306 (6 pages) (2015)

We have systematically investigated the photoluminescence (PL) dynamics of free excitons in GaAs/Al_{0.3}Ga_{0.7}As single quantum wells, focusing on the energy relaxation process due to exciton–acoustic-phonon scattering under non-resonant and weak excitation conditions as a function of GaAs-layer thickness from 3.6 to 12.0 nm and temperature from 30 to 50 K. The free exciton characteristics were confirmed by observation that the PL decay time has a linear dependence with temperature. We found that the free exciton PL rise rate, which is the reciprocal of the rise time, is inversely linear with the GaAs-layer thickness and linear with temperature. This is consistent with a reported theoretical study of the exciton–acoustic-phonon scattering rate in the energy relaxation process in quantum wells. Consequently, it is conclusively verified that the PL rise rate is dominated by the exciton-acoustic-phonon scattering rate. In addition, from quantitative analysis of the GaAs-layer thickness and temperature dependences, we suggest that the PL rise rate reflects the number of exciton–acoustic-phonon scattering events.

Photoluminescence observation of electron-hole droplets in a GaAs/AlAs type-II superlattice

Yoshiaki FURUKAWA and Masaaki NAKAYAMA

J. Phys. Conf. Ser., Vol. 619, 012005 (4 pages) (2015)

We have investigated the photoluminescence (PL) properties of a (GaAs)₁₂/(AlAs)₁₂ type-II superlattice (SL) at 10 K from the viewpoint of the formation of electron-hole droplets (EHDs). In the type-II SL, the lowest-energy exciton consists of an X-electron and a Γ -heavy-hole confined in the AlAs and GaAs layers, respectively; namely, the optical transition is indirect in momentum and real space. The excitation-power density was widely changed from ~ 1 mW/cm² to ~ 1 kW/cm² for precisely observing changes of PL spectra. It was found that a broad PL band appears with a threshold-like nature in the energy region lower than the biexciton. This suggests the occurrence of the Mott transition. The prominent feature of the broad PL band is the fact that the spectral profile hardly depends on the excitation-power density, which is one of typical properties of EHDs. From the line-shape analysis of the PL spectra, we estimated the stability energy of the EHD to be ~ 2.9 meV relative to the biexciton energy. The above results consistently demonstrate the formation of the EHD.

Unique properties of photoluminescence excitation spectra in a Eu-doped GaN epitaxial film

Masaaki NAKAYAMA, Satoshi NAKAMURA, Hideo TAKEUCHI, Atsushi KOIZUMI and Yasufumi FUJIWARA

Appl. Phys. Lett., Vol. 106, 012102 (4 pages) (2015)

We have investigated the temperature dependence of photoluminescence-excitation (PLE) spectra of Eu³⁺ emission due to the intra-4f shell transitions in a Eu-doped GaN epitaxial film from the viewpoint of the energy transfer process by carriers and excitons from the host GaN to Eu³⁺ ions. It was found that the excitonic band of the PLE spectrum disappears in a low temperature region below 140 K in spite of the fact that the optical transitions of the A and B excitons are clearly observed in a reflectance spectrum. The excitonic PLE band becomes remarkable with an increase in temperature. This fact indicates that carriers originating from the thermal dissociation of photogenerated excitons contribute to the Eu³⁺ emission. In other words, excitons play no role in the energy transfer process. Furthermore, the PLE spectrum at room temperature exhibits an oscillatory structure resulting from longitudinal-optical phonon emission in a hot carrier relaxation process.

Polariton-condensation effects on photoluminescence properties in a CuBr microcavity

Masaaki NAKAYAMA, Katsuya MURAKAMI, Yoshiaki FURUKAWA and Daegwi KIM

J. Phys. Conf. Ser., Vol. 619, 012015 (4 pages) (2015)

We have investigated the photoluminescence (PL) properties in a CuBr microcavity with HfO₂/SiO₂ distributed Bragg reflectors at 10 K from the viewpoint of cavity-polariton condensation. From the

excitation-power dependence of PL spectra detected at an in-plane wave vector of $k_{\parallel}=0$, we found that the PL characteristics of the lower polariton branch markedly change with a threshold nature: a drastic increase (decrease) in the intensity (band width). In addition, the PL energy exhibits a large blueshift, ~ 10 meV, around the threshold excitation power, reflecting strong polariton-polariton interactions. The blueshifted PL energy is far below the bottom energy of the cavity photon. In addition, the estimated density of photogenerated electron-hole pairs at the threshold excitation power is two orders lower than the Mott-transition density for the formation of electron-hole plasma. The above results consistently demonstrate the occurrence of the cavity-polariton condensation.

Theory of the lifetime of an exciton incoherently created below its resonance frequency by inelastic scattering

Motoaki BAMBA, Shuji WAKAIKI, Hideki ICHIDA, Kohji MIZOGUCHI, Daegwi KIM, Masaaki NAKAYAMA and Yasuo KANEMATSU

Phys. Rev. B, Vol. 91, 235205 (13 pages) (2015)

When an exciton in semiconductor is scattered and its energy is decreased far below the resonance energy of the bare exciton state, it has been considered that an exciton-polariton is created immediately by the scattering process because there is no exciton level at that energy. However, according to the recent time-resolved measurements of P emission originating from inelastic exciton-exciton scattering, it looks rather natural to consider that the exciton-polariton is created in a finite time scale which is restricted by a coherence volume of the exciton after the scattering. In this interpretation, the exciton remains in this time scale far below its resonance energy as a transient state in a series of processes. We propose an expression of the P-emission lifetime depending on the coherence volume of the scattered excitons through the conversion process from them to the polaritons. The coherence volume of the scattered excitons appears in the calculation of the inelastic scattering process on the assumption of a finite coherence volume of the bottleneck excitons. Time-resolved optical-gain measurements could be a way for investigating the validity of our interpretation.

Hydrothermal Synthesis of N-Acetyl-L-cysteine-Capped CuInS₂ Nanoparticles

Hang-Beom BU, Hiroki YOKOTA, Kunio SHIMURA, Kohji TAKAHASHI, Taichi TANIGUCHI and DaeGwi KIM

Chem. Lett., Vol. 44, pp. 200-202 (2015)

CuInS₂ (CIS) nanoparticles (NPs) were hydrothermally prepared by the reaction of Cu²⁺, In²⁺, and Na₂S in the presence of N-acetyl-L-cysteine as a stabilizer. The X-ray diffraction pattern of the resultant CIS NPs indicated that the chalcopyrite NPs could be obtained. The X-ray photoelectron spectroscopy data suggested that Cu²⁺ is reduced to Cu⁺ during the reaction process. The absorption and photoluminescence peaks of the NPs were clearly red-shifted with increasing size of the particles. Our method will aid in the synthesis of other I-III-VI ternary compounds.

Preparation of Highly Luminescent Hybrid Gel Incorporating NAC-Capped CdTe Quantum Dots through Sol-Gel Processing

Hang-Beom BU, Taichi WATANABE, Masayuki HIZUME, Tomomi TAKAGI, Susumu SOBUE, Shoichi KAWAI, Eiichi OKUNO and DaeGwi KIM

Mater. Res. Express, Vol. 2, 036202 (9 pages) (2015)

Highly photoluminescent gel was prepared by embedding water soluble quantum dots (QDs) in an inorganic-organic hybrid gel matrix using a conventional sol-gel process. Aminopropyltrimethoxysilane (APS) and citric acid (CA) were found to be the best combination for the gel preparation. ¹³C-NMR and FT-IR studies indicated hydrogen bond formation between the amine group of APS and the carboxyl group of CA. IR-light radiation curing was comparable to thermal curing and reduced the gelation time to a considerable extent (71%). The resulting composite formed a hybrid gel phosphor with excellent transparency by embedding CdTe QDs into the matrix and emitted light of various colors with high photoluminescence efficiency (40%). The gel phosphor retained the PL properties after storage in air for one year. In addition, the strength of the hybrid phosphor was demonstrated by a coin-flipping test.

Effects of Surface Modification on Photoluminescence Properties of Self-Assembled Monolayer of CdSe Quantum Dots

Taichi WATANABE, Hiroki YOKOTA, Masaaki NAKAYAMA and DaeGwi KIM

J. Phys. Conf. Ser., Vol. 619, 012024 (4 pages) (2015)

We have investigated surface-modification effects on photoluminescence (PL) properties of the self-assembled monolayer of CdSe quantum dots from the viewpoint of the temperature dependence of PL properties. The band-edge PL band is strongly activated by the surface modification and is observed as the main PL band, contrary to the fact that the defect-related PL band is dominant in the as-grown sample. From the analysis of PL decay dynamics, it is demonstrated that the contribution of a bound exciton state to PL processes would suppress a trapping process to defects.

Evidence of Quantum Resonance in Periodically-Ordered Three-Dimensional Superlattice of CdTe Quantum Dots

DaeGwi KIM, Shogo TOMITA, Kazuma OHSHIRO, Taichi WATANABE, Takenobu SAKAI, I-Ya CHANG and KIM Hyeon-Deuk

Nano Lett., Vol. 15, pp. 4343–4347 (2015)

Semiconductor quantum dot (QD) superlattices, which are periodically ordered three-dimensional (3D) array structures of QDs, are expected to exhibit novel photo-optical properties arising from the resonant interactions between adjacent QDs. Since the resonant interactions such as long-range dipole–dipole Coulomb coupling and short-range quantum resonance strongly depend on inter-QD nano space, precise control of the nano space is essential for physical understanding of the superlattice, which includes both of nano and bulk scales. Here, we study the pure quantum resonance in the 3D CdTe QD superlattice deposited by a layer-by-layer assembly of positively charged polyelectrolytes and negatively charged CdTe QDs. From XRD measurements, existence of the periodical ordering of QDs both in the lamination and in-plane directions, that is, the formation of the 3D periodic QD superlattice, was confirmed. The lowest excitation energy decreases exponentially with decreasing the nano space between the CdTe QD layers and also with decreasing the QD size, which is apparently indicative of the quantum resonance between the QDs rather than a dipole–dipole Coulomb coupling. The quantum resonance was also computationally demonstrated and rationalized by the orbital delocalization to neighboring CdTe QDs in the superlattice.

Control of Localized Surface Plasmon Resonance Energy in Monolayer Structures of Gold and Silver Nanoparticles

Hiroki YOKOTA, Taichi TANIGUCHI, Taichi WATANABE and DaeGwi KIM

Phys. Chem. Chem. Phys., Vol. 17, 27077–27081 (2015)

Monolayer structures of Au and Ag nanoparticles (NPs) were fabricated by a dipping method to realize the control of localized surface plasmon resonance (LSPR) energy. The mean inter-particle distance in the monolayer was controlled by changing the concentration of NPs in the colloidal solution used for monolayer assembly. The extinction-peak energy of the monolayer structure was red-shifted with decreasing inter-particle distance, reflecting plasmon coupling between NPs.

Domain Wall in Multimode Peierls State

Yuki MATSUMOTO and Akira TERAJ

J. Phys. Soc. Jpn., Vol. 83, 114705 (9 pages) (2014)

The domain wall as a one-dimensional discommensuration of the multimode Peierls (MMP) lattice distortion is investigated numerically based on the Su–Schrieffer–Heeger model generalized to the square lattice with the half-filled electronic band. In order to create the domain wall, we consider a spin excitation where the total number of spin-up electrons is larger than that of spin-down electrons by the linear dimension of the square lattice. The extra spins are localized at the domain wall, and the localized wave functions form a mid-gap band with zero energy. The localized wave functions are analytically constructed in the same way as the edge states in the graphene nanoribbon. The properties of the localized states for the domain walls with various orientations to the MMP distortion pattern are elucidated. The number of the zero-energy states for every orientation satisfies the index theorem established in the Dirac electron system. Furthermore, the correlation effects on the domain wall are studied by introducing the on-site and nearest-neighbor Coulomb interactions to the electron–lattice model. It is revealed that the creation energy of the domain wall decreases due to the electron–electron interactions.

Fractionally Charged Solitons in “1100” Charge Order Backgrounds

Kenichi HIROKAWA, Akira TERAJ and Yoshiyuki Ono

J. Phys. Soc. Jpn. Vol. 84, 034707 (7 pages) (2015)

We reconsider the problem of “binding” of a pair of fractionally charged solitons in “1100” charge order backgrounds, using the variational Monte Carlo method based on the matrix-product state. In the “1100”

charge order ground state of the one-dimensional extended Peierls–Hubbard model, the $2k_F$ bond order wave (BOW) coexists with the $4k_F$ BOW. We have found that the fractionally charged soliton with $-e/2$, $-e$ being an electronic charge, is accompanied with not only a kink in the $2k_F$ BOW but also a kink in the $4k_F$ BOW, which was not allowed to exist in the dimer model used in the previous study. Calculating the total energy of a pair of fractionally charged solitons with the same charge as a function of the soliton–soliton distance, we have found that the soliton–soliton interaction is repulsive. Therefore the “binding” of the solitons does not occur and the elementary charge excitation from the “1100” charge order ground state is a fractionally charged soliton.

A Perturbative Method for Nonequilibrium Steady State of Open Quantum Systems

Tatsuro YUGE and Ayumu SUGITA

J. Phys. Soc. Jpn. Vol. 84, 014001 (7 Pages) (2015)

We develop a method of calculating the nonequilibrium steady state (NESS) of an open quantum system that is weakly coupled to reservoirs in different equilibrium states. We describe the system using a Redfield-type quantum master equation (QME). We decompose the Redfield QME into a Lindblad-type QME and the remaining part R . Regarding the steady state of the Lindblad QME as the unperturbed solution, we perform a perturbative calculation with respect to R to obtain the NESS of the Redfield QME. The NESS thus determined is exact up to the first order in the system-reservoir coupling strength (pump/loss rate), which is the same as the order of validity of the QME. An advantage of the proposed method in numerical computation is its applicability to systems larger than those in methods of directly solving the original Redfield QME. We apply the method to a noninteracting fermion system to obtain an analytical expression of the NESS density matrix. We also numerically demonstrate the method in a nonequilibrium quantum spin chain.

Volumetric display using rotating prism sheets arranged in a symmetrical configuration

Yuki MAEDA, Daisuke MIYAZAKI, Takaaki MUKAI and Satoshi MAEKAWA (Univ. of Hyogo)

Opt. Express Vol.21, 27074-27086 (2013).

A volumetric display that creates a distortion-free three-dimensional (3D) image in midair is described. The proposed system consists of rotating prism sheets used as an optical scanner and a dihedral corner reflector array (DCRA), which is a distortion-free imaging element. Two prism sheets are arranged in a symmetrical configuration to reduce an unnatural motion parallax caused by optical aberrations. A cross-section of the 3D image is formed by the DCRA in midair and moved by the rotating prism sheets to create a 3D displayable space. A 3D volume image was displayed without image distortion or unnatural motion parallax.

Floating multi-view image formation with micro-mirror array imaging element

Daisuke MIYAZAKI

The 3rd Japan-Korea Workshop on Digital Holography and Information Photonics, Session 2- 3 (2013).

A volumetric display that creates a distortion-free three-dimensional (3D) image in midair is described. The proposed system consists of rotating prism sheets used as an optical scanner and a dihedral corner reflector array (DCRA), which is a distortion-free imaging element. Two prism sheets are arranged in a symmetrical configuration to reduce an unnatural motion parallax caused by optical aberrations. A cross-section of the 3D image is formed by the DCRA in midair and moved by the rotating prism sheets to create a 3D displayable space. A 3D volume image was displayed without image distortion or unnatural motion parallax.

Floating volumetric display using an imaging element that consists of a 90° prism sheet and a linear Fresnel lens

Yuki MAEDA, Daisuke MIYAZAKI, Takaaki MUKAI and Satoshi MAEKAWA (Univ. of Hyogo)

Proc. Soc. Photo-Opt. Instrum. Eng., Vol. 9011, 90111N (2014).

We propose a floating volumetric display system using a novel imaging element whose aperture is large and can be made easily at low cost. Diffuse rays in a horizontal direction for an observer are formed by a 90° prism sheet, which has a shape of an array of 90° V-grooves, as a result of twice total internal reflection. On the other hand, the diffuse rays in a longitudinal direction for the observer are formed by a linear Fresnel lens. A formed image by the proposed imaging element does not distort in the horizontal direction because the rays in the horizontal direction converge by retroreflection. The proposed imaging element can be produced easier than a conventional distortion-free imaging element and display a larger floating image. A floating three-dimensional image was displayed by a volumetric display system based on optical scanning of an inclined image plane. A position of a two-dimensional real image formed by the proposed imaging element was moved by an optical scanner at a faster rate than the duration time of persistence of vision. A stack of moved images created the floating three-dimensional volume image.

Multi-user autostereoscopic display based on direction-controlled illumination using a slanted cylindrical lens array

Daisuke MIYAZAKI, Yui HASHIMOTO, Takahiro TOYOTA, Kenta OKODA, Tetsuro OKUYAMA (Panasonic), Toshikazu OHTSUKI (Panasonic), Akio NISHIMURA (Panasonic), and Hiroyuki YOSHIDA (Panasonic)

Proc. Soc. Photo-Opt. Instrum. Eng., Vol. 9011, 90111G (2014).

This research aims to develop an auto-stereoscopic display, which satisfies the conditions required for practical use, such as, high resolution and large image size comparable to ordinary display devices for television, arbitrary viewing position, multiple viewer availability, suppression of nonuniform luminance distribution, and compact system configuration. In the proposed system, an image display unit is illuminated with a direction-controlled illumination unit, which consists of a spatially modulated parallel light source and a steering optical system. The steering optical system is constructed with a slanted cylindrical array and vertical diffusers. The direction-controlled illumination unit can control output position and horizontal angle of vertically diffused light. The light from the image display unit is controlled to form narrow exit pupil. A

viewer can watch the image only when an eye is located at the exit pupil. Auto-stereoscopic view can be achieved by alternately switching the position of an exit pupil at viewer's both eyes, and alternately displaying parallax images. An experimental system was constructed to verify the proposed method. The experimental system consists of a LCD projector and Fresnel lenses for the direction-controlled illumination unit, and a 32 inch full-HD LCD for image display.

Optical design for heterogeneous imaging based on retro reflection using parallel roof mirror arrays

Yuki MAEDA, Daisuke MIYAZAKI, and Satoshi. MAEKAWA (Univ. of Hyogo)

JSAP-OSA Joint Symposia 2014, Information Photonics, 20a-C4-3 (2014).

Floated integral imaging display viewable from surrounding area

Daisuke MIYAZAKI, Go MIYAZAKI, Yuki MAEDA, and Takaaki MUKAI

Imaging and Applied Optics 2014, OSA Technical Digest, DW2B.5 (2014).

A full-parallax auto-stereoscopic display method that enables formation of a floating three-dimensional image viewable from a surrounding area is proposed. This method utilizes integral imaging, a rotating mirror scanner, and a hemisphere concave mirror.

Wide-Viewing Angle Three-dimensional Display Using Multiple LCDs

Hirofumi YABU, Joji KANDA, and Hideya TAKAHASHI

ICIC Express Letters Part B, Vol.5, 1, pp.195-200 (2014).

We propose an omnidirectional three-dimensional (3D) display system. This is a tool for communication around a 3D image among a small number of people. This 3D display system consists of multiple basic 3D display units. The basic unit consists of an LCD, a lenticular lens array sheet, and a relay lens. In this basic unit, the light rays from an LCD pass through a lenticular lens sheet and observed directly. Thus, the spatial density distribution of projected light rays is partial. To average the spatial density of projected light rays, we use a relay lens. To increase the viewing angle, we aligned multiple basic units in a circle, and displayed 3D images at the center of the circle. To verify the effectiveness of the proposed 3D display, we constructed the prototype system. This prototype consists of 3 basic units. They are aligned 18.5-degree apart in a circle and the radius is 613.2 mm. The shape of the maximum size of displayed 3D images is a cylinder and the radius is 25 mm, the height is 50 mm. The viewing angle of a 3D image is 55.5-degree. This paper describes the principle of proposed 3D display system, and also describes the experimental results.

Silicone Rubber Membrane Tactile Sensor for Endoscope Based on Image Processing

Yuma KITANOUMA, Hideya TAKAHASHI, Kayo YOSHIMOTO (Osaka University), and Kenji YAMADA (Osaka University)

ICIC Express Letters Part B, Vol.5, 1, pp.279-284 (2014).

We propose the silicone rubber membrane tactile sensor for an endoscope. The proposed system consists of the transparency silicon rubber membrane and the image sensor. Our proposed system can estimate the stiffness of the target object by measuring the deformation of the silicone rubber which includes markers inside. When the silicone rubber is deformed by contacting with the target object, the position of each marker shifts. By using the displacement information of markers measured by the imaging device, the system can measure the deformation of the silicone rubber. The purpose of this study is to evaluate the proposed system. At first, we introduce the approximated models of the silicone and the object. We formulate the stiffness of the object, the deformation of silicone, and the whole object. To verify the effectiveness of the proposed system, we constructed the prototype system.

Retinal projection type super multi-view head-mounted display

Hideya TAKAHASHI, Yutaka ITO, Seigo NAKATA, and Kenji YAMADA (Osaka University)

Proc.SPIE-IS&T Electronic Imaging, Vol.9012, pp. 90120L-1-90120L-6 (2014).

We propose a retinal projection type super multi-view head-mounted display (HMD). The smooth motion parallax provided by the super multi-view technique enables a precise superposition of virtual 3D images on the real scene. Moreover, if a viewer focuses one's eyes on the displayed 3D image, the stimulus for the accommodation of the human eye is produced naturally. Therefore, although proposed HMD is a monocular HMD, it provides observers with natural 3D images. The proposed HMD consists of an image projection

optical system and a holographic optical element (HOE). The HOE is used as a combiner, and also works as a condenser lens to implement the Maxwellian view. Some parallax images are projected onto the HOE, and converged on the pupil, and then projected onto the retina. In order to verify the effectiveness of the proposed HMD, we constructed the prototype HMD. In the prototype HMD, the number of parallax images and the number of convergent points on the pupil is three. The distance between adjacent convergent points is 2 mm. We displayed virtual images at the distance from 20 cm to 200 cm in front of the pupil, and confirmed the accommodation. This paper describes the principle of proposed HMD, and also describes the experimental result.

Evaluation of the three-dimensional endoscope system for assessing the gastrointestinal motility

Kayo YOSHIMOTO (Osaka University), Kenji YAMADA (Osaka University), Kenji WATABE (Osaka University), Maki TAKEDA (Osaka University), Takahiro NISHIMURA (Osaka University), Michiko KIDO (Osaka University), Toshiaki Nagakura (Osaka Electro-Communication University), Hideya TAKAHASHI, Tsutomu NISHIDA (Osaka University), Hideki IJIMA (Osaka University), Masahiko TSUJII (Osaka University), Tetsuo TAKEHARA (Osaka University), and Yuko OHNO (Osaka University) *Proc.SPIE-BiOS2014 Advanced Biomedical and Clinical Diagnostic System XII*, Vol.8935, pp. 89351G-1-89351G -6 (2014).

This paper described evaluation of the three-dimensional endoscope system for assessing the gastrointestinal motility. Gastrointestinal diseases are mainly based on the morphological or anatomical abnormality. However, sometimes the gastrointestinal symptoms are apparent without visible abnormalities. Such diseases are called functional gastrointestinal disorder, for example, functional dyspepsia, and irritable bowel syndrome. One of the major factors of these diseases is the gastrointestinal dysmotility. Assessment procedures for motor function are either invasive, or indirect. We thus propose a three-dimensional endoscope system for assessing the gastrointestinal motility. To assess the dynamic motility of the stomach, three-dimensional endoscopic imaging of stomach lining is performed. Propagating contraction waves are detected by subtracting estimated stomach geometry without contraction waves from one with contraction waves. After detecting constriction waves, their frequency, amplitude, and speed of propagation can be calculated. In this study, we evaluate the proposed system. First, we evaluate the developed three-dimensional endoscope system by a flat plane. This system can measure the geometry of the flat plane with an error of less than 10 percent of the distance between endoscope tip and the object. Then we confirm the validity of a prototype system by a wave simulated model. The detected wave is approximated by a Gaussian function. In the experiment, the amplitude and position of the wave can be measure with 1 mm accuracy. These results suggest that the proposed system can measure the speed and amplitude of contraction. In the future, we evaluate the proposed system in vivo experiments.

Gastric contraction imaging system using a three-dimensional endoscope

Kayo YOSHIMOTO (Osaka University), Kenji YAMADA (Osaka University), Kenji WATABE (Osaka University), Maki TAKEDA (Osaka University), Takahiro NISHIMURA (Osaka University), Michiko KIDO (Osaka University), Toshiaki Nagakura (Osaka Electro-Communication University), Hideya TAKAHASHI, Tsutomu NISHIDA (Osaka University), Hideki IJIMA (Osaka University), Masahiko TSUJII (Osaka University), Tetsuo TAKEHARA (Osaka University), and Yuko OHNO (Osaka University) *IEEE Journal of Translational Engineering in Health and Medicine*, Vol.2, 1, pp.1-8 (2014).

Objective: This paper presents a gastric contraction imaging system for assessment of gastric motility using a three-dimensional endoscope. Gastrointestinal diseases are mainly based on morphological abnormalities. However, gastrointestinal symptoms are sometimes apparent without visible abnormalities. One of the major factors for these diseases is abnormal gastrointestinal motility. For assessment of gastric motility, a gastric motility imaging system is needed. Method: To assess the dynamic motility of the stomach, the proposed system measures three-dimensional gastric contractions derived from a three-dimensional profile of the stomach wall obtained with a developed three-dimensional endoscope. After obtaining contraction waves, their frequency, amplitude, and speed of propagation can be calculated using a Gaussian function. Results: The proposed system was evaluated for three-dimensional measurements of several objects with known geometries. The results showed that the surface profiles could be obtained with an error of less than 10 percent of the distance between two different points on images. Subsequently, we evaluated the validity of a prototype system using a wave simulated model. In the experiment, the amplitude and position of waves

could be measured with 1-mm accuracy. Conclusions: The present results suggest that the proposed system can measure the speed and amplitude of contractions. Clinical Impact: This system has low invasiveness and can assess the motility of the stomach wall directly in a three-dimensional manner. Our method can be used for examination of gastric morphological and functional abnormalities.

Applied Chemistry and Bioengineering

High Catalytic Activity of Heteropolynuclear Cyanide Complexes Containing Co and Pt Ions for Visible-Light Driven Water Oxidation

Yusuke YAMADA, Kohei OYAMA, Rachel GATES and Shunichi FUKUZUMI

Angew. Chem. Int. Ed., Vol. 54, pp. 5613-5617 (2015)

A near-stoichiometric amount of O₂ was evolved as observed in the visible-light irradiation of an aqueous buffer (pH 8) containing [Ru^{II}(2,2'-bipyridine)₃] as a photosensitizer, Na₂S₂O₈ as a sacrificial electron acceptor, and a heteropolynuclear cyanide complex as a water-oxidation catalyst. The heteropolynuclear cyanide complexes exhibited higher catalytic activity than a polynuclear cyanide complex containing only Co^{III} or Pt^{IV} ions as C-bound metal ions. The origin of the synergistic effect between Co and Pt ions is discussed in relation to electronic and local atomic structures of the complexes.

High and Robust Performance of H₂O₂ Fuel Cells in the Presence of Scandium Ion

Yusuke YAMADA, Masaki YONEDA and Shunichi FUKUZUMI

Energy Environ. Sci., Vol. 8, pp. 1698-1701 (2015)

Hydrogen peroxide is a promising candidate as a next-generation energy carrier because it can be produced from O₂ abundant in air using photoenergy in the presence of a photocatalyst and can also generate electricity via fuel cells. Although H₂O₂ is unstable during storage under ambient conditions, we report herein remarkable suppression of H₂O₂ decomposition by adding Sc³⁺ ion to an aqueous H₂O₂ solution. The resulting solution yields high and robust performance of one-compartment H₂O₂ fuel cells in terms of open circuit potentials, power densities, and durability.

Bottom Up and Top Down Methods to Improve Catalytic Reactivity for Photocatalytic Production of Hydrogen Peroxide from Water and Dioxygen with a Ruthenium Complex and Water Oxidation Catalysts

Yusuke ISAKA, Satoshi KATO, Dachao HONG, Tomoyoshi SUENOBU, Yusuke YAMADA and Shunichi FUKUZUMI

J. Mater. Chem. A, Vol. 3, pp. 12404-12412 (2015)

Hydrogen peroxide (H₂O₂) was produced from water and dioxygen using [Ru^{II}(Me₂phen)₃]²⁺ (Me₂phen = 4,7-dimethyl-1,10-phenanthroline) as a photocatalyst and [Ir(Cp*)(H₂O)₃]²⁺ (Cp* = η⁵-pentamethylcyclopentadienyl) as a precursor of a water oxidation catalyst in the presence of Sc³⁺ in water under visible light irradiation. TEM and XPS measurements of residues in the resulting solution after the photocatalytic production of H₂O₂ indicated that [Ir(Cp*)(H₂O)₃]²⁺ was converted to Ir(OH)₃ nanoparticles, which are actual catalytic species. The Ir(OH)₃ nanoparticles produced in situ during the photocatalytic production of H₂O₂ were smaller in size than those prepared independently from hydrogen hexachloroiridate (H₂IrCl₆), and exhibited higher catalytic reactivity for the photocatalytic production of H₂O₂. The photocatalytic production of H₂O₂ from water and dioxygen was also made possible when Ir(OH)₃ nanoparticles were replaced by nickel ferrite (NiFe₂O₄) nanoparticles, which are composed of more earth abundant metals than iridium. The size of NiFe₂O₄ nanoparticles became smaller during the photocatalytic production of H₂O₂ to exhibit higher catalytic reactivity in the second run as compared with that in the first run. NiFe₂O₄ nanoparticles obtained by the treatment of NiFe₂O₄ in an aqueous solution of Sc³⁺ exhibited 33-times higher catalytic reactivity in H₂O₂-production rates than the as-prepared NiFe₂O₄. Thus, both the bottom-up method starting from a molecular complex [Ir(Cp*)(H₂O)₃]²⁺ and the top-down method starting from as-prepared NiFe₂O₄ to obtain nanoparticles with smaller size resulted in the improvement of the catalytic reactivity for the photocatalytic production of H₂O₂ from water and dioxygen.

Singlet Oxygen Generation from Li⁺@C₆₀ Nano-Aggregates Dispersed by Laser Irradiation in Aqueous Solution

Kei OHKUBO, Naoki KOHNO, Yusuke YAMADA and Shunichi FUKUZUMI

Chem. Commun., Vol. 51, pp. 8082-8085 (2015)

Laser pulse irradiation of a deaerated aqueous solution containing the solid state lithium ion-encapsulated fullerene resulted in the formation of highly dispersed nano-aggregates ($\text{Li}^+@C_{60}$)_n. Photoirradiation of an O₂-saturated D₂O solution containing ($\text{Li}^+@C_{60}$)_n gave singlet oxygen with 55% quantum yield, leading to efficient double-stranded DNA cleavage.

Ni–Cu Alloy Nanoparticles Loaded on Various Metal Oxides Acting as Efficient Catalysts for Photocatalytic H₂ Evolution

Yusuke YAMADA, Shinya SHIKANO and Shunichi FUKUZUMI

RSC Adv., Vol. 5, pp. 44912-44919 (2015)

Catalysis of Al₂O₃–SiO₂, TiO₂, SiO₂ and CeO₂ (MOx) impregnated with pre-formed Ni–Cu alloy nanoparticles (Ni–CuNPs/MOx) for photocatalytic hydrogen (H₂) evolution was compared with that of MOx impregnated with Ni²⁺ and Cu²⁺ ions followed by calcination and reduction (Ni–Cu/MOx). The photocatalytic H₂ evolution was conducted by photoirradiation ($\lambda > 340$ nm) of a deaerated mixed solution of a phthalate buffer (pH 4.5) and acetonitrile [1:1 (v/v)] containing β -dihydronicotinamide adenine dinucleotide (NADH), 2-phenyl-4-(1-naphthyl)quinolinium ion (QuPh⁺–NA), and Ni–CuNPs/MOx or Ni–Cu/MOx as an electron donor, a photosensitizer and an H₂-evolution catalyst, respectively. Ni–CuNPs/Al₂O₃–SiO₂ exhibited activity for the photocatalytic H₂ evolution, whereas Ni–Cu/Al₂O₃–SiO₂ showed no activity. Such precursor dependent catalysis can be elucidated by the ion-exchangeable nature and high surface area of Al₂O₃–SiO₂, on which Ni–Cu alloy particles hardly form from metal salts. On the other hand, Ni–Cu/TiO₂ and Ni–Cu/SiO₂ exhibited higher activity than Ni–CuNPs/TiO₂ and Ni–CuNPs/SiO₂, respectively, resulting from formation of smaller Ni–Cu alloy nanoparticles on TiO₂ and SiO₂ by reducing Ni²⁺ and Cu²⁺ on the surfaces. When CeO₂ was used as the support, no catalytic activity was observed for either Ni–CuNPs/CeO₂ or Ni–Cu/CeO₂. Kinetic study for thermal H₂ evolution suggested that Ni–CuNPs were severely deactivated for H₂ evolution by being loaded on CeO₂.

Characterization of Lithium Insertion Electrodes and Its Verification: Prototype 18650 Batteries Consisting of LTO and LAMO

Kensuke NAKURA, Kingo ARIYOSHI, Hiroshi YOSHIKAWA and Tsutomu OHZUKU

J. Electrochem. Soc., Vol. 162, pp. A622-A628 (2015)

The insertion electrodes of lithium titanium oxide (LTO) and lithium aluminum manganese oxide (LAMO) are characterized in terms of the area-specific capacity (ASC) in mAh cm⁻², area-specific impedance (ASI) in Ω cm², and area-specific deformation (ASD) in $\mu\text{m}/(\text{mAh cm}^{-2})$. The prototype 18650-batteries consisting of LTO and LAMO electrodes characterized in this way are fabricated and examined in their performance in order to verify the basic concepts of the characterization of the lithium insertion electrodes. The rechargeable capacity, 1.05 Ah, calculated from ASC and the active electrode area agrees with the nominal capacity of 1.0 Ah determined at the 5-h rate of discharge. The impedance estimated from ASI and the active electrode area also agrees well with the observed impedance spectra for a prototype battery except a high frequency region due to inductance derived from a spirally wounded electrode configuration. The internal resistance of the battery is calculated to be ca. 30 m Ω from the results on the rate capability tests at 1/5, 1/2, 1, 2, 3, 4, and 5 C-rate for both charge and discharge, and an understanding on the internal resistance of a battery is discussed in relation to ASI and ASD.

Secondary Excitation Process for Quantitative Confocal 3D-XRF Analysis

Kouichi TSUJI, Atsushi TABE, Peter WOBRAUSCHECK and Christina STRELI

Advances in X-ray Analysis, Vol.58, pp. 191-199 (2015)

X-ray fluorescence (XRF) is a well-established method for quantitative elemental analysis. For accurate quantification, secondary excitation has to be taken into account. In this paper, the secondary excitation process was discussed for analysis by confocal micro-XRF. Experimental depth profiles were shown for a layered sample of Co and Cu. An additional peak was observed in the depth profile of Co, and it was explained by secondary excitation process. Additionally, a Mosaic model was proposed for quantification of confocal micro-XRF analysis.

Confocal Micro-XRF Analysis of Light Elements with Rh X-Ray Tube and Its Application for Painted Steel Sheet

Ryota YAGI and Kouichi TSUJI

X-Ray Spectrom., Vol.44, pp. 186-189 (2015)

A confocal micro-X-ray fluorescence (XRF) instrument with a vacuum chamber was applied for analysis of light elements for painted steel sheet. Because this instrument is equipped with a Rh-anode X-ray tube, light elements are excited more effectively by the Rh-L lines. However, it was difficult to analyze Cl, because the energies of the Cl-K lines are close to those of the Rh-L lines. Thus, we applied an Al thin film as a primary X-ray filter to eliminate the Rh-L lines and confirmed the feasibility of Cl analysis using a Rh X-ray tube. Rh-L scattered X-rays were observed by using an acrylic plate as a sample. The Rh-L scattered X-rays were completely absorbed by a 24 μm thick Al filter. A calibration curve of Cl was prepared by using certified reference materials with different Cl concentrations. The limit of detection for Cl was 11.9 ppm as estimated from the calibration curve. Confocal micro-XRF with a Rh X-ray tube enables the analysis of low Z elements including Cl by applying an Al filter. This technique was applied for a practical painted steel sheet sample. The elemental image of Cl was successfully observed after corrosion in NaCl solution as well as other light elemental maps.

Confocal Micro XRF Monitoring of Displacement Plating Process

Yuta KITADO, Shintaro HIRANO, Noritsugu KOMETANI and Kouichi TSUJI

Adv. X-ray. Chem. Anal., Japan, Vol. 46, pp.269-276 (2015) (in Japanese)

X-ray fluorescence analysis (XRF) is a non-destructive method. There is a lot of applications like analysis of industrial material. By assembling the polycapillary X-ray lens (PCXL) in the point part of X ray tube and a detector, the micro-area analysis has been possible. The depth resolution of the confocal micro XRF instrument which had been developed in our laboratory is about 44 μm at the confocal point at Au $L\beta$ (11.4 keV). The confocal micro XRF instrument was applied to in situ analysis of displacement plating process. Time dependent profiles were acquired by repeated point analysis on the surface of the steel sheet and repeated line scan near a solidliquid interface. Inhomogeneous nature of displacement plating was observed by 2D mapping of the steel sheet after the chemical reaction.

On X-Ray Channeling in a Vibrating Capillary

Andrea LIEDL, Sultan B. DABAGOV, Dariush HAMPAL, Claudia POLESE and Kouichi TSUJI

Nucl. Instrum. Methods Phys. Res., B, Vol. 355, pp. 289-292 (2015)

A novel study on a different use of polycapillary optics is presented. The scope of this study is to achieve an efficient radiation collimation due to handled beam profiling that avoids the typical one based on total external reflection into the capillary channel. For this purpose a vibration is applied to a monicapillary in order to emulate a “virtual roughness” on the channel internal wall surface. The transmission properties of such a system for different vibrational states are discussed.

Preliminary Experiment of X-Ray Diffraction Imaging

Masaki YAMANASHI, Noritsugu KOMETANI and Kouichi TSUJI

Nucl. Instrum. Methods Phys. Res., Sect. B, Vol. 355 pp. 272–275 (2015)

X-ray diffraction (XRD) techniques have been used in various fields, such as, material science, medical science, etc. XRD gives the structure information of materials. An XRD imaging spectrometer equipped with a 2D X-ray detector for obtaining the information of a large observation area was developed in this study. A polycapillary half lens was applied as a 2D collimator to have an X-rays with a large collimated area of 8 mm. The 2D diffracted X-rays were detected by a 2D X-ray detector.

Analytical Technique for Monitoring Trace Heavy Elements Eluted from Surface of Toys

Kouichi Tsuji

In *Trace analysis of metals and sample preparation techniques*, Technical Information Institute Co., Ltd. pp. 423-429 (2015) (in Japanese)

Total reflection X-ray fluorescence (TXRF) is well known as a trace analysis method. There are many applications of trace elemental analysis by TXRF. Sample preparation technique has been developed depending on the type of the samples to be analyzed. In the case of solution samples, a normal sample preparation is to drop a small amount of solution on a flat sample carrier, then a dried residue is measured by TXRF. We have studied how to measure the metals in surface layers of plastics by TXRF. In some cases, the

surface of the plastic products will be dissolved by acid solutions such as acid rain, leading that harmful elements are also dissolved into the solutions or soils. In this study, we have studied dissolving and leaching processes of plastic products for TXRF analysis. A droplet of solutions dissolved by organic solutions was prepared in thin films by spin coating techniques. This sample was analyzed by TXRF with an internal standard solution. In addition, a actual plastic toy (minicar) was dissolved in acid solution. The leaching solution was sampled in the time range from 0.5 min. to 180 min., then they were measured by TXRF. The time-dependent curves of TXRF intensities showed specific shapes depending on the elements. This result indicates that TXRF is useful for monitoring the leaching process of metals from plastic toys.

Determination of Trace Elements in Italian Wines by Means of Total Reflection X-Ray Fluorescence Spectroscopy

Rogerta DALIPI, Laura BORGESSE, Annalisa ZACCO, Kouichi TSUJI, Emanuele SANGIORGI, Roberto PIRO, Elza BONTEMPI and Laura E. DEPERO

Intern. J. Environ. Anal. Chem., in press (DOI:10.1080/03067319.2015.1036861)

This work was performed to highlight the advantages of total reflection X-ray fluorescence spectroscopy (TXRF) for multi-elemental qualitative and quantitative analysis of wine. Indeed the International Organization of Vine and Wine (OIV) selected some potentially toxic elements and proposed limit values for their concentration in wines. Direct TXRF analysis of nine wine samples from Emilia Romagna region of Italy was performed in two different laboratories: Italy and Japan. Wine dehydration was also evaluated as sample conservation mean. Traces of Fe, Cu, Zn and Pb are present in all the analysed samples, with concentrations lower than the limits established by the OIV. The target hazard quotients (THQs) were also calculated for seven elements (Cl, Mn, Fe, Ni, Cu, Zn and Sr) to determine their potential detrimental effects. The results show that TXRF is a fast, simple and accurate analytical technique for trace element analysis of wine. Moreover, dehydration is an effective way to store wine samples for further elemental analysis.

Secondary Excitation Process for Quantitative Confocal 3D-XRF Analysis

Kouichi TSUJI, Atsushi TABE, Peter WOBRAUSCHECK and Christina STRELI

Powder Diffraction, Vol. 30, pp. 109-112 (2015)

X-ray fluorescence (XRF) is a well-established method for quantitative elemental analysis. For accurate quantification, secondary excitation has to be taken into account. In this paper, the secondary excitation process was discussed for analysis by confocal micro-XRF. Experimental depth profiles were shown for a layered sample of Co and Cu. An additional peak was observed in the depth profile of Co, and it was explained by secondary excitation process. Additionally, a Mosaic model was proposed for quantification of confocal micro-XRF analysis.

Analytical Characteristics of Wavelength Dispersive XRF Imaging with Straight Polycapillary and 2D Detector

Seiji EMOTO, Kouichi TSUJI, Shuichi KATO, Takashi YAMADA and Takashi SHOJI

Advances in X-Ray Chemical Analysis, Japan, Vol.45, pp.129-138 (2014) (in Japanese)

XRF imaging is analytical method to obtain 2D elemental distribution by using XRF. One of the typical methods of XRF imaging is scanning XRF imaging using micro X-ray beam. For this method, energy dispersive detector is used. However, in energy dispersive scanning XRF imaging, since the sample is scanned with a fixed micro X-ray beam, this method needs long measurement time to obtain elemental images of a wide area. The alternative method for performing XRF imaging in a shorter time is a projection XRF imaging. For this method, incident X-ray is irradiated to a sample in a wide area and fluorescence X-ray is detected by 2D detector. However, since 2D detector has no energy resolution, there is a problem that the identification of the elements can not be performed. Therefore, we proposed the projection XRF imaging combined with wavelength dispersive spectroscopy (WDS). In this paper, we discuss WD-XRF imaging using straight polycapillary and X-ray CCD camera.

3D-XRF Analysis of Electrodes of Li-ion Battery

Ryota YAGI, Shintaro HIRANO, Kouichi TSUJI, Mareike FALK, Jurgen JANEK and Ursula FITTSCHEN

Advances in X-Ray Chemical Analysis, Japan, Vol.45, pp.241-250 (2014) (in Japanese)

X-ray fluorescence analysis (XRF) is a non-destructive method. Using polycapillary X-ray lens (PCXL), the

micro-area analysis has been possible. In confocal setup, foci of both X-ray focusing PCXL and collecting PCXL are adjusted to the identical point, therefore depth elemental profiling and three dimensional elemental analysis are possible by scanning sample in three dimensions. In our laboratory, confocal 3D micro-XRF instrument which provides a vacuum chamber was developed. Under vacuum condition, it becomes possible to detect soft X-rays from light elements because of the absence of atmosphere which absorb soft X-rays. The depth resolution of the confocal 3D-XRF instrument which had been developed in our laboratory is about 11 μm at the confocal point at Mo-K α (17.4 keV). The confocal 3D-XRF instruments were applied to analysis the electrode materials of Li-ion secondary battery under atmospheric and vacuum conditions. Depth-dependent elemental mapping was performed for a positive-electrode material, which consists of $\text{LiMn}_{1.5}\text{Ni}_{0.5}\text{O}_4$, after charge-discharge processes. On the negative electrode material (graphite), Ni and Mn were observed.

Visualization of Elemental Distributions near Steel Sample Surface by Confocal Micro X-Ray Fluorescence

Kouichi TSUJI, Shintaro HIRANO, Ryota YAGI, Takashi NAKAZAWA, Koji AKIOKA, Masahiro ARAI and Takashi DOI

Tetsu-to-Hagané, Vol. 100, pp.897-904 (2014) (in Japanese)

Details of corrosion process under the coating layer of the steel sheet have not been understood well. Therefore, it is required to develop a nondestructive analytical method for the near surface of the steel sheet. It is also required to have analytical tool for observing the corrosion process in the solution. The authors developed a confocal 3D-XRF analytical instrument, which enables a nondestructive elemental analysis near the surface of the material. This technique was applied for analyzing the corrosion process under the coating layer of the steel sheet. Depth elemental images showing elemental distributions were nondestructively obtained. 3D-XRF method was also applied for observing Fe distribution in the NaCl solution during corrosion of Fe from the steel sheet. Dissolution, migration, and deposition processes were successfully monitored. It is expected that this confocal 3D-XRF technique will be applied for in-situ analysis of the steels under various environments.

Comparison of Two Confocal Micro-XRF Spectrometers with Different Design Aspects

Stephan SMOLEK, Takashi NAKAZAWA, Atsushi TABE, Kazuhiko NAKANO, Kouichi TSUJI, Christina STRELI and Peter WOBRAUSCHEK

X-Ray Spectrom., Vol. 43, pp. 93-101 (2014)

Two different confocal micro X-ray fluorescence spectrometers have been developed and installed at Osaka City University and the Vienna University of Technology Atominstitut. The Osaka City University system is a high resolution spectrometer operating in air. The Vienna University of Technology Atominstitut spectrometer has a lower spatial resolution but is optimized for light element detection and operates under vacuum condition. The performance of both spectrometers was compared. In order to characterize the spatial resolution, a set of nine specially prepared single element thin film reference samples (500nm in thickness, Al, Ti, Cr, Fe, Ni, Cu, Zr, Mo, and Au) was used. Lower limits of detection were determined using the National Institute of Standards and Technology standard reference material glass standard 1412. A paint layer sample (cultural heritage application) and paint on automotive steel samples were analyzed with both instruments. The depth profile information was acquired by scanning the sample perpendicular to the surface.

Elemental Depth Imaging of Solutions for Monitoring Corrosion Process of Steel Sheet by Confocal Micro-XRF

Shintaro HIRANO, Koji AKIOKA, Takashi DOI, Masahiro ARAI and Kouichi TSUJI

X-Ray Spectrom., Vol. 43, pp. 216-220 (2014)

Non-destructive and non-contact analysis has been in demand on numerous occasions. Confocal micro X-ray fluorescence analysis enables depth-selective elemental analysis of solid samples in the laboratory. In this paper, we applied this technique for imaging elemental distributions in solutions. A low-carbon steel sheet was placed in artificial seawater (NaCl: 3.5 mass%), and the corrosion process in the solution was observed. A depth image of Fe K α intensity in the NaCl solution was obtained by using this technique. The Fe K α intensity in the solution was measured with corrosion time by sequential line analysis at a fixed lateral position. The corrosion of Fe from the steel sheet, the migration of Fe ions in solution, and their

condensation near a polymer window were successfully monitored.

An Estimation of the Number of Upstream Migration of Juvenile Ayu *Plecoglossus Altivelis Altivelis* in the Urbanized Yamato River by the Method of Micro-X-Ray Fluorescence Analysis

Mayu NAMITA, Hiromitsu ONCHI, Tenma ITAYA, Takashi NAKAZAWA, Kouichi TSUJI and Susumu YAMOUCHI

Kankyo Asesumento Gakkaishi Japan Society for Impact Assessment, Vol. 12, pp.101-108 (2014) (in Japanese)

Strontium or strontium calcium ratios in otoliths were determined employing the method of micro-X-ray fluorescence analysis along with the microscopic observation of daily growth rings of the otoliths. This enabled us to distinguish natural Ayu from artificially released ones, and to estimate the number of upstream migrating Ayu in the Yamato River. As a result, of the Captured Ayu, 20 individuals of the 27 individuals in 2010, 41 individuals of the 44 individuals in 2011, and 29 individuals of the 32 individuals in 2012 were thought to be natural and the remaining individuals were artificially released ones. A total of 14,000 to 33,000 individuals of the natural Ayu were expected to ascend the lower areas of the Yamato River from 2010 to 2012.

Underfilm Corrosion of Steel Sheets Observed by Confocal 3D-XRF Technique

Koji AKIOKA, Takashi NAKAZAWA, Takashi DOI, Masahiro ARAI and Kouichi TSUJI

Powder Diffraction, Vol. 29, pp. 151-154 (2014)

A confocal micro-X-ray fluorescence (XRF) method with a vacuum chamber was used for investigation of underfilm corrosion that occurs on a painted steel sheet used for automotive applications. A painted steel sheet was prepared by applying electrodeposition coating onto an electro-galvanized steel sheet with a zinc phosphate conversion coating. The spatial resolution of the confocal micro-XRF was about 10.9 μm at an energy of 17.4 keV. The phosphorus signal from the zinc phosphate layer was able to be observed nondestructively by measuring under the vacuum condition. Each layer of the painted steel sheet was observed from the depth profile analysis of the characteristic elements of each layer. The painted steel sheet was scratched to expose the substrate surface, and then the sheet was then immersed in a NaCl solution for 10 days. The in-depth elemental map of Ti of the corroded steel sheet revealed blister-type corrosion around the scratch. The in-depth elemental maps of Zn and P suggested that the zinc phosphate layer dissolved from the scratched part into the NaCl solution.

First Total Reflection X-Ray Fluorescence Round-Robin Test of Water Samples: Preliminary Results

Laura BORGESSE, Fabjola BILO, Kouichi TSUJI, Ramón FERNÁNDEZ-RUIZ, Eva MARGUI, Christina STRELI, Giancarlo PEPPONI, Hagen STOSNACH, Takashi YAMADA, Peter VANDENABEELE, David M. MAINA, Michael GATARI, Keith D. SHEPHERD, Erick K. TOWETT, Leonardo BENNUN, Graciela CUSTO, Cristina VASQUEZ and Laura E. DEPERO

Spectrochimica Acta Part B, Vol. 101, pp. 6-14 (2014)

Total Reflection X-Ray Fluorescence (TXRF) is a mature technique to evaluate quantitatively the elemental composition of liquid samples deposited on clean and well polished reflectors. In this paper the results of the first worldwide TXRF round-robin test of water samples, involving 18 laboratories in 10 countries are presented and discussed. The test was performed within the framework of the VAMAS project, interlaboratory comparison of TXRF spectroscopy for environmental analysis, whose aim is to develop guidelines and a standard methodology for biological and environmental analysis by means of the TXRF analytical technique.

Development of a Compact Grazing Exit X-Ray Fluorescence Spectrometer for Fast Trace Elemental Analysis

Takafumi ASHIDA and Kouichi TSUJI

Spectrochimica Acta Part B, Vol. 101, pp. 200-203 (2014)

A compact grazing exit X-ray fluorescence (GE-XRF) spectrometer was developed in the laboratory. An Al cylindrical collimator for the primary X-rays was placed just above the sample stage. This collimator also played the role of an exit slit to detect fluorescent X-rays at small grazing exit angles. Therefore, no additional exit slit was used in this setup, leading to a compact design. The entire size of the analysis

equipment was 80 mm × 200 mm × 170 mm (horizontal × vertical × height). The maximum exit angle was adjusted to the height of the sample stage. The background was drastically reduced at grazing exit angles, enabling trace elemental analysis. A calibration curve was obtained using 10 μL Ga solutions. Accordingly, the detection limit for Ga was evaluated to be 20 ppb.

In Situ Observations of Thermoreversible Gelation and Phase Separation of Agarose and Methylcellulose Solutions under High Pressure

Noritsugu KOMETANI, Masahiro TANABE, Lei SU, Kun YANG, and Katsuyoshi NISHINARI

J. Phys. Chem. B, Vol. 119, pp. 6878–6883 (2015)

Thermoreversible sol–gel transitions of agarose and methylcellulose (MC) aqueous solutions on isobaric cooling or heating under high pressure up to 400 MPa have been investigated by in situ observations of optical transmittance and falling-ball experiments. For agarose, which undergoes the gelation on cooling, the application of pressure caused a gradual rise in the cloud-point temperature over the whole pressure range examined, which is almost consistent with the pressure dependence of gelling temperature estimated by falling-ball experiments, suggesting that agarose gel is stabilized by compression and that the gelation occurs nearly in parallel with phase separation under ambient and high-pressure conditions. For MC, which undergoes the gelation on heating, the cloud-point temperature showed a slight rise with an initial elevation of pressure up to 150 MPa, whereas it showed a marked depression above 200 MPa. In contrast, the gelling temperature of MC, which is nearly identical to the cloud-point temperature at ambient pressure, showed a monotonous rise with increasing pressure up to 350 MPa, which means that MC undergoes phase separation prior to gelation on heating under high pressure above 200 MPa. Similar results were obtained for the melting process of MC gel on cooling. The unique behavior of the sol–gel transition of MC under high pressure has been interpreted in terms of the destruction of hydrophobic hydration by compression.

High Pressure Study of Rotational Dynamics of Perylene and Sodium 8-Methoxyperylene-1,3,6-trisulfonate in Imidazolium-Based Ionic Liquids

Noritsugu KOMETANI and Atsuko TAI

J. Solution Chem., Vol. 43, pp.1529-1538 (2014)

Rotation times of perylene and 8-methoxyperylene-1,3,6-trisulfonate (MPTS) in 1-alkyl-3-methylimidazolium tetrafluoroborate and 1-alkyl-3-methylimidazolium hexafluorophosphate under high pressure have been examined by means of the time-resolved fluorescence anisotropy measurements. The isothermal compression of sample solutions by the application of high pressure could change the solvent viscosity alone over a wide range, allowing for an observation of the pure viscosity dependence of rotation times at a constant temperature (45°C). Rotation times of both perylene and MPTS show a considerably nonlinear dependence on the solvent viscosity and a substantial deviation from the predictions of hydrodynamic and quasihydrodynamic theories particularly at high pressures.

Catalytic Effects of Copper Oxides on the Decomposition of Chlorophenol by the Hydrothermal Oxidation

Noritsugu KOMETANI, Kyohei NAKAO and Hiroki HONDA

J. Soc. Mater. Sci. Jpn., Vol. 63, pp. 674-678 (2014) (in Japanese)

It has been revealed that hydrothermal oxidation of persistent organochlorine substances is dramatically facilitated with the aid of Cu-based catalysts such as Cu-supported WO₃, because the Fenton-type reaction catalyzed by Cu ions undergoes substantial acceleration under subcritical conditions of water at around 200–300°C, leading to the increased formation of hydroxyl radicals which possess a strong oxidative power. In this study, the catalytic hydrothermal oxidation of 4-chlorophenol with CuO or Cu₂O has been examined using the slurry flow and catalyst packed-bed reactor systems. It is found that Cu₂O has a remarkable catalytic activity for the hydrothermal oxidation of 4-chlorophenol compared with those of CuO and Cu-supported TiO₂. The conversion of 4-chlorophenol reached nearly 100% at reaction temperatures around 130°C when Cu₂O was used as catalyst, indicating that it is possible to substantially reduce the reaction condition required for the complete decomposition of persistent organochlorine substances by the hydrothermal oxidation. The continuous treatment of 4-chlorophenol has been also conducted using the packed-bed reactor system with Cu₂O. The results demonstrated that 4-chlorophenol could be degraded for up to 22 hours without significant loss of the catalytic activity.

Advanced Treatment Technique of Polluted Water by the Combination of Fenton and Hydrothermal Oxidation Methods using Copper Oxide Catalysts

Noritsugu KOMETANI

Chemical Engineering, Vol.6, pp. 504-508 (2015) (in Japanese)

Catalytic Activity of *Epi*-Quinine-Derived 3,5-Bis(trifluoro-methyl)benzamide in Asymmetric Nitro-Michael Reaction of Furanones

Tohru SEKIKAWA, Takayuki KITAGUCHI, Hayato KITAURA, Tatsuya MINAMI and Yasuo HATANAKA

Org. Lett., Vol. 17, pp. 3026–3029 (2015)

High catalytic activity of novel *epi*-quinine-derived 3,5-bis(CF₃)benzamide in the asymmetric nitro-Michael reaction is described. With 0.1-5 mol % loadings of this catalyst, the addition of 5-substituted 2(3-*H*)-furanones to a wide range of nitroalkenes involving challenging substrates, β -alkyl-nitroalkenes smoothly proceeded, giving the Michael adducts in high yields (> 90%) with excellent diastereo- and enantioselectivity (> 98:2 dr, syn major; 88-98% ee). DFT calculation was carried out to account for the high catalytic activity.

Development of Environmental Harmony Resist Removal System using Cryogenic Particulate Spray

Jun ISHIMOTO and Hideo HORIBE

J. Photopolym. Sci. Tech., Vol. 28, pp. 285-288 (2015)

It is numerically found that the atomization of LN₂ droplet is induced by shear flow between LN₂ and gaseous nitrogen (GN₂) flow. Sequentially, liquid to solid phase change is enhanced and solid nitrogen (SN₂) particle is continuously created by LN₂ droplet freezing. By using ToF-SIMS and XPS analysis for resist removal experiment, the obtained C film thickness of resist removal section is 0.2 nm. Therefore, the photo resist can be successfully removed by using cryogenic solid particulate spray method.

Effect of Microbubbles on Ozonized Water for Photoresist Removal

Masayoshi TAKAHASHI, Hideo HORIBE, Kouhei MATSUURA and Katsumi TATERA

J. Photopolym. Sci. Tech., Vol. 28, pp. 293-298 (2015)

The existence of microbubbles in ozonized water has been shown to significantly enhance the photoresist removal rate due to an elevated dissolved ozone concentration and a direct effect of the microbubbles relating to the radical generation. Additionally, the ozone microbubble solution was able to effectively remove a high-dose ion-implanted photoresist, which is extremely resistant to removal by ozonized water and other wet chemicals because of its amorphous carbon-like layer, or "crust". Electron spin resonance experiments were also performed without the influence of serious metal contamination and indicated the presence of hydroxyl radicals, which are thought to be formed by interaction of ozone with hydroxide ions adsorbed at the gas-water interface upon collapse of the microbubbles.

Degradation of Polymers for Resist using Microbubbles on Ozonized Water

Kohei MATSUURA, Takashi NISHIYAMA, Eriko SATO, Masashi YAMAMOTO, Masayoshi TAKAHASHI, Kunihiro KOIKE and Hideo HORIBE

J. Photopolym. Sci. Tech., Vol. 28, pp. 299-301 (2015)

A significant effect of microbubbles on degradation of novolak resin could not be confirmed. Microbubbles efficiently dissolved ozone in solution, enhancing dissolved ozone concentration. By using ozone microbubbles, removal rate of novolak resin was enhanced. We expect that the effect of polymer degradation by microbubbles would be made more obvious by setting suitable conditions such as pH, ionic strength, and removal process.

Enhancement of Photoresist Removal Rate by Using Atomic Hydrogen Generated under Low-Pressure Conditions

Masashi YAMAMOTO, Hironobu UMEMOTO, Keisuke OHDAIRA, Shiro NAGAOKA, Tomokazu SHIKAMA, Takashi NISHIYAMA and Hideo HORIBE

J. Photopolym. Sci. Tech., Vol. 28, pp. 303-306 (2015)

Instead of photoresist removal methods using chemicals, we investigated a novel, environmentally friendly removal method using atomic hydrogen generated on a tungsten hot-wire catalyst. We revealed that the photoresist removal rate is remarkably enhanced under low hydrogen pressure conditions. This enhancement may be ascribed to the high kinetic energy of H atoms. If we optimize the removal conditions, the removal rate may become comparable to that achieved when chemicals are used.

Dependence on Resist Stripping Efficiency to Irradiating Beam Size in Advanced Laser Resist Stripping Method

Tomosumi KAMIMURA, Yuta KUROKI, Takuma MURAKAMI, Kosuke NUNO, Masaya AKIMOTO, Yoshiyuki HARADA, Takashi NISHIYAMA and Hideo HORIBE

J. Photopolym. Sci. Tech., Vol. 28, pp. 307-311 (2015)

Dependence on the stripping efficiency to irradiating beam size was investigated in an advanced laser resist stripping method. The beam size on the resist surface was changed from 0.3 mm to 3.0 mm. An intensity shape of the laser beam was Gaussian shape. At a beam diameter of 0.3mm, the stripped resist area in a beam was 15 % of 0.01 mm². In the case of beam diameter of 3.0 mm, the stripped resist area in a beam was 5 % of 0.38 mm². The stripped area improves 38 times for scale-up of the beam area of 100 times. The resist stripping efficiency was thought to depend on the heat stress due to a temperature gradient between the beam center and the regions without laser irradiation. Irradiation with multiple laser beams by small beam diameter was confirmed as one of the methods for improvement of a resist stripping rate with high efficiency.

Estimation of Activation Energies for Decomposition Reaction of Polymer by Hydrogen Radicals Generated Using Hot-Wire Catalyzer

Akihiko KONO, Yu ARAI, Yousuke GOTO, Masashi YAMAMOTO, Seiji TAKAHASHI, Tadaaki YAMAGISHI, Kenji ISHIKAWA, Masaru HORI and Hideo HORIBE

Thin Solid Films, Vol. 575, pp. 17-20 (2015)

This paper discusses the decomposition processes of polymer thin films coated on silicon (Si) substrates by hydrogen radicals generated from H₂ on hot-wire catalyst surfaces. N₂ buffer was used to relax the translational motion of hydrogen radicals. It is shown that H atoms react to polymer films under thermal equilibrium conditions when the total pressure is 21.3 Pa and the distance between the catalyst and the substrate is 100 mm. Polymers with benzene ring such as phenol resin, polystyrene, poly(vinylphenol), and poly(α -methylstyrene) exhibited both low removal rate and high activation energy of decomposition compared to those polymers without benzene ring such as poly(methylmethacrylate) and poly(isobutylene). We concluded that benzene ring with CC bond and resonance structure is resistant to decomposition by hydrogen radicals.

Study of the Decomposition Mechanism of PMMA-Type Polymers by Hydrogen Radicals

Yu ARAI, Yusuke NOTO, Yousuke GOTO, Seiji TAKAHASHI, Masashi YAMAMOTO, Takashi NISHIYAMA, Akihiko KONO, Tatsuo ISHIJIMA, Kenji ISHIKAWA, Masaru HORI and Hideo HORIBE

Thin Solid Films, Vol. 575, pp. 12-16 (2015)

The relationship between the chemical structure of PMMA-type polymers and the removal rate by hydrogen radicals was examined. Hydrogen radicals are known to have superior reduction ability and can be generated by decomposing H₂ on hot-wire surfaces. PMMA-type polymers, which are widely used as base polymers for ArF resist, have many variations with the difference in the substituents. The removal rate of the main chain scission type polymers was faster than that of the main chain cross-linking type polymers. In the main chain cross-linking type polymers, it is considered that reduction decomposition of polymer was inhibited apparently according to occurrence to simultaneously reduce decomposition by hydrogen radicals and main chain cross-link. The removal rate was slow in the case of the main chain scission type polymers with a benzene ring. We guessed that the polymer with a benzene ring was a stable structure by resonance stabilization of a benzene ring. We found that the removal rate was slow according to increasing bulkiness of α -side chain in the main chain scission type polymers. It is considered that etching resistance increases with increasing bulkiness of α -side chain of polymer.

The Effect of the Structural Order of Isotactic Polypropylene Containing Magnetically Aligned Nickel Particles on Its Electrical Resistivity

Masafumi YAMATO, Shuhei OBAYASHI, Takashi NISHIYAMA, Hideo HORIBE, Kohki TAKAHASHI and Kazuo WATANABE

Polymer, Vol. 55, pp. 6546-6551 (2014)

The effect of the high order structure of an isotactic polypropylene (PP) composite on the resistivity of composites containing magnetically aligned Ni particles was studied. Only a small amount of particles needed to be added for the composite material to become conducting after heating while in a magnetic field. The Ni columns formed on applying the field were distorted by the formation of large PP spherulites. Changes to the crystallization process due to the addition of a nucleating agent gave rise to changes in the columnar structure, resulting in large changes in the resistivity of the composite material. Controlling the high order structure of the polymer matrix including its morphology is very important in order to be able to control the magnetically aligned Ni structure.

Synthesis, Thermal, Optical, and Mechanical Properties of Sequence-Controlled Poly(1-adamantyl acrylate)-*block*-Poly(*n*-butyl acrylate) Containing Polar Side Group

Yoshinori NAKANO, Eriko SATO and Akikazu MATSUMOTO

J. Polym. Sci., Part A: Polym. Chem., Vol. 52, pp. 2899-2910 (2014)

We prepared the sequence-controlled block copolymers including poly(1-adamantyl acrylate) (PA_dA) and poly(*n*-butyl acrylate) sequences as the hard and soft segments, respectively, by the organotellurium-mediated living radical polymerization. The thermal, optical, and mechanical properties of the adamantane-containing block copolymers with polar 2-hydroxyethyl acrylate (HEA) and acrylic acid (AA) repeating units were investigated. The microphase-separated structures of the block copolymers were confirmed by the differential scanning calorimetry and atomic force microscopy observations as well as dynamic mechanical measurements. The α - and β -dispersions due to the main-chain and side group molecular motions, respectively, of the hard and soft segments were observed. Their transition temperatures and activation energies increased due to the formation of intermolecular hydrogen bonding by the introduction of the HEA and AA repeating units. The effects of the hydrogen bonding on their tensile elasticity, strength, and strain were also evaluated.

Acetal-Protected Acrylic Copolymers for Dismantlable Adhesives with Spontaneous and Complete Removability

Eriko SATO, Keisuke YAMANISHI, Tadashi INUI, Hideo HORIBE and Akikazu MATSUMOTO

Polymer, Vol. 64, pp. 260-267 (2015)

Acetal-protected acrylic copolymers consisting of 1-isobutoxyethyl acrylate (iBEA), 2-ethylhexyl acrylate (2EHA), and 2-hydroxyethyl acrylate (HEA) repeating units were applied to the pressure-sensitive adhesive (PSA) types of dismantlable adhesives. The random and block copolymers with a relatively high HEA content showed good PSA properties before dismantling treatment. The deprotection of the acetal protected group of the iBEA unit took place in response to individual external stimuli, soaking in boiling water and UV irradiation in the presence of a photoacid generator. The random copolymers containing an HEA unit of more than 10 mol% and an iBEA unit of more than 70 mol% achieved spontaneous debonding with interfacial failures at both the stainless steel and polyethylene terephthalate support film sides by soaking in boiling water within 10 min, whereas the corresponding block copolymer did not achieve interfacial failure even after a 20-min soaking. Photoirradiation of the random copolymers containing N-hydroxynaphthalimide triflate as a photoacid generator resulted in interfacial failures at both sides with a sufficiently reduced peel strength, where cross-linking arose due to the transacetalization and transesterification of a hydroxy group in the HEA unit along with deprotection.

Dual Stimuli-Responsive Homopolymers: Thermo- and Photo-responsive Properties of Coumarin-Containing Polymers in Organic Solvents

Eriko SATO, Yuki MASUDA, Joji KADOTA, Takashi NISHIYAMA and Hideo HORIBE

Eur. Polym. J., Vol. 69, pp. 605-615 (2015)

Thermoresponsive properties of poly(7-methacryloyloxycoumarin) (**P1a**) and its derivatives as homopolymers containing a photoreactive coumarin unit were systematically investigated. **P1a** showed a

lower critical solution temperature (LCST)-type phase separation in dichloromethane, chloroform, and 1,1,2-trichloroethane. The temperature producing a 50% transmittance (T_c) of 0.1 wt% **P1a** in distilled chloroform was 26 °C, while the T_c value decreased to 21 °C in deuterated chloroform i.e., the deuterium isotope effect. The T_c values in chloroform were adjustable from 28 to 57 °C by the introduction of the ethyleneoxy spacer and α -methyl group to **P1a**. While the polymers containing 4-substituted coumarins were soluble in chloroform and dichloromethane from 0 °C to their boiling points. In the distilled chloroform solution, the coumarin units in **P1a** underwent a [2+2] cycloaddition and the transmittance at 500 nm decreased from 98 to 29 % at 25 °C by a 180-sec photoirradiation (326 mJ/cm², emission band at 365 nm).

Analysis of Initiation Mechanism for Thermal Curing of Multifunctional Hyperbranched Polymers by Radical Trapping

Eriko SATO, Izumi UEHARA, Takashi NISHIYAMA and Hideo HORIBE

Journal of Network Polymer, Japan, Vol. 36, pp. 186-191 (2015) (in Japanese)

We have reported that multifunctional hyperbranched polymers are synthesized by radical homopolymerization of ethylene glycol dimethacrylate in the presence of methyl (2-bromomethyl)acrylate as an addition-fragmentation chain transfer agent. The hyperbranched polymers contain the pendant vinyl groups and the ω -end vinyl groups, and exhibit thermosetting properties in the absence of any catalyst. In this study, the initiation mechanisms for the thermal curing of the hyperbranched polymer were investigated by radical trapping using a nitroxide free radical. The hyperbranched polymer reacted with 4-hydroxy-2,2,6,6-tetramethylpiperidine 1-oxy benzoate by heating at 150 °C showing that the curing proceeded by radical mechanism. The ¹H NMR analysis of the product revealed that the cleavage of Br-CH₂ bond and C-C bond adjacent to a vinyl group having relatively low bond dissociation energies has minor contribution to the radical formation and thermal curing proceeds by spontaneous polymerization of vinyl groups.

Precise Synthesis of Reactive Polymers and Their Application to Functional Adhesive Materials

Eriko SATO

The 8th Symposium on Precisely Designed Network Polymer for Young Researcher, Invited Lecture, Higashiosaka, March 6, 2015 (in Japanese)

Design and Precise Synthesis of Reactive Acrylic Polymers

Eriko SATO

KOBUNSHI-DOYUKAI Kansai Workshop, Invited Lecture, Osaka, April 7, 2015 (in Japanese)

Design and Precise Synthesis of Functional Polymers

Eriko SATO

Colour Material Seminar, Invited Lecture, Osaka, May 20, 2015 (in Japanese)

Precise Synthesis of Multifunctional Hyperbranched Polymers by Metal-Free and One-Pot Reactions

Eriko SATO

Malaysian Scientific Association (MSA) International Symposium on Organic Chemistry (ISOC) in Conjunction with MSA 60th Anniversary 2015, Invited Lecture, Kuala Lumpur, Malaysia, September 22, 2015, Abstract Books, p. 138

Photochromism of Diarylethene Molecules and Crystals: Memories, Switches, and Actuators

Masahiro IRIE, Tuyoshi FUKAMINATO, Kenji MATSUDA and Seiya KOBATAKE

Chem. Rev., Vol. 114, pp. 12174–12277 (2014)

A new class of thermally irreversible photochromic molecules, named “diarylethene”, was serendipitously discovered a quarter of a century ago. The dithienylperfluorocyclopentene derivatives undergo thermally irreversible, fatigue resistant, ultrafast and highly sensitive photochromic reactions. The outstanding photochromic performance attracts considerable attention from both scientific and technological points of view, and stimulates researches on the diarylethenes from fundamental 33ft he-chemical aspects to various applications in optical memories, switches and molecular machines. In this review development of studies on

diarylethene molecules and crystals over the past 10 years is described.

Synthesis and Characterization of Amphiphilic Silica Nanoparticles Covered by Block Copolymers Branching Photochromic Diarylethene Moieties on Side Chain

Ryuta SENO and Seiya KOBATAKE

Dyes Pigm., Vol. 114, pp. 166–174 (2015)

Silica nanoparticles covered with polystyrene branching diarylethene moieties to the side chains are synthesized by reversible addition-fragmentation chain transfer polymerization on silica nanoparticles. The resulting nanoparticles are soluble in toluene and tetrahydrofuran and show reversible photoisomerization upon alternating irradiation with ultraviolet and visible light. The photoreversible isomerization follows color change, which is called photochromism. During the photochromic reactions, the nanoparticles are dispersed in solutions such as tetrahydrofuran. The modification by further block copolymerization of N-isopropylacrylamide results in fabrication of photochromic silica nanoparticles soluble in both tetrahydrofuran and water.

Photoreversible Current ON/OFF Switching by Photoinduced Bending of Gold-Coated Diarylethene Crystals

Daichi KITAGAWA and Seiya KOBATAKE

Chem. Commun., Vol. 51, pp. 4421–4424 (2015)

We investigated the photoinduced crystal bending behavior of **1a** before and after gold deposition. The crystals of **1a** showed photoreversible crystal bending upon irradiation with alternating UV and visible light before and after gold deposition. It was revealed that the relationship between the initial speed of the curvature change and the crystal thickness was well explained by Timoshenko's bimetal model and the extended bimetal model before and after gold deposition, respectively. Moreover, we have demonstrated the photoreversible ON/OFF switching of the electric circuit using the gold-coated diarylethene crystal. The current could be flowed in the gold layer on the surface of diarylethene crystal without any resistance. Furthermore, the photoreversible current switching by the photoinduced bending of the gold-coated diarylethene crystal could be repeated over 10 cycles upon alternating irradiation with UV and visible light. These findings bring about not only a new strategy to design for photomechanical actuators but also a new practical use of photomechanical crystals.

Polymorphic Crystallization and Thermodynamic Phase Transition between the Polymorphs of a Photochromic Diarylethene

Chika IWAIHARA, Daichi KITAGAWA and Seiya KOBATAKE

Cryst. Growth Des., Vol. 15, pp. 2017–2023 (2015)

We synthesized a photochromic diarylethene, 1,2-bis(2-methyl-5-(4-hexyloxyphenyl)-3-thienyl)-perfluorocyclopentene (**1a**), and found that it has two types of crystals, a needle-like α -crystal and a plate-like β -crystal. From X-ray crystallographic analysis, the space groups of the α - and β -crystals were determined to be $P\bar{1}$ and $C2/c$, respectively. The molecular conformation and packing of two crystal forms are quite different. The α - and β -crystals can be obtained individually by recrystallization from acetone at different temperatures. The solvent-mediated phase transition from the α -crystal to the β -crystal was found to occur in the acetone solution at room temperature. Moreover, the thermodynamic phase transition from α -form to β -form was found to take place above 88 °C, as confirmed by differential scanning calorimetry measurement, optical microscopic observation under crossed Nicols, and powder X-ray diffraction measurement. The phase transition from α -form to β -form was also observed at 78 °C by photochromic reaction of **1a**, and the phase transition proceeded from the UV irradiated part to the nonirradiated part.

Synthesis and Optical Properties of Gold Nanoparticle Networks Cross-Linked with Chain-Length-Controlled Polymers

Emi SUGATA and Seiya KOBATAKE

RSC Adv., Vol. 5, pp. 34704–34708 (2015)

In order to control the absorption band ascribed to localized surface plasmon resonance (LSPR) of gold nanoparticles (AuNPs) in solution, we newly synthesized a gold nanoparticle network (AuNP-NW) crosslinked with chain-length-controlled polymers. The chain-length-controlled polystyrene (poly(St))

having dithiobenzoate groups at both termini was synthesized by reversible addition-fragmentation chain transfer (RAFT) polymerization with a novel RAFT agent which enables the precise control of the chain length of the polymers. Both terminal groups of poly(St) were reduced from dithiobenzoate groups to thiol groups. The AuNP-NW was prepared by the self-organized cross-linking of individual AuNPs with poly(St) having thiol groups at both termini. Transmission electron microscopy images and absorption spectra of the AuNP-NW indicate the presence of a network structure. The absorption band due to LSPR of the AuNP-NW could be changed by the precise control of the distance between the AuNPs.

Restricted Diffusion of Guest Molecules in Polymer Thin Films on Solid Substrates as Revealed by Three-Dimensional Single-Molecule Tracking

Syoji ITO, Yuhei TAGA, Kengo HIRATSUKA, Satoshi TAKEI, Daichi KITAGAWA, Seiya KOBATAKE, and Hiroshi MIYASAKA

Chem. Commun., Vol. 51, pp. 13756–13759 (2015)

Single-molecule tracking (SMT) of fluorescent guest dyes can provide information on microscopic inhomogeneity in host polymer materials through the dynamics of individual guests depending on the local environment. In the conventional SMT, two-dimensional motions of guests were analyzed for the evaluation and it was difficult to extract the depth-dependent properties. In the present work, we applied three-dimensional (3D) SMT to the elucidation of anomalous motions of guest dyes in poly(2-hydroxyethyl acrylate) thin films on glass substrates by using so-called astigmatism imaging method. The 3D-SMT revealed that hydrophobic guest dyes did not approach the surface of glass substrate and typical distance from the surface was longer than 300 nm. In spite of the long distance from the surface, 5-10% of guest dyes still showed anomalous diffusion, which was attributed to the intrinsic inhomogeneity of the polymer film.

Dependence of Photoinduced Bending Behavior of Diarylethene Crystals on Irradiation Wavelength of Ultraviolet Light

Daichi KITAGAWA, Rika Tanaka and Seiya KOBATAKE

Phys. Chem. Chem. Phys., Vol. 17, pp. 27300–27305 (2015)

When irradiated with 365 nm light, a crystal of 1,2-bis(5-methyl-2-phenyl-4-thiazolyl)perfluorocyclopentene bends toward the incident light. In contrast, when irradiated with 380 nm light, the crystal first bends away from the light source and then bends toward the incident light. This bending behavior can be explained by a comprehensive mechanism based on the depth of the photochromic reaction from the crystal surface. This mechanism is successfully supported by the change of cell parameters associated with the photochromic reaction upon irradiation with 380 nm light, which was determined by *in situ* X-ray crystallographic analysis.

Photoinduced Mechanical Motion of Photochromic Crystalline Materials

Seiya KOBATAKE and Daichi KITAGAWA

In *Advances in Organic Crystal Chemistry, Comprehensive Reviews 2015*, Eds.: R. Tamura, M. Miyata, Springer, Chapter 27, pp. 533-547 (2015)

Photochromic compounds undergo a photochemically reversible transformation reaction between two isomers. Such molecules in organic crystals, which are regularly oriented and fixed in the crystal lattice, may be potentially useful for optoelectronic devices, such as optical memory, photoswitchable color filter, photoswitchable polarizer, photomechanical actuator, and so on. This chapter has focused on photochromism of the diarylethene crystals and their photomechanical phenomena, such as crystal bending and twisting.

Photoreversible Current ON/OFF Switching by Photoinduced Bending of Gold-Coated Diarylethene Crystals

Daichi KITAGAWA and Seiya KOBATAKE

22nd International Conference on the Chemistry of the Organic Solid State (ICCOSS 2015), Young Scientist Award Presentation, O16, Toki Messe, Niigata, Japan, July 12–17 (2015)

Photomechanical motions of photoresponsive molecular crystals have attracted much attention because they enable us to convert light energy into mechanical energy in direct without any contact and electric wires. Among various compounds which show photomechanical motions, diarylethene derivatives are the most promising compounds functioned as photomechanical actuators because of their rapid response, fatigue resistance, and thermal stability. Previously, we have reported the photoinduced crystal shape changes of

diarylethene crystals such as contraction, expansion, bending, fragmentation, and twisting. For further development of this research field, both theoretical and practical studies are required. Here, we have focused on the photoinduced bending behavior of gold-coated diarylethene crystals. The gold-coated rod-like crystals show photoreversible bending upon alternating irradiation with ultraviolet and visible light. The initial speed of bending depends on the crystal thickness and the relationship between the speed and the thickness can be well explained by using Timoshenko's bimetal model for the non-coated diarylethene crystals. Moreover, the bending behavior of the gold-coated diarylethene crystals can also be explained by the extended bimetal model which we propose here. The gold-coated layer on the crystal cannot be broken during the photoreversible bending. Thus, the photoreversible bending behavior can be used as actual electrical circuit switching which is very small size. These results provide not only a new useful strategy to design for photomechanical actuators but also a new practical use of photomechanical crystals.

Evaluation of the Relationship between Preparation Method and Photoinduced Bending Behavior of Diarylethene Microfibers

Hajime TSUJIOKA and Seiya KOBATAKE

22nd International Conference on the Chemistry of the Organic Solid State (ICCOSS 2015), Poster Presentation, P29, Toki Messe, Niigata, Japan, July 12–17 (2015)

Photochromic diarylethenes have drawn much attention because the chemical and physical properties can be changed by photoirradiation. Photomechanical effect of diarylethene crystals such as bending is an attractive property for the light-driven actuator. However, it is not easy to control the crystal shape and size in the molecular crystals. A simple preparation method of the light-driven actuator is required. We evaluated birefringence of microfibers and examined the relationship between molecular orientation and bending behavior. When the microfiber was irradiated with ultraviolet light, the microfiber was found to be bent in the direction towards the incident light. The bent fibers did not return to the initial-shaped fibers upon irradiation with visible light. When the microfiber was observed by polarizing microscopy under crossed Nicols, birefringence was confirmed. The birefringence means that the diarylethene molecules were oriented in the microfiber. To examine the relationship between birefringence and bending behavior of diarylethene microfibers, the microfibers having constant thickness and different birefringence were prepared under various conditions. Birefringence values of the microfibers were measured by Senarmont method. It was found that microfibers having high birefringence showed large bending curvature under the same photoirradiated conditions. These results suggest that the orientation of molecules relates to photoinduced bending behavior of microfibers.

Photochemistry and Solid State Property Changes of photoresponsive Organic Crystals

Seiya KOBATAKE

Annual Meeting on Photochemistry 2015, Award Lecture, AL04, Osaka City University, Japan, September 9–11 (2015)

Photochromic compounds undergo photochemically reversible transformation between two isomers. Such molecules in organic crystals, which are regularly oriented and fixed in the crystal lattice, may be potentially useful for optoelectronic devices. To apply photochromic crystals to photonics, electronics, mechanics, and medical fields, materials are required to change large physical property by photoirradiation. In most cases, compounds that exhibit photochromism in the crystalline phase are rare. Diarylethene derivatives exhibit thermally stable (P-type) photochromic reactions even in the crystalline phase. The P-type photochromic compounds have the potential to be used as optical memory, photoswitching, display, photomechanical actuator, and so on. This paper has focused on photochromism of the diarylethene crystals and their photomechanical phenomena.

Anti-Inflammatory Effect of Water-Soluble Complex of 1'-Acetoxychavicol Acetate with Highly Branched β -1,3-Glucan on Contact Dermatitis

Jiawei LI, Yui AIZAWA, Keiichi HIRAMOTO, Emiko KASAHARA, Daisuke TSURUTA, Toshio SUZUKI, Atsushi IKEDA, Hideki AZUMA and Takeshi NAGASAKI

Biomed. Pharmacother., Vol. 69, pp. 201-207 (2015)

The anti-inflammatory effect on contact dermatitis of the water solubilized 1'-Acetoxychavicol Acetate (ACA) by complexation with β -1,3-glucan isolated from *Aureobasidium pullulans* black yeast is reported. It

is well known that ACA possesses a function to inhibit the activation of NF- κ B by which genes encoding proinflammatory cytokines, chemokines, and growth factors are regulated. However, because ACA is quite insoluble in water, its usefulness has been extremely limited. On the other hand, a triple-helical polysaccharide β -1,3-glucan can include hydrophobic compounds into intra-strand hydrophobic cavity and solubilize poorly-water-soluble compounds. In this study, solubilization of ACA by complexation with highly branched β -1,3-glucan was achieved. The effect of anti-inflammatory response of water-soluble ACA complex with β -1,3-glucan was confirmed *in vitro* and *in vivo*.

Kojic Acid-Appended Carborane/Hydroxypropyl- β -Cyclodextrin Complex: A Novel Boron Carrier for Melanoma Targeting

Takeshi NAGASAKI, Junki KAWAGUCHI, Riku KAWASAKI, Masashi Sakuramoto, Mitsunori KIRIHATA, Yoshihide HATTORI, Shin-ichiro MASUNAGA and Yoshinori SAKURAI
KURRI Progress Report 2014, p. 7 (2015)

Although melanoma boron neutron capture therapy (BNCT) with L- 10 B-*p*-boronophenyl alanine has been treated for melanoma patient, the enhancement of 10 B accumulation in melanoma cells would lead to improved efficacy of malignant melanoma BNCT. Recently, we have evaluated the inclusion complex of kojic acid-appended carborane (CKA) with hydroxypropyl- β -cyclodextrin (HP- β -CD) as a novel boron agent for BNCT toward melanoma. CKA/HP- β -CD complex showed melanoma cells selectivity, unique nuclear localization, and high tumor-suppression effect on BNCT toward melanoma-bearing mice. Furthermore, CKA/HP- β -CD complex was found to be the potent inhibitor of hypoxia-induced HIF-1 α and to have a strong effect on tumor metastasis. Herein, in order to evaluate quantitatively metastasis-suppression, TaqMan RT-PCR assay of melanoma gene GP100 was carried out toward melanoma B16BL6 cells metastasis from thigh subcutaneous to lung in melanoma-bearing mice. TaqMan RT-PCR Assay toward GP100 is potent to estimate quantitatively the metastasis of melanoma cells to lung. The quantitative evaluation of metastasis-suppression effect of CKA/HP- β -CD complex is proceeding in our laboratory.

Evaluation of Boron-containing Rare Earth Oxides Nanoparticles as an Agent for Boron Neutron Capture Therapy

Takeshi NAGASAKI, Riku KAWASAKI, Shunsuke Iizuka, Hiroko YUKAWA, Yusuke TSUJIMOTO, Mitsunori KIRIHATA, Koji Tomita, Kiyofumi KATAGIRI, Koji ONO, Shin-ichiro MASUNAGA and Yoshinori SAKURAI
KURRI Progress Report 2014, p. 132 (2015)

Boron Neutron Capture Therapy (BNCT) is a highly selective cancer therapy that can target single tumor cell without causing excessive radiation damage around normal cells. The success of BNCT depends on the delivery that 10 B compounds accumulate effectively inside the tumor cells. Clinically, boronophenylalanine (BPA) and borocaptate sodium (BSH) are currently used for BNCT as boron delivery agents but these agents have some disadvantages on accumulation or selectivity toward tumor tissue. In addition, the efficacy of boron neutron capture reaction is suppressed due to low neutron fluence. In this study, in order to improve the efficiency of neutron capture reaction, we used boron containing rare earth oxides nanoparticle (SmBO₃, GdBO₃, YBO₃). When their diameter is suitable sizes, these nanoparticles could be significantly accumulated in tumor tissue with EPR effect. Moreover, the particle doped with europium can possess the fluorescence. This fluorescent nanoparticles are expected as novel boron delivery drugs that can diagnose and treat cancer simultaneously and efficiently.

Development of Efficient Boron Delivery System Using Enhanced Permeability and Retention Effect in Boron Neutron Capture Therapy

Masashi SAKURAMOTO, Yoshinori SAKURAI, Hiroki TANAKA, Shin-ichiro MASUNAGA, Koji ONO, Mitsunori KIRIHATA and Takeshi NAGASAKI
The 2nd International Symposium on Fusion Materials, Tokyo, Japan, November 2-4 (2014); Preprints

Cyclodextrin Complex of Kojic Acid Modified *o*-Carborane as a Novel BNCT Drug for Melanoma

Takeshi NAGASAKI, Riku KAWASAKI, S Yoshinori SAKURAI, Hiroki TANAKA, Shin-ichiro MASUNAGA, Koji ONO and Mitsunori KIRIHATA
The 2nd International Symposium on Fusion Materials, Tokyo, Japan, November 2-4 (2014); Preprints

Melanoma-Targeting Boron Delivery System Using Kojic Acid-Carborane Conjugate

Takeshi NAGASAKI, Riku KAWASAKI, Yoshihide HATTORI, Yoshinori SAKURAI, Hiroki TANAKA, Shin-ichiro MASUNAGA, Koji ONO and Mitsunori KIRIHATA
2nd International Workshop on BNCT – Basic Science and Technology for BNCT -, Invited Lecture, Kyoto, Japan, December 8-9 (2014); Preprints

Kojic Acid-Appended Carborane/Hydroxypropyl- β -Cyclodextrin Complex for Melanoma-Targeted Boron Neutron Capture Therapy

Takeshi NAGASAKI, Riku KAWASAKI, Yoshihide HATTORI, Shin-ichiro MASUNAGA, Yoshinori SAKURAI, Hiroki TANAKA, Koji ONO and Mitsunori KIRIHATA
8th Young Researcher BNCT Meeting, Pavia, Italy, September 13-17 (2015); Preprints

Development of Functional Food Materials Based on β -1,3-Glucan: from Food to Medical Materials

Toshio SUZUKI, Takeshi NAGASAKI and Hideaki IDOGAKI
Design of Supramolecular Structures and Development (ed. A. Harada), CMC Books, Tokyo, Japan (2014) (in Japanese)

Boron-Containing Rare Earth Oxides Nano-Particles for Boron Neutron Capture Therapy

Takeshi NAGASAKI and Koji TOMITA
Chemical Industry, Vol. 65, pp. 512-517 (2014) (in Japanese).

Development of a Bispecific Antibody Tetramerized through Hetero-Associating Peptides

Tomohiro OSAKI, Shingo FUJISAWA, Masahiro KITAGUCHI, Masaya KITAMURA and Takeshi NAKANISHI

FEBS J., Vol. 282, pp. 4389-4401 (2015)

The specific assembly of self-associating peptides can be useful in building a functional antibody complex from small antibody fragments. We have focused on the exceedingly specific heterotetrameric assembly of Lin-2 and Lin-7 (L27) domains, which work as protein-protein interaction modules in many scaffold proteins. Here, we describe a novel method for constructing a highly functional antibody based on the hetero-association of L27 domains. In this study, we used a bacterial expression system to produce a bispecific antibody that was heterotetramerized through L27 domains and that targeted both epidermal growth factor receptor (EGFR) and Fc γ receptor III (Fc γ RIII or CD16). Gel electrophoresis, mass spectrometry and gel filtration analyses revealed that the constructed recombinant antibody was a disulfide-linked heterotetramer. The tetramerized antibody bound to EGFR and CD16 simultaneously, according to results from flow cytometry and surface plasmon resonance spectroscopy, respectively. Furthermore, we demonstrated that the bispecific antibody showed cytotoxic activity against EGFR-expressing tumor cells by using CD16-positive lymphocytes as effectors, and its cytotoxicity was comparable to that of a commercial therapeutic antibody. Taken together, the results show that our method has high potential for the cost-efficient production of highly active therapeutic antibodies.

Preparation of Keratin and Chemically Modified Keratin Hydrogels and Their Evaluation as a Cell Substrate with Drug Releasing Ability

Ryo NAKATA, Yu OSUMI, Shoko MIYAGAWA, Akira TACHIBANA and Toshizumi TANABE
J. Biosci. Bioeng., Vol. 120, pp. 111-116 (2015)

Keratin (K) was extracted as a reduced form from wool, which was then subjected to acetoamidation, carboxymethylation or aminoethylation at abundant free cysteine residues to give acetoamidated keratin (AAK), carboxymethylated keratin (CMK) and aminoethylated keratin (AEK). Hydrogels were prepared from intact and three chemically modified keratins simply by concentrating their aqueous solution and subsequent cooling. The lowest concentration to form a hydrogel without fluidity was 110 mg/ml for AAK, 120 mg/ml for AEK, 130 mg/ml for K and 180 mg/ml for CMK. Comparing with a hydrogel just prepared (swelling ratio: 600-700), each hydrogel slightly shrank in an acidic solution. While AAK hydrogel little swelled in neutral and basic solutions, other hydrogels became swelled and CMK hydrogel reached to dissolution. Hydrogels of K, AAK and AEK were found to support cell proliferation, although cell elongation on AAK and AEK hydrogel was a little suppressed. On the other hand, CMK hydrogel did not

seem to be suitable for a cell substrate because of its high swelling in culture medium. Evaluation of the hydrogels as a drug carrier showed that K and AAK hydrogels were good sustained drug release carriers, which showed the drug release for more than three days, while the release from AEK and CMK hydrogels completed within one day. Thus, keratin and chemically modified keratin hydrogels, especially K and AAK hydrogels, were promising biomaterials as a cell substrate and a sustained drug release carrier.

Characterization of a Thermostable Glucose Dehydrogenase with Strict Substrate Specificity from a Hyperthermophilic Archaeon *Thermoproteus* sp. GDH-1

Hiroshi AIBA, Yoshiaki NISHIYA, Masayuki AZUMA, Yuusuke YOKOOJI, Haruyuki ATOMI and Tadayuki IMANAKA

Biosci. Biotechnol. Biochem., Vol. 79, pp. 1094-1102 (2015)

A hyperthermophilic archaeon was isolated from a terrestrial hot spring on Kodakara Island, Japan and designated as *Thermoproteus* sp. glucose dehydrogenase (GDH-1). Cell extracts from cells grown in medium supplemented with glucose exhibited NAD(P)-dependent glucose dehydrogenase activity. The enzyme (TgGDH) was purified and found to display a strict preference for D-glucose. The gene was cloned and expressed in *Escherichia coli*, resulting in the production of a soluble and active protein. Recombinant TgGDH displayed extremely high thermostability and an optimal temperature higher than 85 °C, in addition to its strict specificity for D-glucose. Despite its thermophilic nature, TgGDH still exhibited activity at 25 °C. We confirmed that the enzyme could be applied for glucose measurements at ambient temperatures, suggesting a potential of the enzyme for use in measurements in blood samples.

Development of Catalyst Suitable for Microbial Fuel Cell which Deprives Cells of Electrons

Masayuki AZUMA

Division of Biochemical Engineering, The Society of Chemical Engineering. Newsletter. No.39, p11-14, (2015) (in Japanese)

Phosphorylation of Myosin II Regulatory Light Chain by ZIP Kinase is Responsible for Cleavage Furrow Ingression During Cell Division in Mammalian Cultured Cells

Kosuke HOSOBABA, Satoshi KOMATSU, Mitsuo IKEBE, Manato KOTANI, Xiao WENQIN, Taro TACHIBANA, Hiroshi HOSOYA and Kozue HAMAO

Biochem. Biophys. Res. Commun., Vol. 459, pp. 686-691 (2015)

Zipper-interacting protein kinase (ZIPK) is known to regulate several functions such as apoptosis, smooth muscle contraction, and cell migration. While exogenously expressed GFP-ZIPK localizes to the cleavage furrow, role of ZIPK in cytokinesis is obscure. Here, we show that ZIPK is a major MRLC kinase during mitosis. Moreover, ZIPK siRNA-mediated knockdown causes delay of cytokinesis. The delay in cytokinesis of ZIPK-knockdown cells was rescued by the exogenous diphosphorylation-mimicking MRLC mutant. Taken together, these findings suggest that ZIPK plays a role in the progression and completion of cytokinesis through MRLC phosphorylation.

A Novel Marker for Undifferentiated Human Embryonic Stem Cells

Kiyoshi HIGASHI, Masaki YAGI, Tatsuhiko ARAKAWA, Kouji ASANO, Kumiko KOBAYASHI, Taro TACHIBANA and Koichi SAITO

Monoclon. Antib. Immunodiagn. Immunother., Vol. 34, pp. 7-11 (2015)

Human embryonic stem cells (hESCs) are pluripotent stem cells from early embryos, and their self-renewal capacity depends on the sustained expression of hESC-specific molecules and the suppressed expression of differentiation-associated genes. To discover novel molecules expressed on hESCs, we generated a panel of monoclonal antibodies against undifferentiated hESCs. The antigen recognized by Mab2 is expressed on the cell surface of undifferentiated hESCs; three diffused bands with molecular mass between 30 and 60 kDa in the lysates of hESCs were diminished during hESC differentiation into neural cells. The expression of Mab2 antigen was also observed on the plasma membrane of lung cancer cells, and Mab2 detected 55, 50, and 35 kDa protein bands in the cell lysates. Immunoprecipitation followed by proteomics analyses identified CD147/basigin as a Mab2 antigen. Finally, the positive expression of CD147/basigin protein in undifferentiated hESCs was confirmed. These results suggested that CD147/basigin could be another undifferentiated hESC marker.

DBZ Regulates Cortical Cell Positioning and Neurite Development by Sustaining the Anterograde Transport of Lis1 and DISC1 through Control of Ndel1 Dual-Phosphorylation

Masayuki OKAMOTO, Tokuichi IGUCHI, Tsuyoshi HATTORI, Shinsuke MATSUZAKI, Yoshihisa KOYAMA, Manabu TANIGUCHI, Munekazu KOMADA, Min-Jue XIE, Hideshi YAGI, Shoko SHIMIZU, Yoshiyuki KONISHI, Minoru OMI, Tomohiko YOSHIMI, Taro TACHIBANA, Shigeharu FUJIEDA, Taiichi KATAYAMA, Akira ITO, Shinji HIROTSUNE, Masaya TOHYAMA and Makoto SATO

J. Neurosci., Vol. 35, pp. 2942-2958 (2015)

Cell positioning and neuronal network formation are crucial for proper brain function. Disrupted-in-Schizophrenia 1 (DISC1) is anterogradely transported to the neurite tips, together with Lis1, and functions in neurite extension via suppression of GSK3 β activity. Then, transported Lis1 is retrogradely transported and functions in cell migration. Here, we show that DISC1-binding zinc finger protein (DBZ), together with DISC1, regulates mouse cortical cell positioning and neurite development in vivo. DBZ hindered Ndel1 phosphorylation at threonine 219 and serine 251. DBZ depletion or expression of a double-phosphorylated mimetic form of Ndel1 impaired the transport of Lis1 and DISC1 to the neurite tips and hampered microtubule elongation. Moreover, application of DISC1 or a GSK3 β inhibitor rescued the impairments caused by DBZ insufficiency or double-phosphorylated Ndel1 expression. We concluded that DBZ controls cell positioning and neurite development by interfering with Ndel1 from disproportionate phosphorylation, which is critical for appropriate anterograde transport of the DISC1-complex.

Incorporation of Histone H3.1 Suppresses the Lineage Potential of Skeletal Muscle

Akihito HARADA, Kazumitsu MAEHARA, Yuko SATO, Daijiro KONNO, Taro TACHIBANA, Hiroshi KIMURA and Yasuyuki OHKAWA

Nucleic Acids Res., Vol. 43, pp. 775-786 (2015)

Lineage potential is triggered by lineage-specific transcription factors in association with changes in the chromatin structure. Histone H3.3 variant is thought to play an important role in the regulation of lineage-specific genes. To elucidate the function of H3.3 in myogenic differentiation, we forced the expression of GFP-H3.1 to alter the balance between H3.1 and H3.3 in mouse C2C12 cells that could be differentiated into myotubes. GFP-H3.1 replaced H3.3 in the regulatory regions of skeletal muscle (SKM) genes and induced a decrease of H3K4 trimethylation (H3K4me3) and increase of H3K27 trimethylation (H3K27me3). Similar results were obtained by H3.3 knockdown. In contrast, MyoD-dependent H3.3 incorporation into SKM genes in fibroblasts induced an increase of H3K4me3 and H3K27me3. In mouse embryos, a bivalent modification of H3K4me3 and H3K27me3 was formed on H3.3-incorporated SKM genes before embryonic skeletal muscle differentiation. These results suggest that lineage potential is established through a selective incorporation of specific H3 variants that governs the balance of histone modifications.

KRAS Mutation Confers Resistance to Antibody-Dependent Cellular Cytotoxicity of Cetuximab against Human Colorectal Cancer Cells

Yusuke NAKADATE, Yasuo KODERA, Yuka KITAMURA, Senji SHIRASAWA, Taro TACHIBANA, Tomohide TAMURA and Fumiaki KOIZUMI

Int. J. Cancer, Vol. 134, pp. 2146-2155 (2014)

Cetuximab is a chimeric IgG1 monoclonal antibody (mAb) that targets the extracellular domain of epidermal growth factor receptor (EGFR). Oncogenic KRAS mutations in tumors have been shown to be a negative predictor of the response of colorectal cancer (CRC) to cetuximab treatment. Cetuximab exerts its therapeutic effects through several mechanisms including antibody-dependent cellular cytotoxicity (ADCC). However, the influence of KRAS mutations on cetuximab-mediated ADCC is not fully understood. Here, we investigated cetuximab-mediated ADCC in two pairs of isogenic CRC cells with or without a KRAS mutation. Peripheral blood mononuclear cells (PBMCs) from healthy volunteers and NK92, a natural killer (NK) cell line that exogenously expresses Fc γ RIIIa (CD16a), were used as effector cells. In an ADCC assay, perforin-dependent target cell lysis was not affected by the KRAS mutation status. On the other hand, perforin-independent ADCC was observed only in CRC cells with wild-type KRAS, but not in cells with mutant KRAS. Neutralizing experiments revealed that the Fas-Fas ligand (FasL) interaction was responsible for the induction of apoptosis and perforin-independent ADCC. Furthermore, the presence of

effector cells clearly enhanced the growth-inhibitory effect of cetuximab only in CRC cells with wild-type KRAS, but not in those with mutant KRAS. These findings suggest that ADCC is an important mode of action of cetuximab and that KRAS mutation impairs the therapeutic effect exerted by cetuximab-mediated ADCC.

Retraction

The following article information appeared in Page 104 of Vol. 55 of this memoirs is retracted.

Amazing Catalytic Activity of *Epi*-Quinine-Derived 3,5-Bis(trifluoromethyl)-benzamide in Asymmetric Nitro-Michael Reaction of Furanones

Tohru SEKIKAWA, Takayuki KITAGUCHI, Hayato KITAURA, Tatsuya MINAMI, and Yasuo HATANAKA
J. Am. Chem. Soc., accepted

Architecture and Building Engineering

Load-displacement Behavior of Deployment of DCMS Basic Unit

Junichi KATO and Yoshiya TANIGUCHI

Proceedings of the International Association for Shell and Spatial Structures (IASS) Symposium 2015, "Future Visions" 17-20 August, Amsterdam, The Netherlands (2015)

DCMS (Deployable Closed-Membrane Structure) is a deployable structure consisting of membranes and a rod frame. This paper reports load-displacement behavior of a basic unit of DCMS on pressing and stretching test in 2 directions of the deployment of the unit. Pressing and stretching test are performed in the direction of axial deployment and pressing test is performed in the direction of nonaxial deployment. Test models are constructed of aluminum pipes, elastic cords, banding bands and 3 kinds of fabric membrane. At the test in the direction of axial deployment, stretching test shows that the self-equilibrium system of the unit generates restoring force against stretched deformation. Pressing test shows that snap through action may happen in the range of folding. At the test in the direction of non-axial deployment, pressing test shows the apparent rigidity of the unit is softening.

Stochastic Optimization Method for Tuned Mass Damper Systems of Spatial Structures Based on Order Statistics

Makoto YAMAKAWA (Tokyo Denki University) and Susumu YOSHINAKA

Journal of Structural Engineering, AIJ, Vol. 61B, pp. 531-536 (2015) (in Japanese)

In design of passive tuned mass damper (TMD) on the vibration control performance of the spatial structure, we have to decide the both of a spatial arrangement and characteristics of TMDs. To find an optimal design of the systems is formulated as Mixed-Integer Programming (MLP) problem. It is difficult to obtain the exact global optimum solution in general. However, such global solution might not be required. To find a good local solution of the TMD systems, we propose a stochastic optimization method. We investigate the behavior of the method through a numerical example.

Cross-Correlations among Daily Variations of Thermal Control Use, Thermal Sensation, Clothing Insulation and Outdoor Temperature during Cooling Season in Japan

Noriko UMEMIYA and Tomohiro TANIGUCHI

Proceedings of the 8th Windsor Conference: Counting the Cost of Comfort in a Changing World, 7-4, pp.1-8 (2014)

This survey was designed to investigate university student rooms to realize energy savings related to thermal control use and the relations among thermal sensation, clothing insulation, and outdoor air temperature in pre-cooling and post-cooling seasons. Results revealed the following: 1) Phase shifts to the outdoor air temperature mutually differ in pre-cooling and post-cooling seasons. 2) For neutral temperatures, although the effect of pre-cooling makes the act of opening a window less likely, that is not true in the post-cooling season. 3) For thermal sensations, the section rates of thermal control use vary in the pre-cooling season, but do not vary in the post-cooling season. 4) The clothing amount varies more during the pre-cooling season than during the post-cooling season.

Resident Evaluation of Soccer and Music Concert Noise Near a Soccer Stadium

Noriko UMEMIYA and Ken MURAMOTO

Proceedings of the 11th International Congress on Noise as a Public Health Problem (ICBEN) 2014, 6-20 (2014)

Large-scale popular music concerts attracting several tens of thousands of spectators have been held in Japan often during the last decade. Nagai Athletic Stadium in Osaka, an official FIFA soccer stadium that can accommodate 50 thousand spectators, has hosted more than 20 professional games annually since 1994 as the home stadium of a Japanese soccer league team: Serezo Osaka. It has also hosted a few popular music concerts since summer 2007. Surveys of soccer and concert noise were administered to residents near the stadium. Results show the following. 1) The degrees of noise annoyance and living disturbance are not significantly different for soccer and concert noise, although the noise level is reportedly higher for concerts. 2) Concert noise creates greater discomfort than soccer noise. 3) Noise annoyance is higher for residences

with high resistance to noise. 4) The visibility of the stadium is not strongly related to noise annoyance. 5) Consideration of the park and the stadium when they selected the living area is not strongly related to the noise annoyance. 6) The relation between living disturbance and noise annoyance is similar for soccer and concert noise. 7) Soccer noise annoyance is lower for residents who like playing soccer. Concert noise annoyance is lower for residents who pass the park and who take a walk in the park.

Relation Between Noise Evaluation and Daily Noise Exposure to Road Traffic Noise and Railway Noise

Naohiro KATADA, Noriko UMEMIYA and Tomohiro KOBAYASHI

Proceedings of the 11th International Congress on Noise as a Public Health Problem (ICBEN) 2014, 6-16 (2014)

This study examines the relation between daily noise exposure and noise sensitivity, effects of noise exposure on the relation between sensitivity and noise evaluation and the differences attributable to noise types. Some study showed that railway noise is more annoying than road traffic noise, but others demonstrated that road traffic noise is more annoying than railway noise. This study examined road traffic noise and railway noise as usual daily noises and investigates the relation between daily noise exposure to these noises and evaluation of noise. Building construction noise at the actual spot of building construction was selected as an object of evaluation. Conclusions are the following. 1) Respondents exposed to railway noise evaluated construction noise as annoying. However, no relation was found between road traffic noise and annoyance. 2) No relation was found between daily exposure and sensitivity to sound. 3) Among respondents not exposed to any noise in daily life, sensitive people answered that construction was annoying.

Change of Summer Thermal Control Use in Homes After Electricity Shortage Caused by 3.11 Disaster in Japan

Xiaoyong LIN and Noriko UMEMIYA

Proceedings of the 20th International Congress of Biometeorology, Cleveland, 5D.4, pp.1-12 (2014)

Electricity shortages prevailed in many areas of Japan after the earthquake that occurred in Tohoku on March 11, 2011. Almost all electricity generation by nuclear plants was halted in Japan after the disaster. Electricity conservation was requested by government in the national interest. Excessive air-conditioning and illumination were discouraged. Circumstances were most severe in the Kansai area, where half of the electricity generation capacity was done by nuclear power generation. In summer 2011, electric utilities in Kansai asked businesses and households to reduce electricity consumption by up to 15 percent. This study examined summer thermal control use in apartments in Osaka in Japan in 2004 and 2011. 1) Electricity charges were lower in 2011 by 6.0% in May and by 23.7% in August. The cooling charge was lower by 43.8%. The mean setting temperature was 26.0° C in 2004 and 27.5° C in 2011. 2) Degrees of air conditioner use and window opening and habits of 'saving electricity' did not differ. 3) Cooling charges related to the degree of window opening stronger when asleep than when awake. Habits of 'saving electricity' showed only slight effects on electric charges and cooling charges in 2011. 4) Relations between temperature settings and the degree of thermal control use were stronger in 2004 than in 2011. Temperature settings did not differ by living environment evaluation or habits of saving electricity either in 2004 or in 2011.

Measurements of Driving Energy in SPT and Various Dynamic Cone Penetration Tests

Tatsunori MATSUMOTO (Kanazawa University), Le Ta PHAN (Ho Chi Minh City University), Akihiko OSHIMA and Shinya SHIMONO (Kanazawa University)

Soils and Foundations, Vol. 55, pp. 201–212 (2015)

Driving energy was measured in a standard penetration test (SPT) and 12 types of dynamic cone penetration tests (DCPTs) having different configurations for the hammer, driving rod, anvil and cone tip. The driving energy transferred from the free falling hammer to the driving rod was estimated from the measurements of strain and acceleration below the anvil. Basically, the driving energy was estimated for 21 successive blows in order to obtain the mean value, the standard deviation (σ) and the coefficient of variance (COV) in the SPT and DCPTs. The dynamic cone resistance, q_{dyn} , was estimated from the driving energy, the corresponding set per blow, and masses of the hammer and the total rods. Thus, the estimated dynamic cone resistance was compared with the static cone resistance, q_t , from a cone penetration test (CPT). The main objective of this report is to provide information on the driving efficiency in the SPT and each DCPT. The mean values for e_f in the tests ranged from 52% to 76%. The values of COV for e_f ranged from 0.024 to 0.265. Even though the test results are limited, the dynamic cone resistance, q_t , estimated from the dynamic measurements were relatively good measures of the cone resistance from the CPT, showing the importance of the dynamic measurement in the SPT and DCPTs. In addition, possible factors influencing the driving efficiency, such as the hammer mass, the configuration of the driving rod (solid or hollow), the ratio of the diameter of the anvil and the diameter of the hammer, and the existence of a cushion or cushions between the anvil and the hammer, are discussed on the basis of the limited test results.

Reconsideration on Expression of Consolidation Characteristics of Clay by Logarithm Volume Ratio f — An Example of Dredged Clay —

Hirohisa OKADA (Kobe City) and Akihiko OSHIMA

J. Geotechnical Engineering, Vol. 10, pp. 187-199 (2015) (in Japanese)

Consolidation characteristics of clay, which are compressibility, permeability and consolidation velocity etc., are conventionally represented by relationships between the “arithmetic scaled” volume ratio f or void ratio e and the logarithmic scaled effective stress p , coefficient of permeability k and coefficient of consolidation c_v etc. However, some previous works have suggested that a relation of volume ratio f and effective stress p in double logarithmic scale ($\log f$ - $\log p$) is able to express compressibility of clay more reasonably than the one in single logarithmic scale (f - $\log p$). At the exordium of this paper, the rationale of representation of consolidation characteristics of clay including k and c_v by “logarithmic f ” than “arithmetic f ” was derived from a revisional study on them. Next, experimental results of a series of centrifuge consolidation test for the very soft clay (dredged clay) were examined. Then their results were numerically simulated for two cases of using “logarithmic f ” or “arithmetic f ”. As a consequence, consolidation curves experimentally obtained were correctly represented by the numerical simulation with “logarithmic f ”. Moreover, it was found that more stable and faster calculation is enabled by applying “logarithmic f ” instead of “arithmetic f ” to the expansion of the consolidation equation.

Development of Representative Soil Profile Model of Quaternary Alluvium in Osaka Region and Its Application to Liquefaction-Hazard Assessment

Akihiko OSHIMA, Suguru YAMADA, Teruyuki Hamada (Geo-Research Institute) and Mari KASUGAI (Geo-Research Institute)

The XIX INQUA (International Union for Quaternary Research) Congress, Nagoya, Japan (2015)

Subsurface ground in Osaka region is coated with loosely deposited alluvial sandy soil, a result of the formation of river delta which had begun since approximately 6,000 years ago at when Holocene glacial retreat was peaking. Since the alluvial sandy layer has shallow ground water table, higher risk of liquefaction occurrence during expected earthquake events has been pointed out. The Kansai Geo-informatics database has summarized and published the planar distributions of geotechnical properties, which are the thickness of the strata, the SPT-N value and the grain size characteristics, as mean value of each stratum. However, the database contains insufficient number of data of the grain size characteristics in comparison with the SPT-N data. Hence, it can be considered that the details of planar distributions and depth distributions or the regional characteristics of the alluvial sandy strata have not yet been necessarily comprehended.

In the present study, the regionality of grain size characteristics of alluvial sandy strata in Osaka region was examined, as shown below. First, digital models of alluvial sandy strata were developed using “Supporting

system for building representative soil profile model”, in which representative soil classification and mean SPT-N value at each 1m depth were given to each 250m × 250m mesh. Second, the value of fines content in each 1m depth for each mesh were obtained from a correlation between SPT-N and fines content. Additionally, based on the developed model, planar distributions of liquefaction risk were assessed for 2 cases in which the different groundwater level, current or lowered, were considered. Finally, the effect of liquefaction countermeasure with the groundwater drawdown method was examined by comparison of assessment results.

Comparison of Calculation on Self-Weight Consolidation of Dredged Clay Using Consolidation Properties Expressed by “Logarithmic Volume Ratio” and “Arithmetic Volume Ratio”

Hirohisa Okada (Kobe City), Akihiko OSHIMA and Suguru YAMADA

Proc. of the 6th Japan-China Geotechnical Symposium, Sapporo Aug. 30- Sep. 1 (2015)

This paper describes the effect of the initial volume ratio f_0 (or the initial water content w_0) on the rate of self-weight consolidation of dredged clay as well as the effect of the expressive form of the consolidation characteristics, by examinations on results of the consolidation calculation by means of the finite differential method. The consolidation characteristics such as the compression curve were considered to express either the arithmetic f or the logarithmic f in calculations performed with different f_0 (or w_0) conditions. It was found as conclusions that the faster rate of self-weight consolidation was observed in cases of the arithmetic f was considered, and the rate of consolidation became faster with an increase of f_0 . It is also found that the stable calculation can be performed if consolidation characteristics were expressed in $\log f$ form even though a large interval of time difference was configured. In contrast, the short interval of time difference was needed to obtain stable results from calculations with the arithmetic f expressive form.

Inhibition of avoidance and jumping behavior in ayu *Plecoglossus altivelis altivelis* by free ammonia

Hiromitsu ONCHI and Susumu YAMOCHI

Journal of Japan Society for Impact Assessment, Vol.13, pp.79-85 (2015) (in Japanese)

Behavioral experiments were conducted from February to March 2011 to clarify the effect of free ammonia (range 0.055-0.33mg/L) to the activity of ayu *Plecoglossus altivelis altivelis*. Test of avoidance behavior revealed that ayu tend to remain in the same place regardless of the concentration of free ammonia, and any avoidance behavior was not clearly confirmed for free ammonia at the concentration range used in this experiment. However, when free ammonia concentrations exceeded, the area of distribution of the school of ayu became significantly wider, and abnormal movement was confirmed. In the jumping experiment, the jumping rate with free ammonia concentration had a significant negative relationship with each other, and approximately 70% of ayu were not able to jump when the free ammonia concentration was 0.33 mg/L.

A Field Investigation on CO₂ Budget at a Salt Marsh Located at Coastal Urban Area

Toru ENDO, Yusuke NAKANO, Tenma ITAYA, Noriaki IKADA and Susumu YAMOCHI

Journal of Japan Society of Civil Engineers, Ser. B2 (Coastal Engineering), Vol. 70, pp. I_1196-I_1200 (2014) (in Japanese)

It is thought that a salt marsh located at coastal urban area absorbs and emits large amounts of carbon dioxide (CO₂). In this study, a field investigation on CO₂ budget was conducted at Osaka-Nanko bird sanctuary, and CO₂ fluxes were measured at tidal flat, sea surface and reed field by using chamber methods in order to estimate CO₂ budgets of the salt marsh. The results of this study were as follows: (1) CO₂ fluxes of tidal flat and reed field were one order larger than that of sea surface. (2) It was estimated that CO₂ flux emitted from tidal flat was 3.26 g/m²/day and CO₂ flux absorbed by reed grass field was 1.53 g/m²/day in October 2013. (3) It was suggested from the result of seasonal change of fluxes that the absorbed amount of CO₂ becomes larger on summer than on autumn.

An Analysis on Influence Factors to Use Frequency and WTP of Shopping Support Services for People in Food Desert

Noboru ISE and Yasuo HINO

Osaka City University, Memoirs of the Faculty of Engineering, Vol. 55, pp. 19-26 (2014)

Recently, the food desert problem has been becoming serious problem in mainly rural areas of Japan, because it must be improved by local responsibility according to local needs. Although, some applicable estimation method of the number of people in food desert (PFD) were developed by many studies, the estimations of the demand for and profit from each shopping support service will be also required. Therefore, this paper mainly aims to gain the fundamental knowledge not only to develop the estimation model of the

demand for each shopping support service for PFD but also to evaluate the profit of their services at local level, by using the factor analysis including individual attributes and area characteristics. As a result, some important findings, concerned with influence factors to use frequency and WTP of shopping support services, came out of this study. These results must be useful information to introduce the suitable support services for PFD in consideration of each local need.

Approach to Improve Driving Condition on Desert highway from Viewpoint of Road Safety

Zulpikar KERAM and Yasuo HINO

Osaka City University, Memoirs of the Faculty of Engineering, Vol. 55, pp. 57-62 (2014)

Recently, the environmental problems caused by road construction and the road safety problems caused by desert climate have been getting more and more obvious. Especially, the road safety must be the most important issue against the desert weather. In this paper, the approach to improve the driving conditions on desert roads should be proposed from viewpoint of road safety, based on reviewing major results of a series of studies. As a result, an appropriate idea to prevent traffic accidents caused by desert weather from viewpoint of developing road facilities, in consideration of results of a series of studies.

Evaluation of Some Trial Bus Services to Support Elderly Persons toward the Active Town Life

Yasuo HINO, Kazuo MUKAI, Kazuya MIZUKAMI and Junichi MORITA

Japan Society of Traffic Engineers, Papers on Traffic Engineering, Vol. 1, pp. B18-B25 (2015) (in Japanese)

As population has been decreasing with both aging and declining birthrate, the activity of town with both residents and visitors must be required more and more. In order to realize the activity, it should be essential to provide the opportunity of going out with accompanying person based on the improvement of their mobility and accessibility in daily life. Therefore, three new trials of bus services, such as, “free charge for accompanied person on Sunday”, “discount fare of regular route bus to adjust the fare of small bus of same route” and “getting on and off at the non-designated bus stop in the limited areas”, were introduced in Kawachi-nagano city of Osaka prefecture, Japan. In this study, the user’s situation and evaluation for these services were analyzed by using the site survey and questionnaire survey. As a result, some important findings to evaluate the utility of these services and investigate the future approaches to realize the active town planning.

A Study on “Community Bus” System Focusing on Operation Transition and Regional Characteristics

Yusuke KURASHIMA, Megumi KATAYAMA, and Takashi UCHIDA

Japan Society of Traffic Engineers, Papers on Traffic Engineering, No. 34, pp. 445-450 (2014) (in Japanese)

Study on the Effect that Recognition and Application of Use Promotion Measure Gives to Will to Support Community Bus

Yusuke KURASHIMA and Takashi UCHIDA

Japan Society of Civil Engineers, Proceedings of Infrastructure Planning, No.50, pp. 3 (CD-ROM) (2014) (in Japanese)

Posterior Evaluation after the Development for the Nature-friendly Environment and the Water Amenity of the Medium and Small Size River in the Built-up Area -- an approach with a questionnaire to inhabitants --

Yasumasa FUKUSHIMA and Takashi UCHIDA

Japan Society of Civil Engineers, Proceedings of Infrastructure Planning, No. 50, pp. 9 (CD-ROM) (2014) (in Japanese)

In recent years the development of the urban river has been focusing on efforts for the environment and the water amenity besides the flood control and the water utilization. In the waterfront development various factors such as the river itself, the development conditions the environment in every region complicatedly connect each other, and moreover the stakeholders/agents such as local governments, inhabitants, planners, and bodies concerned are mutually involved, in some cases however, the residents along the river have failed to value and then water amenity have made little progress.

This paper takes a case of the waterfront development of the small size river in an emerging built-up area. Going through several years after the project implementation, we take hold of the actual condition and the evaluation by means of questionnaire survey to the inhabitants. An analysis focusing on their involvement with the waterfront development is conducted. This study gives basic data for the consideration on development methods in order to promote the utilization with high evaluations from the inhabitants.

Formation of Waterside Spaces with Groins

Yasumasa FUKUSHIMA and Takashi UCHIDA

Osaka City University, Memoirs of the Faculty of Engineering, Vol. 55, pp. 27-33 (2014)

River management in recent years involves measures for waterside management emphasizing the environment and utilization as well as river improvement and irrigation. This study addresses the formation of waterside spaces with groins as a part of waterside management emphasizing the environment and utilization, using typical groin management cases in which planning we have been engaged. This report presents our knowledge obtained through processes from planning, business implementation, and subsequent degradation by aging.

Midosuji Cycle Picnic Event for Raising the Awareness of Positive Images of cycling in Osaka

Itaru FUJIE and Nagahiro YOSHIDA

Velo-city 2015 in Nantes, Speed Dating Session (2015)

While bike commuting rate of Osaka city, the third largest city in Japan, increased by 33.7 percent in 2010, the prevailing image of cycling is still negative due to the long history of countermeasures for illegal parking issues or undesirable behaviors. Under these situations, some interested people planned a unique cycling demonstration event called as Midosuji Cycle Picnic for raising the awareness of positive images of cycling. The purpose of the event is 1) to demonstrate the cultural diversity of cycling for publics, 2) to get reliance about right-of-way from car drivers, 3) to increase the number of desirable cyclists who could use hand signals or eye contact with drivers, and 4) to make some recommendations for improving the condition of cycling infrastructure through demonstration.

The event is held at Midosuji, where is the main street in Osaka. It has been organized at the seventh time in September 2014 since 2011. Like a critical mass event in other countries, some picnic tours with different destinations are developed to attract people who may not have enough interest for the purposes. More than 300 cyclists, including visually impaired people with different types of bike like recumbent or tandem bicycle were participated. Participants were divided into small group, and cycled together on the roadway led by a group leader who could deliver proper attitudes to the member of the group. The organizer of this event is the Party of Making Cycling Town, who promotes bicycle usage in conjunction with urban planning. They also distribute education program, leadership training course, as well as communication materials for surroundings against negative images for cyclists.

The Effects of Shared Lane Pavement Markings: A New Trial of Osaka City

Nagahiro YOSHIDA, Teruyoshi TAKAHASHI, Masayuki KINUTA, and Masaaki MATSUNO

The third Asia-Pacific Cycle Congress, Spin Cycle Session (2015)

Recently safer cycling facility especially for urban area is required in the transport planning and traffic engineering to maximize environmental and health benefit in the world. In Japan, shared-use paths, which are commonly designed for two-way travel on both sides of road, has introduced into one of the Government Order on Road Design Standards to decrease bicycle-related accidents since 70s. However, recent research evidences showed riding on pavement included a negative impact on their risk as well as pedestrian's safety.

In addition, the Japanese government has published the technical guideline for bicycle transport in November 2012. The types of bicycle lane with regulation and shared lane pavement markings on roadway have been indicated for the first time as a part of technical guideline. In response to this, Osaka city, where is the third largest city in Japan and bicycle commuting share has increased by 33.7 percent in 2010, decided to introduce a bicycle lane and shared lane pavement markings on the roadway of the Honmachi-dori within the central business district in September 2013. The objective of the introduction on new bicycle path on roadways is to protect pedestrian safety, which means the extra path, were expected to encourage faster cyclists to change their path choice behavior. In order to get the effects of road markings, the before and after observations for traffic conditions as well as some questionnaire surveys for traffic participants including pedestrians, cyclists, and car drivers were conducted. After showing the basic comparison, the effect of different type of pavement markings on path choice behavior for cyclists using a discrete choice model were also indicated

Research on Bicyclist Safety Analysis on Sight Distance and Driving Behavior at Unsignalized Intersections along Highway

Yoshito TAKENAKA and Nagahiro YOSHIDA

Japan Society of Civil Engineers, Journal of JSCE, Division D3, Vol. 70, pp. I_1167-I_1172 (2014) (in Japanese)

Recently, using a bicycle is recommended under the growing concerns about health and environment, while the bicycle involved collision rate tends to increase. Some remarkable researches pointed out that a sight distance or driver's behaviors at intersections have affected an significant influence on bicycle safety, but the relationship between these factors are not clearly described together. Therefore, the purpose of this study is to investigate the possible factors of bicycle related accidents focused on the sight distance and driving behavior at unsignalized intersections along highway.

Analysis of Road Traffic Conditions and Individual Knowledge and experiences on Cyclist Path Choice Behavior

Takuya OKADA and Nagahiro YOSHIDA

Japan Society of Civil Engineers, Journal of JSCE, Division D3, Vol. 70, pp. I_655-I_661 (2014) (in Japanese)

Cycling on the sidewalks have brought some safety problems in Japan. Preceding research findings have suggested that building bicycle lanes on roadways or providing information related with traffic law may encourage cyclists to ride on the roadway. However, the effects of individual knowledge and experiences as well as road traffic conditions on cyclist path choice behavior are not clearly captured. The purpose of this paper, therefore, is to analyze these effects on path choice behavior. Multiple methods; a photomontage experiment and on-site observations were employed to collect both stated preference data and revealed preference data. As a result, some factors encouraging cycling on the roadways or discouraging cycling on the sidewalks as well as future intervention effects are revealed.

